High-Order Harmonic Generation from Molecules

by

Nicholas L. Wagner

B.S., Case Western Reserve University, 2001

A thesis submitted to the

Faculty of the Graduate School of the

University of Colorado in partial fulfillment

of the requirements for the degree of

Doctor of Philosophy

Department of Physics

2008

This thesis entitled:
High-Order Harmonic Generation from Molecules
written by Nicholas L. Wagner
has been approved for the Department of Physics

Prof. Henry Kapteyn

Prof. Margaret Murnane

Date

The final copy of this thesis has been examined by the signatories, and we find that both the content and the form meet acceptable presentation standards of scholarly work in the above mentioned discipline.

Wagner, Nicholas L. (Ph.D., Physics)

High-Order Harmonic Generation from Molecules

Thesis directed by Prof. Henry Kapteyn and Prof. Margaret Murnane

High harmonic generation in atoms is well understood in terms of the three step model (ionization, propagation and recombination), and much attention has been payed to the dynamics of the continuum electron in the propagation step. However, a molecular medium can be used to further understand the ionization and recombination steps. High harmonic generation can also be used to probe the dynamics of rotational and vibrational wave packets in molecular media.

This thesis reports on two experiments using high harmonic generation from molecular media. In the first experiment, an impulsive Raman pump is used to excite a rotational wave packet in the molecular system, and a second time-delayed pulse generates high harmonics from the rotationally excited medium. Both the intensity and the phase of the high harmonic emission are measured. The general features of the orientational dipole are extracted from the phase and intensity modulations.

A second experiment uses a vibrationally excited molecule as the high harmonic generation medium. The coherently excited molecular vibrations modulate the intensity of the high harmonic generation. Using high harmonic generation as a probe makes it possible to see all excited modes include two modes which were not present using a comparable visible probe. The rotational dephasing of the vibrational wave packet is also observed.

Acknowledgements

Many people have contributed to this work directly and indirectly. When I started graduate school, Randy Bartels and Tom Weinacht involved me in their work using molecular phase modulation, which I continued with Tenio Popmintchev. I learned about high harmonic generation experiments from Emily Gibson, with whom I also studied ionization pulse compression. I began studying high harmonic generation in molecular media with Andrea Wüest, with whom I did the majority of work presented here. He and I completed the vibrational study and laid the ground work for the study of rotational wave packets. Robynne Lock, Xibin Zhou and Wen Li have joined the project and continued studies on rotational and vibrational wave packets. In addition to those who have worked with me directly, Zach Walters has been very helpful with many theoretical discussions and determining what could be done with the analysis. Members of our research group helped me greatly, teaching me basic experimental competence, listening to my problems and helping develop my ideas. Emily Gibson, Etienne Gagnon, Xiaoshi Zhang and Amy Lytle have all worked and helped maintain the laser system. They frequently put aside their own work to allow me time to complete my studies. The support staff in JILA have made sure I have gotten paid, the machine shop has built large parts of my experimental apparatus and the supply office has purchased much of my experimental apparatus. Finally, my advisers Margaret Murnane and Henry Kapteyn have spend untold hours advising me and committed undue resources to allowing me to complete my studies.

Contents

Chapter

Tables

Table

Figures

Figure

Chapter 1

Introduction

High harmonic generation (HHG) is the nonlinear production of harmonics of an intense optical field by ionization and recollision of the an electron. It was first observed by McPherson, et al. [40] in 1987, where they observed the 17^{th} harmonic of 248 nm in neon gas. Typically, HHG is seen by focusing an ultrafast, high-intensity, near-IR pulse into a noble gas at intensities of $\sim 10^{14}$ W/cm^2, and observing the odd harmonics of the driving field. Initially, the surprising aspect of HHG is the plateau region of the high harmonic spectrum. In the perturbative region (3^{rd} - 7^{th} harmonic) the intensity of the each harmonic order drops rapidly. However, in the plateau region the harmonics are roughly the same intensity over many orders. Eventually the plateau ends in a cut-off region where the harmonic intensity drops rapidly. This plateau region was not what is expected from perturbative nonlinear optics, which would predict that each higher order would drop in intensity.

In 1993 Kulander[35] and Corkum[18] provided a theoretical explanation for high harmonic generation and the similar phenomena of above threshold ionization and non-sequential ionization. They explained high harmonic generation in terms of a three step model, as illustrated in 1.1. First, the atoms of the atomic gas are ionized at roughly the peak of the optical cycle. Second, the ionized electron, now in the continuum with no kinetic energy, is accelerated by the optical field. When the optical field changes direction, the free electron is accelerated back toward the parent ion. Third, when the

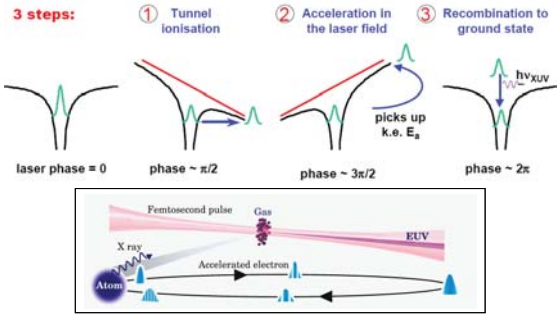

Figure 1.1: An illustration of the three step model of HHG

electron returns to the parent ion it can do three things: a radiative transition to the ground-state, inelastic scattering, or elastic scattering. The radiative transition results in HHG. The inelastic scattering is called non-sequential ionization, where the returning electron knocks an additional electron from the atom. Finally, elastic scattering results in very high energy electrons in the above threshold ionization spectrum. Based on simple classical electron trajectories in optical fields, the returning electron has a plateau of kinetic energies which is then manifest in the high harmonic spectrum.

Most research on high harmonic generation has concentrated on the second step of the free electron propagation: Specifically, some work has observed the long and short electron trajectories which both contribute to HHG[13], used the optical field to control and measure the electron propagation[50][33], increased the intensity to produce shorter wavelength EUV light[24] , shaped the field to selectively increase a single harmonic order[8]. One notable accomplishment of this line of research is the creation of isolated attosecond pulses[27].

The other heavily researched aspect of high harmonic generation has been phase-matching the process to produce more useful (higher flux) source of the EUV light. High harmonic generation is an attractive, tabletop source of EUV light when compared with large, expensive synchrotron sources. However, phasematching is needed to increase the conversion efficiency and improve the spatial coherence[10]. Waveguides[20], quasi-

phasematching[74], and pulse shaping[8] have all been used to develop high harmonic generation as a tabletop source of EUV light.

Both of these lines of research have used noble gases as the medium for HHG and have not focused on the first and third steps in the HHG process: strong-field ionization and recombination. One reason is that strong field ionization and recombination are not particularly interesting in isotropic atoms with no internal structure. However, when molecules are used as the medium for HHG, ionization and recombination become much more interesting and complex. Both of these processes can depend on the rotational and vibrational state of the molecule, which can potentially serve as a knob to control HHG. Additionally, high harmonic generation can be used as a probe to understand the rotational and vibrational dynamics of the molecular system.

Many aspects of of high harmonic generation in molecular media are not well understood, such as how the amplitude and phase of the ionized electron varies with molecular orientation. The initial structure of the electronic wave packet in the continuum could affect the recombination amplitude. The recombination amplitude could also be strongly affected by the molecular potential distorting the incoming plane wave. Additionally, a molecular system could break the isotropic symmetry and offer the possibility of generating high harmonics polarized perpendicular to the fundamental light.

This thesis reports on two experiments using high harmonic generation from molecules. In the first experiment, an impulsive Raman pump is used to excite a rotational wave packet in the molecular system, and a second time-delayed pulse generates high harmonics from the rotationally excited medium. Both the intensity and the phase of the high harmonic emission is measured. The general features of the orientational dipole are extracted from the phase and intensity modulations.

A second experiment uses a vibrationally excited molecule as the high harmonic generation medium. The coherent molecular vibrations modulate the intensity of the high harmonic generation. The high harmonic probe could see two modes which were

not visible using a comparable visible probe. The rotational dephasing of the vibrational wave packet was also observed.

1.1 Outline of the Thesis

The rest of this chapter presents a brief introduction to the Lewenstein model[38] of HHG and the approach taken to extend it to molecular systems. Chapter 2 presents the experimental apparatus used to measure the high harmonic intensity from excited molecules, and explains how the data is processed. The third chapter discusses the theory of rotational wave packets excited by an ultrashort laser pulse and the details of the time evolution that are important for understanding the high harmonic data. Then chapter 4 presents the data on harmonic emission from rotationally excited CO_2. Intensity and phase measurement are discussed from the perspective of extracting the orientational dipole. Chapter 5 presents data on high harmonic generation from vibrationally excited molecules. Chapter 6 summaries the work and provides a perspective for the future. Appendix A contains a derivation of the Lewenstein model. Appendix B presents work on pulse compression in ionizing medium, which is another project which I worked on during my graduate career.

1.2 Lewenstein Model of High Harmonic Generation

The theory of high harmonic generation can be divided into two parts: First, the single atom response is the dipole of a single atom in a strong optical field. Second, propagation deals with the phasematching and absorption in the medium and effectively adds up the contributions for all of the atoms generating harmonics.

The Lewenstein model[38] is a semi-classical model of high harmonic generation which calculates the single atom response. It is derived in appendix A. The goal of this model is to calculate the dipole responsible for the emission of high harmonics for an arbitrary optical pulse. The nonlinear dipole is calculated as a function of time in the

fundamental field. This dipole is then twice differentiated to get the electric field of the emitted harmonics. A Fourier transform then gives the high harmonic spectrum.

The main requirement for high harmonic generation is that the ionized electron must return to the parent ion. When the electron returns to the parent ion it contributes to a dipole response with a broad spectrum, the magnitude of the contribution depends on the degree/rate of ionization and the energy and direction the electron is returning with. So, to determine the dipole at a time t we first need to determine which electron trajectories return at that time and when they were ionized.

$$\nabla_p S(\mathbf{p}, t, t_i) = \int_{t_i}^{t} dt''(\mathbf{p} - \mathbf{A}(t'')) = 0 \tag{1.1}$$

Here S is the semi-classical action and represents the phase of the electron trajectory. This equation is the result of the stationary phase approximation which tells us which trajectories will contribute the most. $\mathbf{p}$ is the momentum that the electron has when it recollides. $\mathbf{A}$ is the vector potential of the fundamental field and t_i is the time at which the electron was ionized. When the fundamental field is sinusoidal, there are two solutions for every optical cycle that have a given recollision energy. These two solutions are called the long and short trajectories (corresponding to the time spent in the continuum). Solutions from the previous optical cycles can be ignored because the lateral spreading of the electronic wave function is proportional to the time spend in the field. So the shortest times contribute the most and trajectories in the continuum longer than one cycle can be ignored.

After the returning trajectories are known the dipole can be calculated.

$$d(t) = \sum_i a_i(t_i) a_p(t_i, t) a_r(t) \tag{1.2}$$

The dipole is the product of the complex amplitude from each step and is commonly summed over the two contributing trajectories (the long and short trajectories). a_i is

the ionization amplitude and is usually computed using static electric field ionization rates[1]. The phase of the ionization amplitude is usually neglected.

The propagation amplitude is a complex number with a constant amplitude; however, the phase is the phase the electron accumulates during propagation in the continuum. Any effect from the atomic potential is neglected. Because the electron accumulates phase faster than the fundamental field, the propagation amplitude oscillates many times faster than the fundamental optical field, leading to high harmonics.

$$a_p(t_i, t, p) = \exp(iS(t_i, t, p)) = \exp\left(i \int_{t_i}^{t} dt' \left[(\mathbf{p} + \mathbf{A}(t) - \mathbf{A}(t'))^2/2 + I_p\right]\right) \tag{1.3}$$

The recombination amplitude is the expectation value of the dipole operator using the total electronic wave function: the part in the ground state plus the part returning from the continuum. Only the terms mixing the ground state and returning wave contribute to HHG. We assume the fundamental electric field does not significantly affect the recombination. The returning electronic wave is approximated as a plane wave.

$$a_r(t, p) = \int \psi_{ground} \mu \mathbf{x} \exp(i\mathbf{p} \cdot \mathbf{x}) \tag{1.4}$$

The dipole calculated here is the single atom response; however, the observed HHG signal is emission from a macroscopic sample of atoms. The response of all of the atoms must be added coherently. With macroscopic sample of dipoles oscillating in phase, the resulting optical field does not have a dipole shape, but is emitted as highly directed beam propagating in the same direction as the fundamental field. The intensity of the emitted beam is strongly affected by the degree to which the atomic dipoles are in phase. This phase is in turn affected by the spatial variation of the optical field and the temporal slip between the harmonic field and fundamental field due to the medium and ionization. Several phasematching technique exist to minimize this phase variation and

produce more intensity harmonics: waveguides, quasi-phasematching, and pre-ionized media.

1.3 Modifications of the Lewenstein Model for Molecular Media

There are two immediate modifications necessary for molecular media. First the ionization rate can be calculated using a method appropriate for molecules such as MO-ADK theory[59]. Second, the recombination amplitude is calculated by approximating the electronic ground state as the highest occupied molecular orbital (HOMO).

There are several additional approximations which may be important in molecular systems. For the ionization step, there are several methods of calculating the strong field ionization rate[59][34], and the initial phase of the electron could also be important. For instance, is there a π shift in the electron phase when the electron comes from a positive or negative lobe of the HOMO? Additionally, nodes in the molecular electron density could change the shape of the outgoing electronic wave packet.

During the propagation step, the electron moves far from the parent ion and is not significantly affected by the potential. The maximum excursion of a typical electron is $\sim$10 nm for an 800 nm driving field, and the lateral spread of the electron is $\sim$1 nm.

During recombination it is also possible the single active electron approximation is not valid, meaning the bound electrons as well as the returning electron need to be considered[46][25]. The fundamental optical field could distort the molecular orbital and influence the recombination amplitude, and finally the molecular potential could distort the incoming plane wave[60]. There is no current consensus regarding whether these effects are important; and if they are, in which systems and regimes these effects matter. The experiments in this thesis show directly the orientational dependence which a molecular medium gives to the ionization and recombination amplitudes, as well as indirect evidence of the effect of the molecular potential on the returning plane wave.

Chapter 2

Experimental Apparatus

Rotational and vibrational wave packets evolve very fast (fs - ps), and a pump-probe technique is needed to observe the time evolution. A pump-probe technique is used when the detection device (such as a camera) does not have a fast enough response time to detect the time evolution. Instead of using the speed of the detector to capture the motion (as might be done with a high speed video camera), the speed of the illumination is used to detect the motion. A very short pump pulse creates the wave packet through an impulse excitation. Then, a time delayed probe pulse illuminates the wave packet for a very short time at some point after the pump. This is repeated for all time delays, and a complete picture of the motion is acquired. The pump-probe technique requires that the wave packet can be excited repeatedly and that pump and probe pulses are shorter than the time scale of the wave packet's time evolution. Our pump and probe optical pulses are created by a Ti:sapphire ultrafast laser amplifier. The output of the laser system is then split into a pump and probe pulse by a Mach-Zehnder interferometer. The pump pulse excites the wave packet in a gas jet. The probe pulse is then focused onto the same gas jet and generates high harmonics. The EUV harmonics are then detected using a spectrometer and a EUV CCD camera. The experimental apparatus is illustrated in figure 2.1.

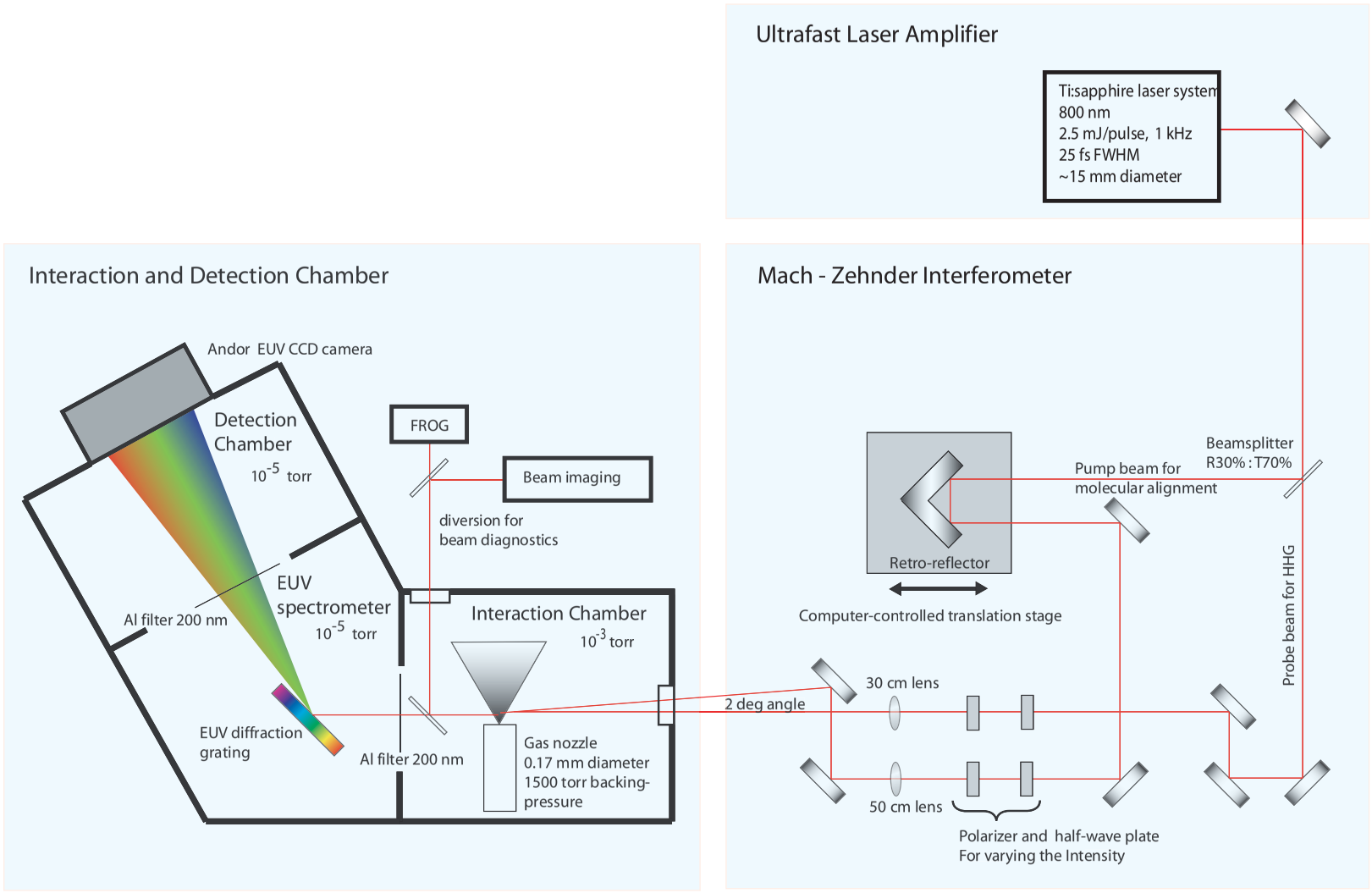

Figure 2.1: The experimental apparatus consists of three main parts: a Ti:sapphire amplifier, a Mach-Zehnder interferometer, and a glancing-incidence EUV spectrometer.

2.1 Ultrafast Amplified Ti:sapphire Laser System

The laser system used in this experiment is an amplified Ti:sapphire system[7]. This laser is ideal for HHG because of the very broad bandwidth of Ti:sapphire, which makes it possible to generate very short pulses. This is useful in the case of HHG because with a short pulse, the intensity can ramp up to a very high value before ionizing the medium. HHG typically requires ultrashort pulses < 30 fs and a per-pulse energy of ~ 1 mJ. Chirped pulse amplification[56] is used to produce pulses of this duration and intensity.

The laser system begins with the oscillator[2]. This is a Ti:sapphire laser that is continuously pumped and is mode-locked through a Kerr-lens. The repetition rate is determined by the length of the cavity and is 86 MHz in the system used here. The oscillator also contains a prism pair to compensate for the dispersion of the Ti:sapphire material, output coupler and focusing mirrors. The oscillator typically produces ~ 13 fs pulses with an average power of 450 mW.

Next, a Pockels cell is used to select isolated pulses from the 86 MHz pulse train coming from the oscillator. This is done primary because the 532 nm lasers used to pump the amplifier are limited in their repetition rate. So, the Pockels cell is used to lower the repetition rate of the seed pulse train to 1 kHz. This significantly reduces the average power of the pulse train (by a factor of 86,000).

The 13 fs pulse cannot be amplified directly because it would easily become intense enough to damage the Ti:sapphire amplification material. So,a chirped pulse scheme is used for amplification[56]. A grating-based stretcher makes the path length for 'blue' colors longer than 'red' colors. This stretches the 13 fs seed pulse to ~ 2 ps, without losing any spectral components.

The 1 kHz pulse train then goes through two ring amplification stages. The first stage can be thought of as an high gain amplifier and the second stage can be

thought of as a low gain, power amplifier. The amplification narrows the spectrum and lengthens the minimum pulse duration. The Ti:sapphire amplification crystals are pumped with 532 nm pulses approximately 100 ns in duration. These pump pulses deposit a significant thermal energy in the crystal causing a thermal lens. This thermal lens is minimized by cooling the crystals with liquid nitrogen[42]. At liquid nitrogen temperatures the thermal conductivity of the Ti:sapphire crystal is much larger which reduces the thermal lens.

After amplification the pulse train is compressed to its minimum duration, using a grating compressor. The compressor performs the opposite function of the stretcher. The 'blue' colors travel a shorter path than the 'red' colors. The pulses are compressed to a duration < 30 fs. The laser system used in theses experiments typically produces 3 mJ per pulse and has an average power of 3 W. The compressor can be adjusted to compensate for material further down the line in the experiment.

2.2 Mach-Zehnder Interferometer

The second part of this apparatus is a Mach-Zehnder interferometer that is used to separate the original pulse into two time-delayed pulses and adjust the power, polarization and focusing of each arm of the interferometer. The laser beam is first split in two by a multilayer dielectric beamsplitter, usually 50% of the power in each beam. The beam used to pump the molecular coherence is then time-delayed using a computer controlled translation stage and a retro-reflector.

The retro-reflector greatly simplifies alignment of the interferometer and insures that the pointing of the time-delayed beam does not change as the time-delay is adjusted. The motor used to adjust the time-delay is also important. The coherence of molecular rotations can last up to a few 100 ps, which requires the range of the translation to be ~ 2 cm. However, the features of the wave packet are typically 100 fs in duration. So, a resolution of ~ 10 fs is required for rotational wave packets. Vibrational wave

packets require resolution shorter than the vibrational period. In these experiments, it is often necessary to average several datasets to obtain a good signal-to-noise ratio. This requires a motor that can return to its original position after moving ~ 2 cm away. These requirements are best met using a closed-loop motor and a position sensor.

The duration of the pump pulse can also be adjusted by putting material in the pump arm. This material disperses the pulse and increases its duration. This is usually done when pumping rotational wave packets. A pulse of 100-200 fs is usually sufficiently short to impulsively excite a rotational wave packet. So by increasing the pulse length the peak intensity can be lowered, which minimizes other processes such as ionization and multi-photon dissociation which are undesirable. When pumping a vibrational wave packet, the material is removed and a short sub-30 fs pump pulse is used, since it necessary to use a pump pulse with a duration less than half of the vibrational period.

Both arms of the interferometer include a 1/2 waveplate and a polarizer, used to adjust the power on each beam. For some experiments an additional 1/2 waveplate is inserted after the polarizer to adjust the polarization of the pump pulse. Finally both beams are focused using lenses. The probe/HHG beam is focused with a 30 cm lens, and the pump beam is focused with a 50 cm lens. This insures that the probe spot is smaller than the pump spot in the interaction region. Because the probe spot size is smaller than the pump, it sees a more uniform excitation and does not see the lower intensity edges of the pump pulse. Both lenses are mounted on translation stages along the axis of propagation to adjust their positions relative to the gas jet in the generation chamber. The lenses are also mounted to allow translation perpendicular to the beam for fine adjustment of the overlap of the two beams at the gas jet.

Optical interference is used to align and find time-zero for the interferometer. First, both arms of the interferometer are set to approximately the same length using a tape measure. The time delay is scanned by hand until an interference pattern is observed. Once the interference pattern is found, the pointing of each beam can be

adjusted until the interference fringes become a bullseye, which indicates both beams are propagating parallel to each other. The timing is then adjusted until the fringe contrast is maximal, this allows the time-zero of the interferometer to be found within ± 10 fs. In the non-collinear case discussed below the bullseye pattern cannot be used.

After both beams pass through their respective lens, they are recombined. This is done by one of two methods: a dielectric beam splitter or a non-collinear reflection. Using a dielectric beamsplitter allows both the pump and probe to propagate collinearly and is much easier to align; however, a significant amount of power ($\sim 1/2$) is lost at the beamsplitter and the polarization cannot be rotated without changing the reflectance of the beamsplitter. A second technique is to reflect the pump with a mirror immediately next to the probe beam. The angle of the mirror is set such that the beams cross at the focus/gas jet at a very small angle < 3 degrees. This method allows for more efficient use of the laser power and for adjustment of the polarization of the pump. We did not find that the HHG signal depended on which geometry we used, as long as the incident pump and probe pulses emerging were the same.

2.3 Generation Chamber

After the beams are focused and combined, they enter the generation chamber which contains a gas jet and a 550 l/s turbo pump. The beams enter the chamber through a thin (250 μm) sapphire window to minimize dispersion and nonlinear effects.

When generating high harmonics it is necessary to let the gas interact with the laser in only a small region near the focus. If there is gas present while the laser is focusing, nonlinear effects will modify the pulse temporally and spatially, which changes the position, shape and intensity of the focus. After EUV light is generated by HHG, it must propagate in a vacuum because it is strongly absorbed by all materials and gases. Because of these two requirements, windows can not be used to confine the gas. There are, however, two common windowless methods of confining gases for HHG:

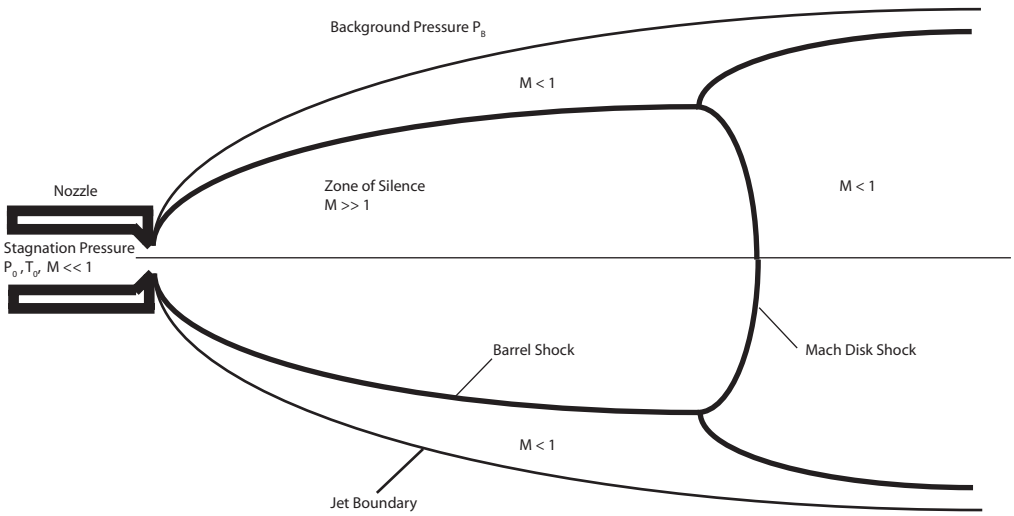

Figure 2.2: Diagram of a free jet expansion.

hollow-waveguides with differential pumping[20], and gas jets[52]. When using HHG as a molecular probe it is desirable to minimize propagation effects, so a gas jet is preferable because it has a very short interaction length, < 500 μm. In addition to confining the gas and minimizing the interaction length, the supersonic expansion in the gas jet also cools the temperature of the gas significantly from room temperature to $\sim$ 75K.

The gas jet used in this experiment is a rather simple design. It consists of a short piece of fused silica capillary tubing with an inner diameter of 150 μm, an outer diameter of 1.2 mm and a length of 1 cm. One side of the capillary tube is the molecular gas at a stagnation pressure of 700-2000 torr. The gas moves through the capillary and supersonically expands into the vacuum chamber. The chamber has a pressure $< 10^{-5}$ torr when the gas jet is turned off, and a pressure of $\sim 10^{-3}$ torr when gas is flowing. Ideally a larger turbo pump would reduce the background pressure in the chamber and allow a 'cleaner' supersonic expansion. However, the density needed for efficient HHG is $> 10^{17}$ W/cm^2 , and the laser is aligned to intersect the gas jet very near the end of the capillary, usually 100-300 μm. Hence the background does not have a significant effect on the expansion in this region. The background pressure is also low enough to avoid

absorption of EUV light produced through HHG. The gas jet parameters for several gases and distances away from the nozzle are shown in figure 2.3.

2.4 Detection Chamber

The detection chamber consists of a Hettrick glancing-incidence EUV spectrometer and an Andor EUV camera. It is pumped by a smaller turbo pump and is typically at a pressure of $< 10^{-6}$ torr. After the EUV light is produced at the gas jet, it leaves the generation chamber and enters the detection chamber. First, it passes through a small differential pumping aperture, which separates the detection chamber from the generation chamber. Next the EUV light passes through a 200 nm aluminum filter. The purpose of the aluminum filter is to reject the fundamental light and prevent it from reaching the EUV camera. The EUV light then passes through a glancing incidence EUV spectrometer and the harmonic orders are spatially separated. Then the EUV passed through a second 200 nm aluminum filter to further reject the fundamental light and then is detected on the Andor EUV camera.

The Andor EUV camera is similar to a common CCD camera except for three aspects. First, the CCD is mounted in a vacuum without any coating or glass cover, because any air, coating, or cover would absorb the EUV light before it could be detected. Second, the CCD chip is cleaved off of the wafer and the back is lapped to be very thin ($\sim$ 10 nm). The EUV light hits the CCD chip from the back and is transmitted through the back-thinned chip and creates an electron-hole pair which is then detected. The camera is also cooled to -60° C to minimize the thermal noise.

However, because the CCD can also detects the fundamental 800 nm light, it must be separated from the EUV harmonics. When the fundamental light is allowed to hit the camera it easily saturates the dynamic range of the CCD. Aluminum filters are commonly used to separate the high harmonic and the fundamental light. The fundamental is reflected by the surface of the aluminum and the harmonics are transmitted through

Characterization of gas jet properties

p_0 = 1500 torr

	N_2, O_2		CO_2, N_2O	
d / μm	150	170	150	170
Mach disk location				
x / cm	~12	~14	~12	~14
Quitting surface location				
x_q / mm	~8	~10	~18	~20
Translational temperature on axis in K				
x / μm				
100	~150	~180	~190	~200
200	~100	~110	~110	~140
300	~70	~80	~80	~100
400	~60	~60	~70	~80
Rotational temperature (in mol. flow region) in K				
	~0.1 * T_0 = 30		~0.1 * T_0 = 30	
Density on axis in cm^{-3}				
x / μm				
100	1×10^{19}	2×10^{19}	1.3×10^{19}	1.2×10^{19}
200	3×10^{18}	5×10^{18}	3×10^{18}	5×10^{18}
300	2×10^{18}	2×10^{18}	1.2×10^{18}	1.5×10^{18}
400	9×10^{17}	1×10^{18}	0.9×10^{18}	1×10^{18}
Pressure on axis in torr				
x / μm				
100	~200	~300	~190	~250
200	~40	~50	~40	~70
300	~10	~15	~12	~18
400	~5	~8	~6	~7
Off-axis half-widths in μm				
x / μm				
100	~100	~100	~80	~80
200	~150	~150	~140	~140
300	~200	~200	~200	~200
400	~250	~250	~300	~300

Figure 2.3: Properties of the gas jet for several gases and distances away from the nozzle. These values were calculated using methods shown in *Atomic and Molecular Beam Methods [52].*

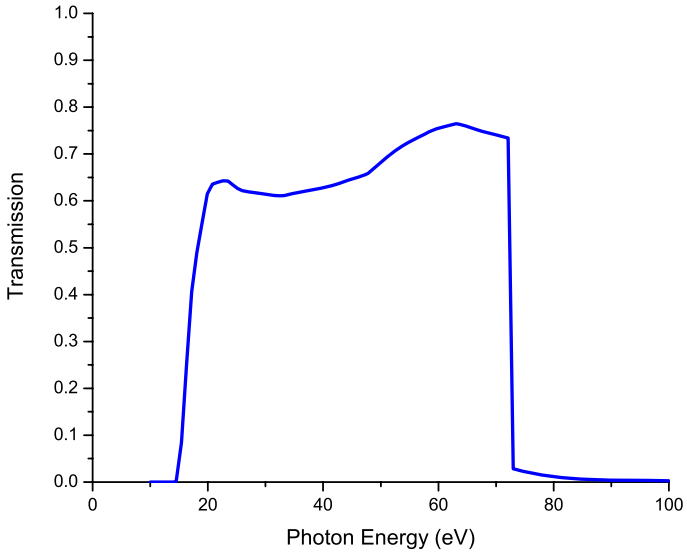

Figure 2.4: The transmission as a function of photon energy for EUV light through the 200 nm aluminum thin film filter, which is used to reject the fundamental light. Most of our experiments are limited to observing HHG emission in the range of ∼20-72 eV.

the thin foil of aluminum. The fraction of the light transmitted is shown in figure 2.4. The aluminum filter passes photons with energy between 17 and 72 eV. In the systems we studied, these energies are also those most abundantly produced by HHG. Higher harmonic orders can be observed by using other metallic filters such as zirconium or silver, which have transmission windows at high energies. It is necessary to use very thin 200 nm aluminum filters so a significant fraction of the EUV light is transmitted; however when filters are very thin, they often have small pinholes. Because of this, it is necessary to use two separate filters: one before and one after the spectrometer. Any fundamental light which leaks through pinholes on the first filter is allowed to diffract, and only a very small portion of this can then leak through any pinholes on the second filter.

It is also important to mount the aluminum filters carefully. Being a thin 200 nm foil up to 1 inch in diameter, the filters will break if they have too much differential air pressure on them when the chamber is pumped down. So the mount must allow air to easily move around the filter but not allow light the leak around it. Ariel Paul[47] has designed a baffle for this purpose, which conveniently fits into a NW40 flange.

No materials reflect EUV light at normal incidence with any significant efficiency, however at glancing incidence the fraction of reflected light becomes greater. Thus glancing incidence reflections are typical used in EUV systems. The spectrometer used in these experiments contains a gold mirror and a diffraction grating at glancing incidence. The gold mirror is spherical; however at glancing incidence the effective focal length in the plane of incidence become very long and can be ignored[3]. At glancing incidence, the spherical mirror is effectively a cylindrical mirror, which focuses the light in the spectrally-dispersed dimension. The other dimension is allowed to diffract naturally.

2.5 Typical Raw Data

The CCD camera is 1024 by 256 pixels with 12 bit resolution; however, usually the smaller dimension is integrated on the chip in 'full vertical binning mode'. A typical spectrum from argon is shown in figure 2.5, where orders 19-45 can be seen. The maximum energy/harmonic order is limited by the aluminum filter. In figure 2.5, the peaks from the first-order diffraction from the grating are labeled in red, and second order diffraction is labeled in blue.

The harmonic order can be determined using two methods. First, there is a sharp cutoff in the aluminum transmission at 72.7 eV. The central wavelength of the laser is 790 nm so the last harmonic order visible below the absorption edge should be the 45^{th}. The harmonic orders can be counted down from the 45^{th}. When a longer wavelength fundamental field of 805 nm is used, the 47^{th} drops below the aluminum edge, however the laser used in these experiments has a central wavelength closer to 790 nm.

The second method compares the 1^{st} and 2^{nd} order diffraction peaks. The same spectrum must be represented in both diffraction orders and spaced according to the grating equation $d \sin\theta = n\lambda$. This means the 46^{th} harmonic observed in the second-order of the grating diffraction emerges from the grating at the same angle as the 23^{rd} harmonic from the first-order diffraction. We can use this property to determine the order of the each harmonic in the spectrum. First, Label the highest harmonic observed peak order p and the 12^{th} peak in, order q. The 12^{th} peak is used because that is where the second order from the grating begins. Because the highest peak from the second order is just below the q^{th} harmonic,

$$p = 2q - 1 \tag{2.1}$$

Additionally, the p^{th} harmonic is the 11th harmonic above the q^{th} so,

$$p = q + 2 \times 11 \tag{2.2}$$

These two equations can be solved to get $p = 45$ and $q = 23$. Then, the rest of the harmonic orders can easily be labeled. Both methods give the same result.

2.6 Removing Cosmic Rays

Cosmic rays sometimes hit the CCD and cause counts on the pixels of the camera. This can be a problem if these cosmic rays which obscure the data. The problem is acute when the CCD integration time is longer than 10 seconds in 'full vertical binning mode'. However, the effect of the cosmic rays can be eliminated by taking two identical spectra one after another. Any differences between them are assumed to come from cosmic rays hitting the CCD, and the differences are replaced by neighboring values.

2.7 Setting Focal Positions

The pump beam is focused such that the center of the focus is aligned with the center of the gas jet, and the most intense part of the focus is used to pump the molecular coherence. However, the high harmonic beam is aligned such that it is focus slightly before the gas jet, because this is where the most intense harmonics are created and the short trajectories are selected through spatial phase matching[51]. Figure 2.6 shows the high harmonic intensity from SF_6 as a function of the high harmonic focal position. The high harmonic intensity is most intense when the focus is ~ 2 mm before the gas jet.

2.8 Background Subtraction and Integration

In the analysis of the data, we would like to retrieve a number from the high harmonic spectrum which is proportional to the intensity of each harmonic order. As

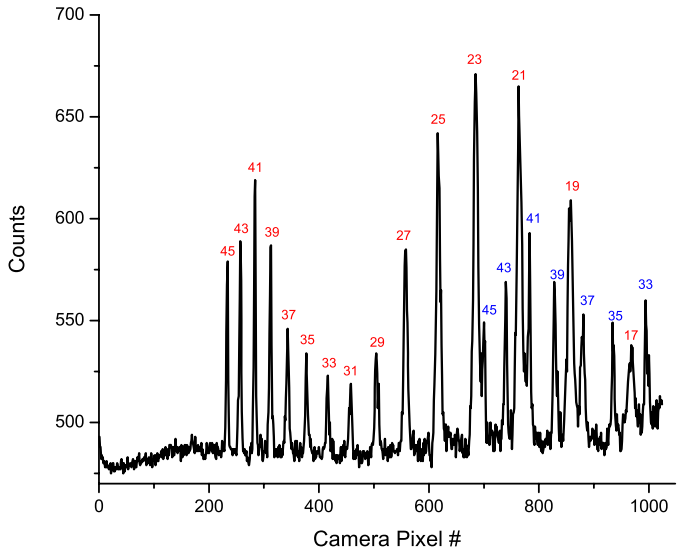

Figure 2.5: A typical high harmonic spectrum generated by a 28 fs pulse in argon gas with a density of 10^{18} cm^{-3}. The peak intensity of the pulse was $\sim 10^{14}$ W/cm^2. Lower energy harmonics are on the right side of the graph and higher on the left side. The harmonic orders are labeled in red for the first order diffraction from the grating and in blue for the second order diffraction.

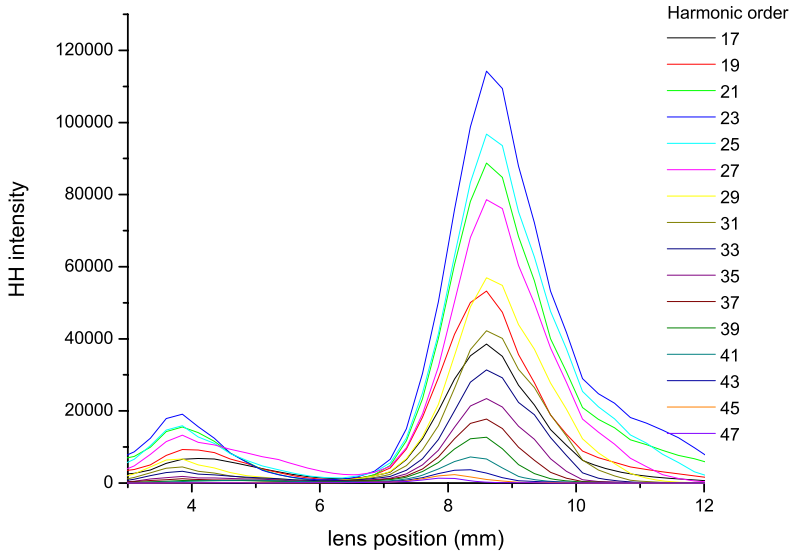

Figure 2.6: High harmonic intensity in SF_6 is plotted against the position of the lens focusing the HHG beam. The focus is aligned to the outlet of the gas jet at 6.5 mm; however, HHG is most intense when the focus is 2 mm before the jet. This position also selects the short trajectory harmonics[51].

can be seen in the argon spectrum in figure 2.5, the number of counts on the camera is not zero between the harmonic orders. This non-zero background must be subtracted before each harmonic peak can be integrated. The background is due mainly to two factors: thermal noise in the CCD and scattered EUV light. Because part of the background comes from the EUV light, the background level will change with overall EUV intensity. So each spectrum has a unique background. The background is determined by drawing a cubic spline through points midway between the harmonic peaks, and this background is then subtracted from the spectrum. Once the background has been removed the peaks are integrated to get the relative intensity of the harmonic order.

Chapter 3

Theory of Impulsively-Excited Molecular Rotational Wave Packets

The use of an optical field to align a molecule is a powerful technique making it possible to study how molecular orientation affects many physical processes, including HHG, as well as processes such as chemical reactions, photoelectron emission, and the temporal variation of the index of refraction[55]. Optical fields can be used to align molecules in two regimes: static and dynamic alignment. In static alignment, the duration of the optical pulse is much longer than the rotational time constant and the molecules align adiabatically to the field. In the dynamic case, the duration of the optical pulse is much shorter than the rotational period and excites many rotational levels, forming a rotational wave packet. As the rotational wave packet evolves in time the molecules periodically align along the direction of the polarization and anti-align perpendicular to the polarization. Typically using either method, an intensity around 10^{13} W/cm^2 is required to significantly align a molecular sample with a rotational temperature of 100's of Kelvin.

This chapter explains how molecules are dynamically aligned, specifically how the rotational wave packet is excited, and the characteristics of the time-evolution of the induced alignment.

3.1 Alignment After an Impulsive Torque

The impulsive pump excites rotational levels through a two-photon Raman process. The rotational levels are excited such that immediately after the pump pulse has passed there is an initial alignment. This initial alignment can be understood in terms of a classical rigid rotor. The subsequent revivals are a result of the quantization of the rotational energy levels and require a quantum mechanical description.

Starting with a classical rigid rotor, a torque can be applied to the rotor which causes the rotor to swing toward alignment. Consider a rotor with an initial angle θ with respect to the electric field as shown in figure 3.1. We can ignore the azimuthal angle ϕ, because the geometry is symmetric in that angle. Additionally, assume the rotor is initially stationary, or more specifically assume that the impulse given by the electric field (torque multiplied by time) is much larger than the average thermal angular momentum (moment of inertia multiplied by thermal angular velocity).

The electric field induces a dipole in the molecule. The induced dipole then feels a torque from the electric field. The torque exerted by an electric field is $\tau = \mu \times \mathbf{E}$ where μ is the induced dipole which is determined by the polarizability tensor, $\mu = \alpha \cdot \mathbf{E}$. For a linear molecule the polarizability can be described by a polarizability parallel and perpendicular to the molecular axis.

$$\alpha = \begin{pmatrix} \alpha_\perp & 0 & 0 \\ 0 & \alpha_\perp & 0 \\ 0 & 0 & \alpha_\parallel \end{pmatrix} \tag{3.1}$$

This polarizability tensor assumes the molecule lies along the z-axis. However, we can rotate it through the polar angle θ.(Clockwise rotation around the y-axis.)

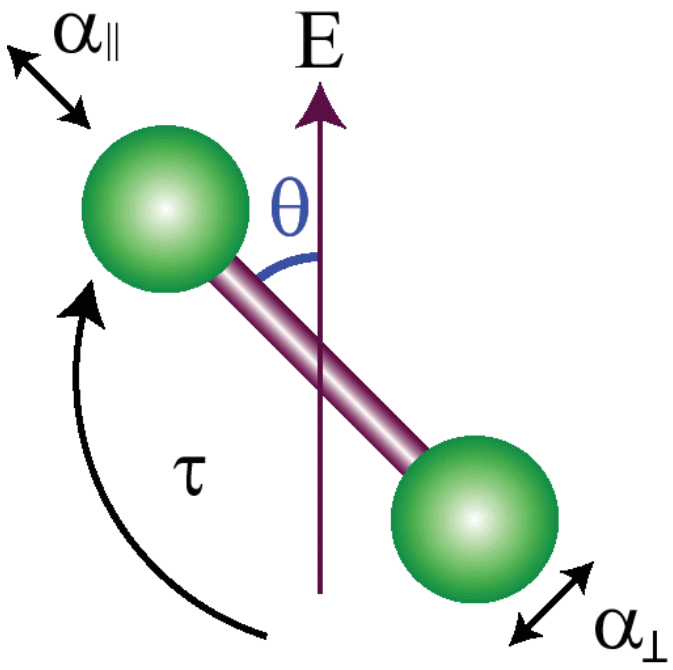

Figure 3.1: An impulsive pump pulse applies a torque to a linear molecule. The molecule is kicked in the direction of the polarization of the pump pulse.

$$\alpha(\theta) = \mathbf{R}^T \alpha \mathbf{R} = \begin{pmatrix} \alpha_{\parallel} - \Delta\alpha \cos^2\theta & 0 & \Delta\alpha \sin 2\theta \\ 0 & \alpha_{\perp} & 0 \\ \Delta\alpha \sin 2\theta & 0 & (\alpha_{\perp} + \Delta\alpha \cos^2\theta) \end{pmatrix} \tag{3.2}$$

where $\Delta\alpha = \alpha_{\parallel} - \alpha_{\perp}$. Now, we can use the rotated polarizability tensor to determine the torque on the molecule. At this point, we'll set the electric field to be polarized along the z-axis.

$$\tau = \mu \times \mathbf{E} = (\alpha \cdot \mathbf{E}) \times \mathbf{E} = -\Delta\alpha \sin 2\theta E_z^2 \hat{y} \tag{3.3}$$

The torque is zero when the molecule lies parallel or perpendicular to the electric field, and the torque is maximum at 45°. This formula for the torque can be inserted into the angular version of Newton's second law to get a differential equation for the classical time evolution. This equation will tell us how a rotor with initial position θ_0 will evolve with time, $\theta(t)$.

$$I \frac{d^2\theta(t)}{dt^2} = -E^2(t)\Delta\alpha \sin 2\theta \tag{3.4}$$

Here I is the moment of inertia of the rotor. Dynamic alignment requires an impulsive torque. The time scale of the rotational motion is $\sqrt{\frac{I}{E^2\Delta\alpha}}$ so the electric field pulse must be shorter than this, so a delta function $E^2(t) = \beta\delta(t)$ impulse is used. If the rotor is initially not moving and is at an angle θ_0 to the electric field, then the expression for the position after the pulse is

$$\theta(t) = \theta_0 - \left(\frac{\beta\Delta\alpha}{I} \sin 2\theta_0\right) t \tag{3.5}$$

This equation relates the angular position of the rotor to its initial position. The result is plotted in figure 3.2 for several time delays. At t = 0.6 (Green curve), there is an alignment because a large number of initial angles correspond to positions near zero.

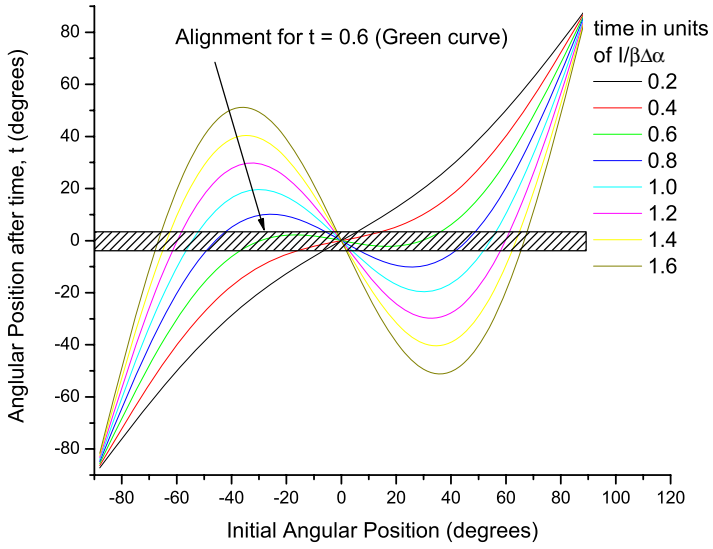

Figure 3.2: Classical calculation of impulsive alignment of CO_2. The molecular axis position for several time delays after the initial impulse as a function of initial angular position is shown. The initial alignment is seen a t=0.6.

This shows there is an initial alignment shortly after an impulse torque. It is not useful to extend this classical model further because is does not exhibit the revivals, which are due to the discrete rotational energy levels.

3.2 Quantization of Rotational Energy Levels and Revivals

The rotational wave packet is periodic in its time evolution. This periodic nature is due to the wave packet's composition from rotational eigenstates with discrete energies. Rotational eigenstate, $|JM\rangle$, has an energy $BJ(J+1)$. Here B is the rotational constant of the molecule and defines the time scale of the rotational dynamics. The rotational constant is inversely related to the moment of inertia: $B = \frac{\hbar^2}{2I}$. A rotational wave packet can be expressed in terms of the rotational eigenstates with complex coefficients, c_{JM}, and energy-dependent phase accumulation.

$$\psi(t) = \sum_{J,M} c_{JM} e^{-iE_J t/\hbar} |JM\rangle = \sum_{J,M} c_{JM} e^{-iBJ(J+1)t/\hbar} |JM\rangle \tag{3.6}$$

When no electric fields are present($H = BJ^2$), the coefficients are independent of time, and the dynamics comes from interference between rotation levels of different energies. If we consider a time $t = \frac{\pi\hbar}{B}$, then the phase of each state is $\pi J(J+1)$. Because J is restricted to positive integer values, the phase at this time is a multiple of 2π for all possible values of J. This means the wave packet at this time(and multiples of this time) is the same as the wave packet at t = 0; the wave packet periodically repeats itself. The time period between the repetition is called the revival time. Because there is an initial alignment after an impulsive torque(as described in the previous section), this initial alignment will repeat itself at the revival time. This is called the full revival. At fractions of the revival time $(1/2, 1/4, 1/8, \ldots)$, there are fractional revivals during which only a portion of the states are in phase.

3.3 Quantum Calculation of Rotational Wave Packet

Rotational wave packets are usually characterized by the alignment parameter $< \cos^2\theta >$; however, this is not a full description of the time evolution. In fact, some fractional revivals are not seen in $< \cos^2\theta >$, but are seen in full angular density. The goal of calculating the rotational wave packet is to calculate the time evolution of the alignment parameter and the angular density. The calculation presented here follows Ortigoso[45].

We start by deriving the Hamiltonian for a linear molecule in an optical field. A molecule interacts with light through the dipole operator.

$$H = H_0 - \frac{1}{2}\mu \cdot \mathbf{E} \tag{3.7}$$

The dipole operator can be expanded as a Taylor series in the electric field.

$$\mu = \mu_0(\theta) + \alpha(\theta) \cdot \mathbf{E} + \ldots \tag{3.8}$$

We have chosen the laboratory frame where the direction of the electric field is constant, so the permanent dipole $\mu_0(\theta)$ and polarizability $\alpha(\theta)$ are functions of the molecular orientation. We only expand the dipole to the term which is linear in the field because the rotational alignment is caused by the induced dipole (the second term). Dropping high-order terms ignores higher-order non-linear effects. Next, we put the Taylor expanded dipole into the Hamiltonian.

$$H = H_0 - \frac{1}{2}\mu_0 \cdot \mathbf{E} + \frac{1}{2}(\alpha \cdot \mathbf{E}) \cdot \mathbf{E} \tag{3.9}$$

Now, we will restrict the electric field to the optical frequencies, or frequencies much larger than the rotational time scale, $\omega >> B/\pi\hbar$. The typical timescale for molecular rotations is picoseconds and an optical cycle is 1-2 femtoseconds. During an optical cycle the position of the molecule is frozen. The permanent dipole term averages

to zero over the optical cycle because it is linear in the field. However, the polarizability term does not average to zero because it depends on the square of the electric field and remains positive from one half cycle to the next.

We have already determined the polarizability for the linear molecule as a function of the polar angle θ.

$$\alpha(\theta) = \mathbf{R}^T \alpha \mathbf{R} = \begin{pmatrix} \alpha_{\parallel} - \Delta\alpha \cos^2\theta & 0 & \Delta\alpha \sin 2\theta \\ 0 & \alpha_{\perp} & 0 \\ \Delta\alpha \sin 2\theta & 0 & (\alpha_{\perp} + \Delta\alpha \cos^2\theta) \end{pmatrix} \tag{3.10}$$

Now, we will set the electric field to be polarized in the z-direction and insert the polarizability into the Hamiltonian. Additionally, the field-free Hamiltonian is just the rotational energy operator, $B\mathbf{J}^2$.

$$H = B\mathbf{J}^2 + \frac{1}{4}\mathbf{E}^2(t)\left(\Delta\alpha \cos^2\theta + \alpha_{\perp}\right) \tag{3.11}$$

This Hamiltonian is most easily dealt with in the $|JM\rangle$ basis. In the matrix form, $\langle JM\,|H|\,J'M'\rangle$ is non-zero only for $J = J'$ or $J = J' \pm 2$ and $M = M'$. The time-dependent Schrödinger equation can be expressed as an infinite number of differential equations where each differential equation corresponds to a $|JM\rangle$ state. Because states with $J > 40$ are not typical populated thermally or excited, the equations for $J > 40$ can be neglected. The system of differential equations can be solved numerically.

The initial condition for this problem is a thermally populated ensemble of rotational states, which are populated in a Boltzmann manner and have incoherent phase relationships. This can be modeled by calculating the time evolution many times and adding the results incoherently. The time evolution is calculated using each thermally excited $|JM\rangle$ state as an initial condition. The initial condition is a pure $|JM\rangle$ state. The observable such as $< \cos^2\theta >$ or angular density $\langle\psi|\psi\rangle$ is calculated for each initial state. The observable is then added incoherently weighted by the thermal populations.

The result is the thermally averaged alignment parameter or angular density.

There are several parameters specific to individual molecules that go into these calculations. The rotational constant defines the energy level spacing. The anisotropic polarizability sets the strength of the interaction. Table 3.1 lists these parameters for some small molecules.

Molecule	Rotational Constant, B	anisotropic polarizability, $\Delta\alpha$
N_2	1.99 cm^{-1}	0.7 $Å^3$
O_2	1.43 cm^{-1}	1.1 $Å^3$
CO_2	0.39 cm^{-1}	2.1 $Å^3$
N_2O	0.43 cm^{-1}	2.8 $Å^3$

Table 3.1: The rotational constant and anisotropic polarizability for several common molecules[28].

3.4 Wave Packet Simulations

The alignment parameter $< \cos^2\theta >$ is 1/3 for an isotropic, unexcited ensemble. For an ensemble perfectly aligned along the z-axis, $< \cos^2\theta >= 1$. For an ensemble lying in a plane perpendicular to the z-axis $< \cos^2\theta >= 0$. When the alignment parameter is greater than 1/3 the sample is 'aligned' and when the alignment parameter is less than 1/3 the sample is 'anti-aligned', meaning that distribution lies in a plane perpendicular to the polarization and has azimuthal symmetry.

The calculated alignment parameter for CO_2 is shown in figure 3.3 a). The wave packet is excited with a 140 fs pulse with a peak intensity of 5×10^{13} W/cm^2. The pump pulse comes at $t = 0$, and after the pump pulse has passed there is an initial alignment. The initial alignment is repeated after one full rotational period (42.6 ps for CO_2). There are also half and quarter revivals in CO_2. In between the revivals, the wave packet is not static. There is still a lot going on, but it is not visible in $< \cos^2\theta >$. These smaller fractional revivals, eighth etc., can be seen in the time evolution of the angular density shown in figure 3.4. The angular density is generally a function of the

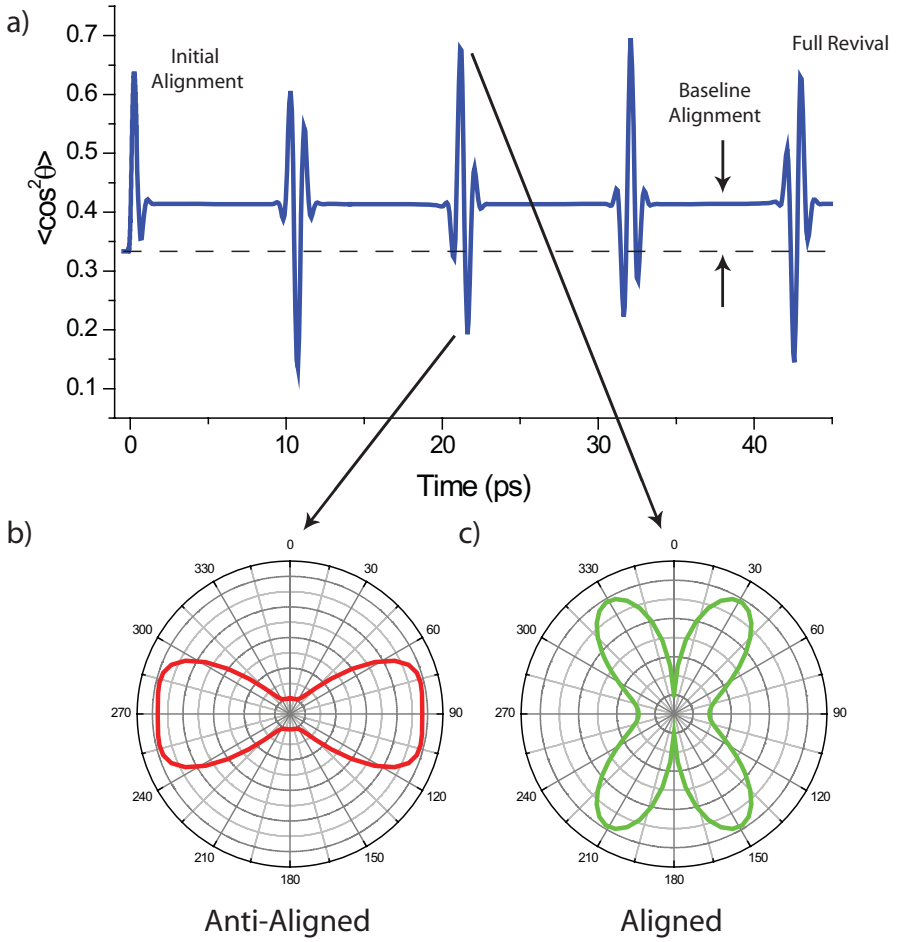

Figure 3.3: a) The alignment parameter $< \cos^2\theta >$ shown as a function of time for CO_2. b) The weighted angular density at a time of anti-alignment. b) The weighted angular density when aligned.

polar and azimuthal angles; however, a linear polarized optical field can not change the magnetic quantum number m. Because of this, the wave packet retains the cylindrical symmetry of the initial thermal ensemble. The angular density shown in figures 3.3 and 3.4 is averaged over the azimuthal angle and weighted by the sine function from the angular differential, $\sin\theta d\phi d\theta$.

$$P(\theta) = \int_0^{2\pi} P_{full}(\theta, \phi) \sin\theta d\phi \tag{3.12}$$

Here $P_{full}(\theta, \phi)$ is the full angular density and is has a functional dependence on both the polar and azimuthal angles. However, in most cases the azimuthal dependence is unimportant due to the cylindrical symmetry of the wave packet. $P(\theta)$ the angular density with azimuthal integration already done. This somewhat more useful form of thew angular density for visualizing the effect of the molecular alignment.

3.5 Sweeping of the Angular Position During Alignment

When the molecule is aligned it cannot be thought of as having the molecular axis parallel to the pump pulse polarization, as illustrated in the 3.5. The angular density $P(\theta, \phi)$ is maximized parallel to the polarization. However, the important quantity is the density at each polar angle,$\int P(\theta, \phi) \sin\theta d\phi$. The sine term in the azimuthal averaging forces the weighted angular density to zero at $\theta = 0$, and the angular distribution is a butterfly pattern, which peaks at some angle near zero but not at zero. As the alignment pulse intensity is increased or the temperature is decreased, a higher degree of alignment is achieved and the butterfly pattern peaks closer to zero.

In summary, during alignment the wave packet is localized around an angle near zero. At times near the maximum alignment the wave packet is still roughly localized and sweeps through angles until the maximum alignment is reached. Then the wave packet sweeps through the angular positions in the opposite direction. This can be seen

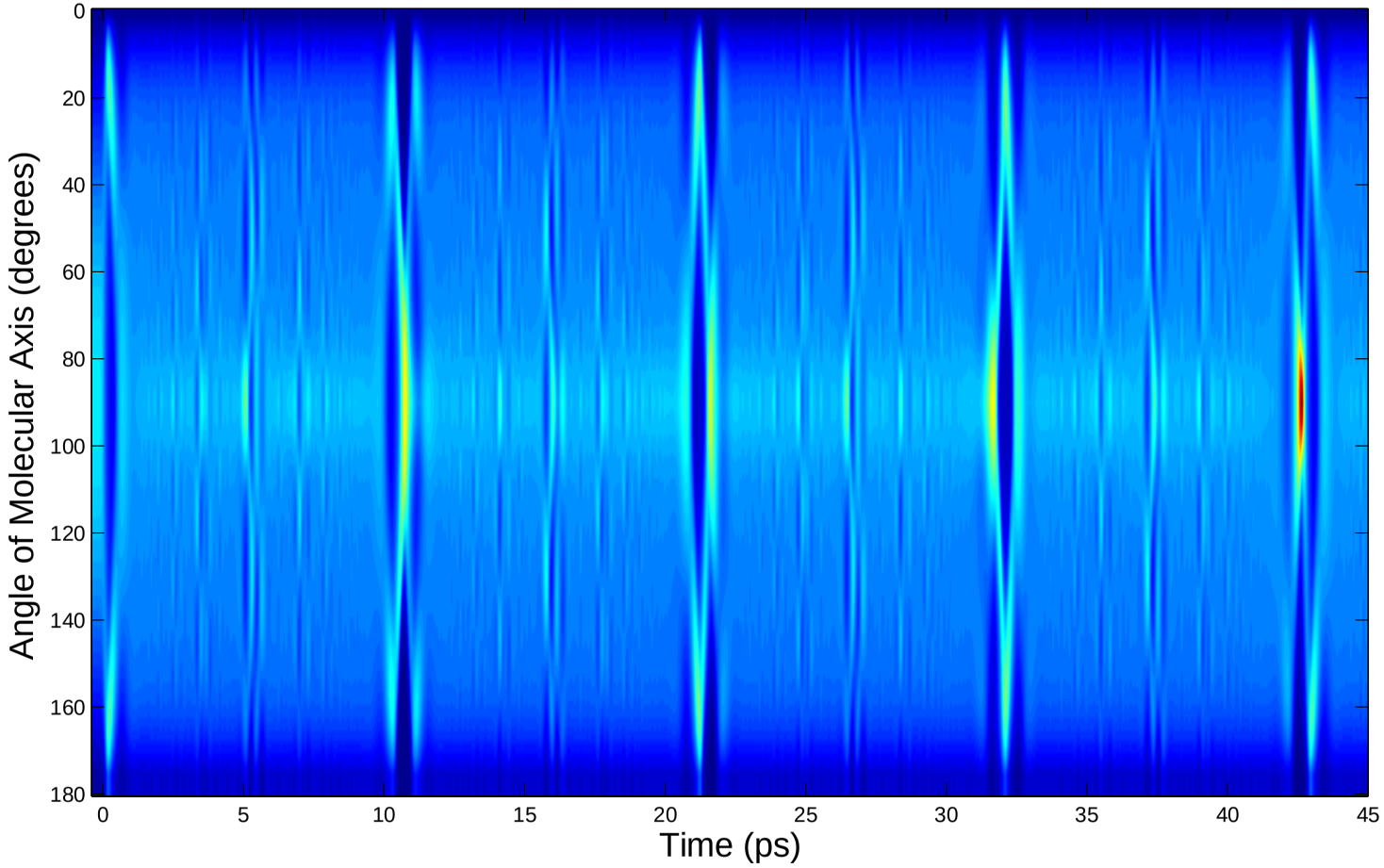

Figure 3.4: The angular density shown as a function of time for CO_2. The vertical axis is the polar angle with respect to the pump polarization and the horizontal axis is the time evolution of the wave packet. One full period of the wave packet is shown. The initial alignment, 1/4, 1/2, 3/4, and full revival can be seen at 0, 11, 22, 33, 44 ps respectively. There are also a number of smaller features between the revivals

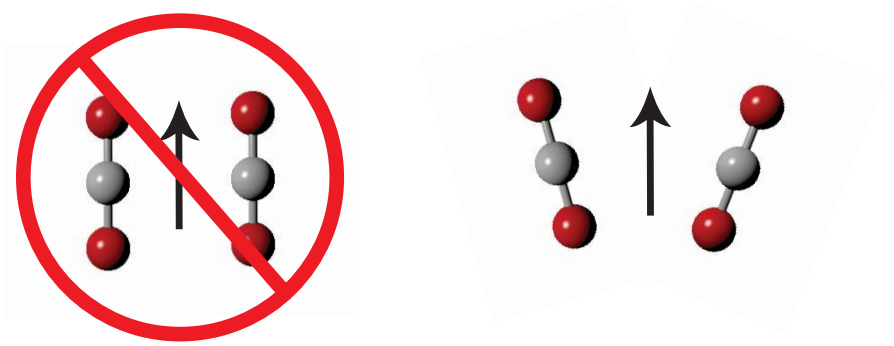

Figure 3.5: An illustration emphasizing that one need to consider the weighted alignment distribution with the azimuthal angle integration completed, as opposed to the full angular density. The weighted alignment distribution shows that most of the molecules are not pointed along the polarization axis, even at maximum alignment.

by looking at the angular density near the 1/2 revival in CO_2, shown in figure 3.6.

3.6 Molecular Alignment and Nuclear Spin Statistics

In molecules consisting of identical atoms, such as diatomics, the rotational wave packet can vary significantly from one molecule to the next. This difference is due to nuclear spin statics and how they affect the populations of even and odd rotational levels[29]. Consider N_2 as an example. The nitrogen-14 nuclei have a spin of 1 and are bosons. Therefore the total molecular wave function must be symmetric upon exchange of the nuclei. The wave function can be divided into electronic, rotational, and nuclear spin parts.

$$\psi_{total} = \psi_e \psi_{rot} \psi_{spin} \tag{3.13}$$

The electronic part is symmetric because nitrogen has a σ orbital. The rotational states are antisymmetric for odd J and symmetric for even J. Because the nuclear spin is 1, the nuclei have 9 possible spin states: 3 are antisymmetric and 6 are symmetric. All of these states are populated equally at experimental temperatures. Because the total wave function must be symmetric, symmetric spin functions are paired with even-J rotational functions, and anti symmetric spin functions with odd-J rotational functions. This pairing causes even-J rotational states to be populated in a 6:3 ratio compared to odd-J states.

The rotational excitation has selection rules of $J = J' + 0, \pm 2$ and $M = M'$. So the initial thermal/spin-weighted ratio of even to odd rotational states is maintained in the wave packet. Molecules with different nuclear spins and electronic symmetries have different ratios, shown in table 3.2. When calculating the rotational wave packet, the initial thermal distribution of state is created with ratio of even and odd state appropriate for the molecule. The ratio is maintained because the excitation does not

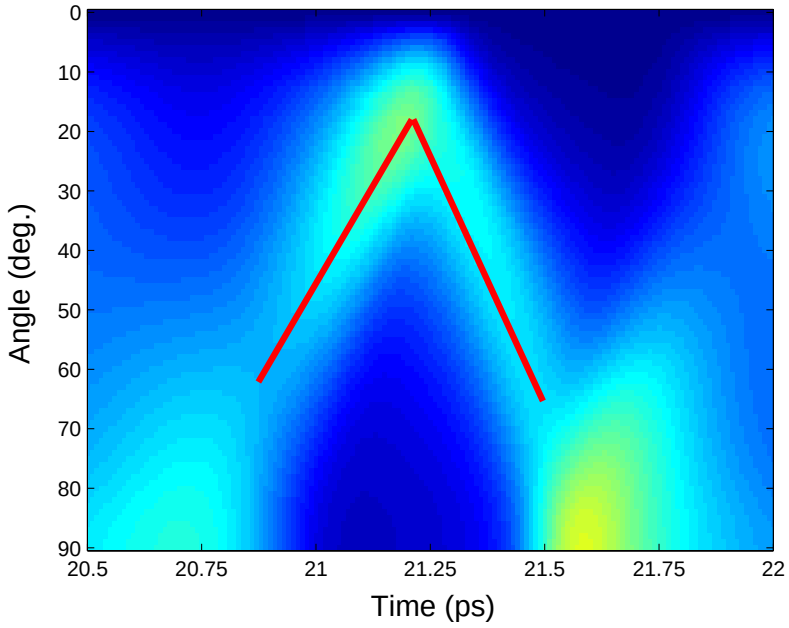

Figure 3.6: The angular density near the 1/2 revival in CO_2. The red line shows where the wave packet is localized and sweeps through angular positions.

mix even and odd rotational states.

Molecule	even	odd
N_2	2	1
O_2	0	1
CO_2	1	0
N_2O	1	1

Table 3.2: The ratio of even and odd rotational state populations for several common molecules.

The ratio of even and odd rotational states affects the character of the wave packet, as is shown in figure 3.7. The main difference is in the quarter revivals. The N_2O molecule has no symmetry because the oxygen atom is on one side of the linear molecule. Because of this lack of symmetry, even and odd states are populated equally. The main effect of this is that no quarter revivals appear in the time evolution of the $< \cos^2\theta >$. Oxygen and carbon dioxide have inverted structures at the quarter revivals, and nitrogen has quarter revivals which are reduced in magnitude. At the quarter revivals, even and odd states align separately and each alignment is 180° out of phase. So, when the even and odd states are equally weighted there is no net alignment and the $< \cos^2\theta >$ remains unchanged; however, the quarter revival is still present in the angular density.

3.7 Pump Intensity, Pump Duration, and Rotational Temperature

Typically, it is desirable to achieve the highest possible degree of alignment. The obvious way of doing this is to increase the pump intensity, which increases the population in high rotational states which allows for a sharper alignment. However, increasing the optical intensity too much causes other undesirable processes, such as multiphoton ionization, to turn-on. The energy content of the pump can also be increased by lengthening the duration of the pump pulse while keeping the intensity constant. The duration can be increased so long as the process is impulsive. A rule of thumb is to set

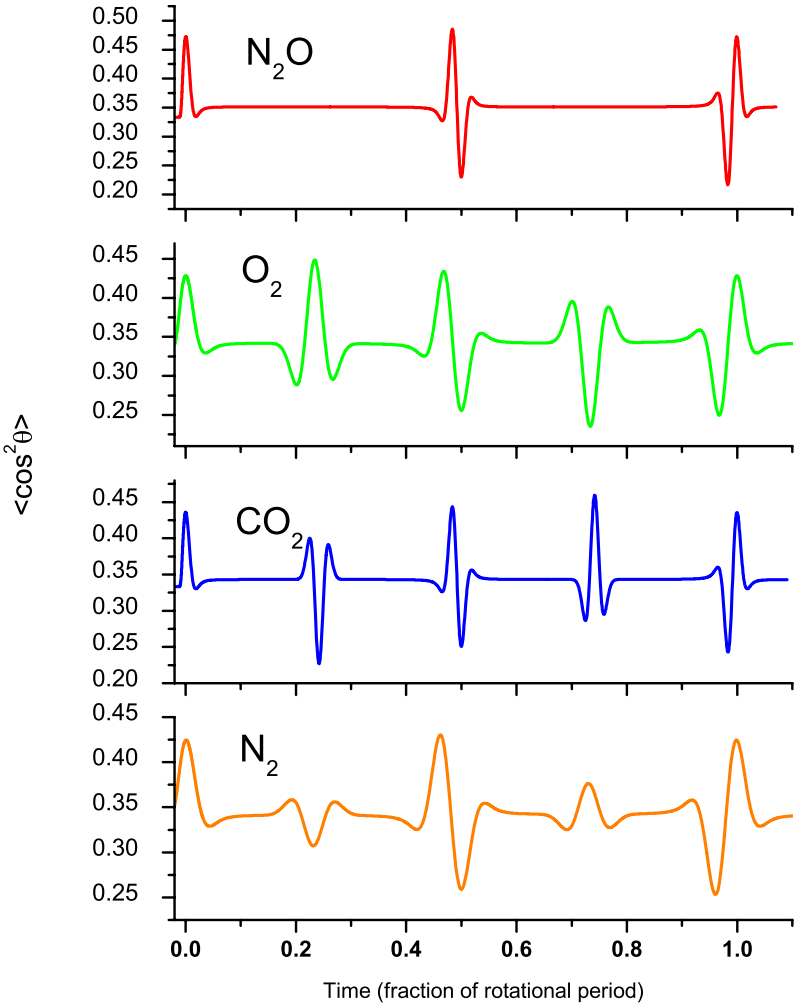

Figure 3.7: The effect of nuclear spin statistics is illustrated in the alignment parameter $< \cos^2\theta >$ for N_2O, O_2, CO_2 and N_2. The 1/4 revival can be reduced, inverted, or flipped depending on the ratio at which even and odd rotational states are populated.

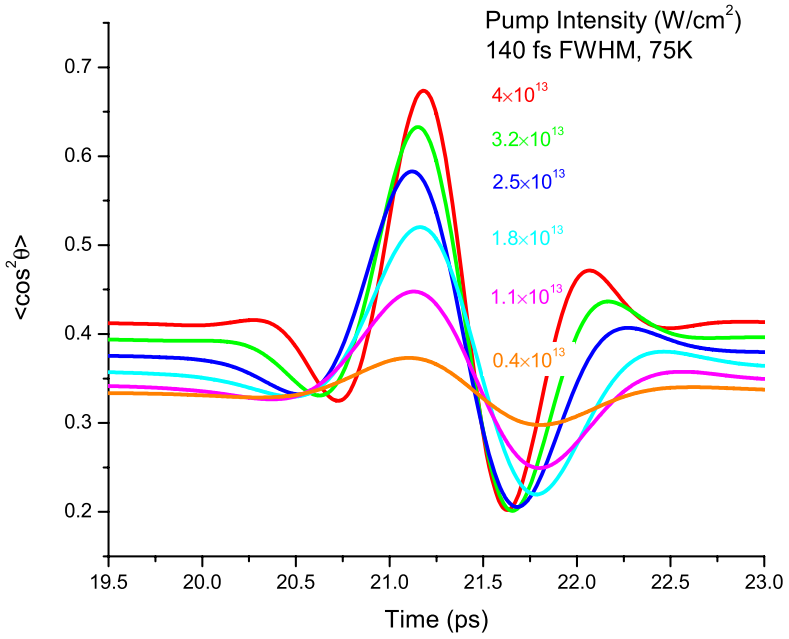

Figure 3.8: Alignment parameter for CO_2 around the 1/2 revival as a function of pump intensity. Increasing the pump intensity decreases the duration of the revival structure and increases the peak alignment.

the pump pulse duration at 1% of the rotational period of the molecule. The initial rotational temperature also has an effect of blurring out the alignment, so the maximum degree of alignment can be increased by lowering the initial rotational temperature. Commonly the intensity is high enough and the temperature low enough that the rotational states populated by the excitation are not already thermally populated. The temperature and intensity also affect the duration of the revivals as is shown in figures 3.8 and 3.9 . Higher temperatures and intensities lead to wave packets made of higher energy rotational states, which narrow the duration of the revival structures.

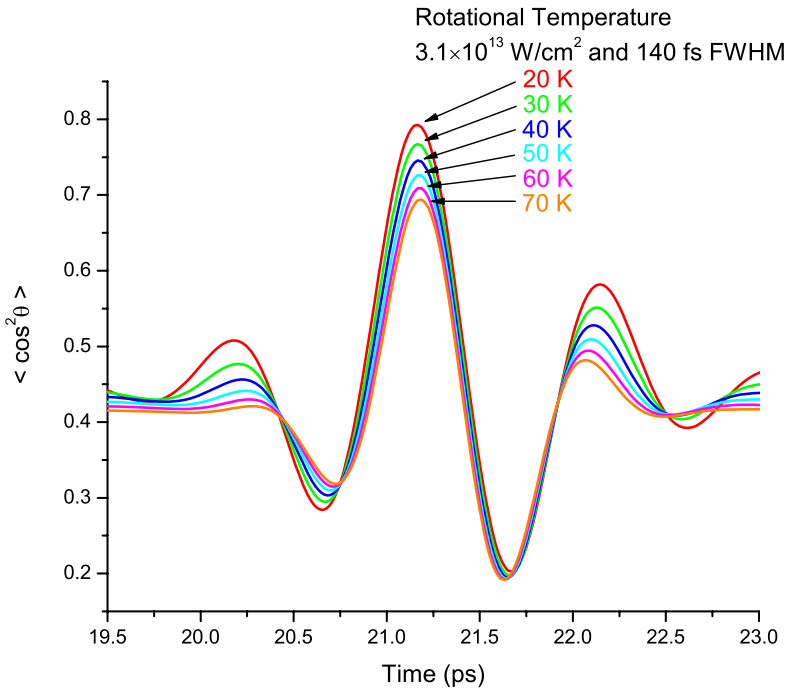

Figure 3.9: Alignment parameter for CO_2 around the 1/2 revival for several initial rotational temperatures. Decreasing the temperature increases the peak alignment.

Chapter 4

High Harmonic Generation from Rotational Wave Packets

One goal of using high harmonics to probe rotationally excited molecules is to understand how HHG emission varies with molecular orientation. Ideally, we would like to be able to align the molecules perfectly in one direction and then vary the polarization of the high harmonic generating field. This would allow us to easily see how the high harmonic emission varied with the molecule's orientation. The resulting angular dependence of high harmonic emission (or orientational dipole) could then be compared directly with theoretical calculations, and used to extract structural information about the molecule[30]. Unfortunately, because the molecules cannot be perfectly aligned, the orientational dipole cannot be retrieved simply by rotating the polarization; the averaging over the rotational distribution must be taken into account.

4.1 Averaging HHG Over Rotational States

Initially, we will consider a single harmonic order, q. The total high harmonic emission from the rotational wave packet is weighted by the angular density of the wave packet and integrated over all polar angles.

$$I_q(t) = \left| \int_0^{\pi} P(\theta, t) B_q(\theta) d\theta \right|^2 \tag{4.1}$$

The azimuthal integration has already been carried out using the cylindrical symmetry and is contained inside the angular density $P(\theta, t)$ along with the sinusoidal

weight. The orientational dipole $B_q(\theta)$ describes the angular dependence of high harmonic emission for harmonic order, q. In general, the orientational dipole can be a complex number and represents the amplitude and phase of the harmonic emission from a molecule oriented at the corresponding angle. In the above equation, we have ignored any harmonic emission polarized perpendicular to the fundamental polarization; this assumption is valid so long as the pump and probe polarization are parallel. When the pump and probe polarizations are parallel, perpendicularly polarized harmonics are not generated for symmetry reasons[23].

4.2 Intensity Measurements from Rotationally Excited CO_2

This section will report the measured intensity from rotationally excited CO_2, and relate the features in intensity modulation to features of the orientational dipole. CO_2 is used for two main reasons. First, it is relatively easy to achieve a strong alignment because it's anisotropic polarizability is larger than other small molecules. Additionally, it has a ionization potential of 13.8 eV, which means it generates a broad range of harmonic compared with lower ionization potential molecules. It is important to note that the ability to resolve features in the orientational dipole is limited by the maximum degree of alignment in the wave packet. Even with an alignment of 0.6 the CO_2 molecule is localized to only $\pm 15^\circ$.

The measured intensity of the 39^{th} harmonic is shown in figure 4.1a along with the alignment parameter for the rotational wave packet in figure 4.1b. The harmonic intensity is normalized to the harmonic intensity from isotropic CO_2. The main feature of the intensity modulation is the revival structure which occurs at the same delay time as those in the alignment parameter. The revival structure in harmonic intensity is anti-correlated with the alignment parameter. As the alignment parameter increases the harmonic intensity decreases, and when the intensity is maximum the alignment is smallest. This anti-correlated property suggests that the orientational dipole for CO_2

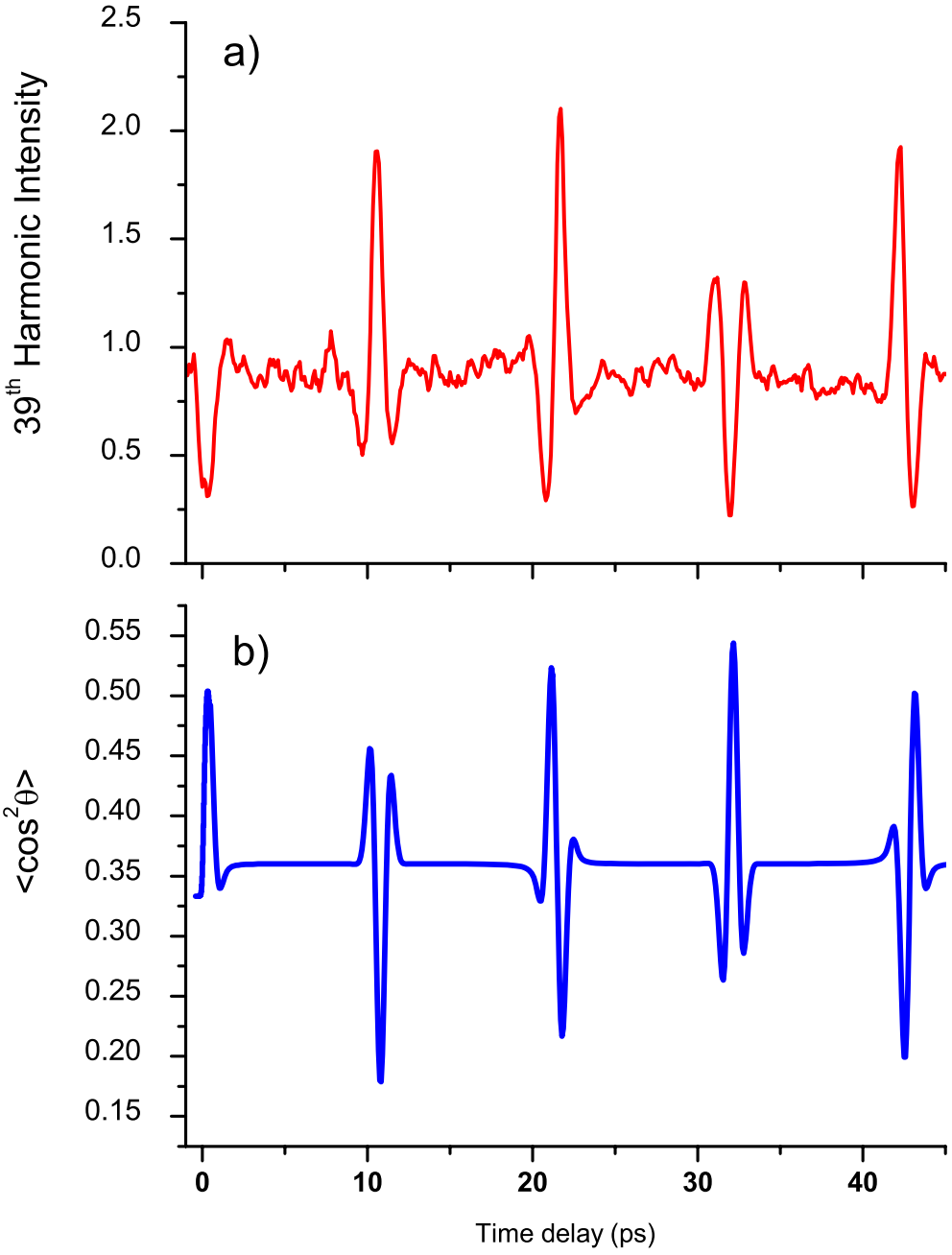

Figure 4.1: a) The measured intensity of the 39^{th} harmonic as function of time delay for CO_2. b) The calculated alignment parameter for this rotational wave packet. The harmonic intensity is anti-correlated with the alignment.

can be approximated as $1- < \cos^2\theta >$ as a first guess with a constant minus the alignment parameter. The negation will invert the revival structure in the alignment parameter which will match the HHG intensity modulation. In this data the maximum degree of alignment is $\sim$0.54.

However as we increase the intensity of the pump/alignment pulse (and consequently the degree of alignment) new features begin to appear. This can be seen in 4.2, where there are three new features: 1) A bump appears at the time of maximum alignment; 2) The intensity at anti-alignment becomes significantly stronger ($\sim 4\times$); and 3) The baseline intensity between revivals drops below the intensity corresponding to an isotropic distribution.

4.3 Origin of the Bump at Maximal Alignment

The bump can be explained by looking at how the angular distribution changes near the maximal alignment, as described in section 3.5 where the wave packet is localized, sweeps toward smaller angle and then returns. An important point is that the harmonic intensity goes almost to zero on both sides of the bump. There are two possible explanations for why the harmonic intensity would go to zero: 1) The wave packet is well localized, and the orientational dipole has a minimum which is seen as the localized wave packet sweeps through angular positions near maximal alignment. 2) There is a π phase shift in the orientational dipole, and the intensity goes to zero as the wave packet sweeps through the phase shift. The observed minima in the modulation could be due to either or both of these effects.

This explanation is illustrated in figure 4.3. The figure shows the magnitude and phase of a possible orientational dipole for CO_2. There is a minimum in the magnitude and a π phase jump around 30°. Also, shown is the angular density for a specific time delay. As the angular density evolves in time, it sweeps through 30° to maximum alignment and then sweeps back through 30°. The observed high harmonic intensity is

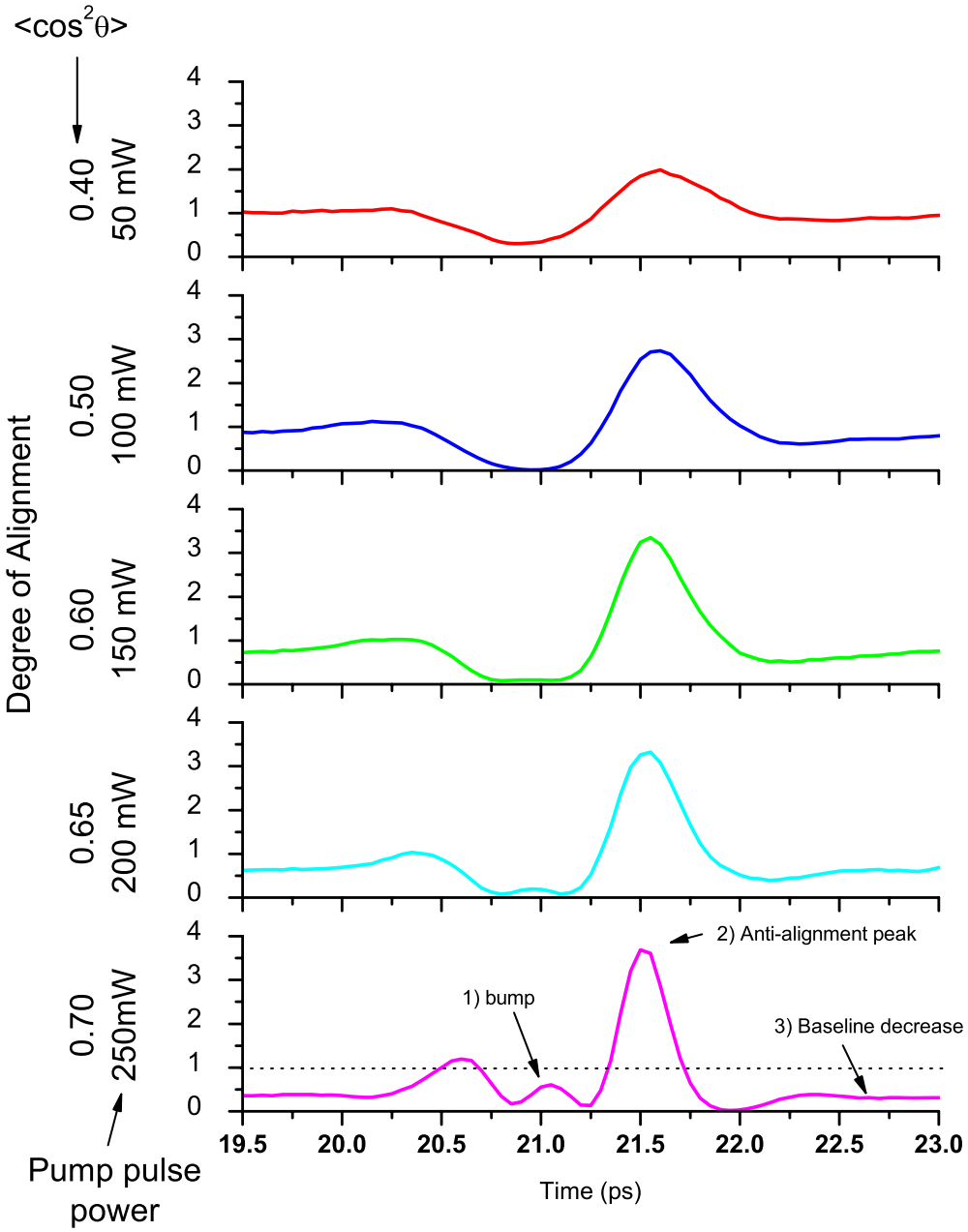

Figure 4.2: The intensity modulation of the 39^{th} harmonic is shown around the 1/2 revival in CO_2. As the degree of alignment of the rotational wave packet is increased several new features appear in the intensity modulation: 1) A bump appears at the point of maximum alignment. Showing that with sufficiently strong alignment the HHG emission again begins to increase. 2) The intensity at anti-alignment gets significantly stronger ($\sim 4\times$). 3) The baseline intensity between revivals drops below the isotropic intensity.

the integral of orientational dipole weighted by the angular density. A sharp alignment effectively selects a small part of the orientational dipole under the angular density. The minimum in the magnitude and the phase shift both could cause a minimum in the observed intensity.

4.4 Origin of the Anti-Aligned Peak

The bump when the molecule is aligned tells us about the orientational dipole at small angles (0°-45°); similarly, the peak of the modulation when the molecule is anti-aligned gives information about larger angles (60°-90°). As the power/intensity of the pump pulse is increased the peak near the anti-alignment becomes stronger and narrower. The angular density also becomes more localized around 90°. The high harmonic intensity is increasingly enhanced with higher degrees of anti-alignment (smaller $< \cos^2\theta >$ as is shown in figure 4.2. Because there are no features on the peak, this is indicative of the orientational dipole increasing towards 90°. If the orientational dipole decreased near 90°, we would expect a small dip to appear at the top of the peak.

4.5 Origin of the Baseline Reduction

This third feature of a reduced baseline between revivals indicates a phase shift in the orientational dipole. The angular density is not isotropic between revivals, because the rotational excitation populates many higher J-states; however, the magnetic quantum number M is unchanged by the excitation and still reflects the thermal distribution after the pump pulse. This leads to a weakly aligned state between the revivals. This is the reason the $< \cos^2\theta >$ is slightly larger than 1/3 between the revivals. Compared to an isotropic distribution, the angular density between revivals is shifted toward smaller angles as shown in figure 4.4. Between the revivals, the high harmonic intensity can be dramatically decreased. For some orders, the high harmonic intensity is less than half the isotropic intensity. How can a small shift toward smaller angle lead to a dra-

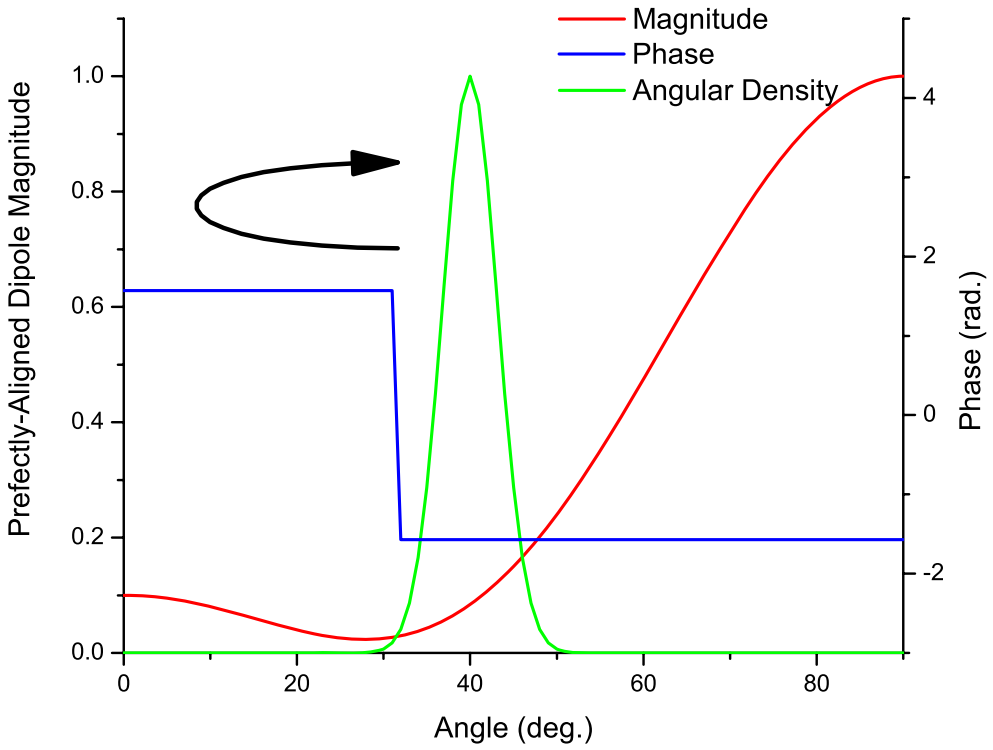

Figure 4.3: A cartoon graphic illustrating the origin of the "bump" during maximal alignment. The angular density sweeps through the minimum or phase shift causing a minimum in the high harmonic intensity. A second minimum is created as the angular density sweeps back in the opposite direction. There is a bump between the two minima.

matic drop in intensity? If the HHG where incoherent, this dramatic effect would not be possible. However, if there is a π phase jump in the orientational dipole, this dramatic decrease makes sense. The slight shift toward smaller angles weights each side of the π phase jump more equally and contributions from each side of the phase jump destructively interfere leading to the reduced intensity between revivals.

4.6 Measuring the Phase

The intensity modulations in CO_2 are strongly suggestive of the π phase jump in the orientational dipole. If this is the case the bump would correspond to harmonic emission which is 180° out of phase compared with emission from other time-delays. It is desirable to confirm this by measuring the phase of the harmonic emission, and this was done using two different methods. First, we used gas mixtures where an atomic gas is used as a reference emission. And second, we directly measured the phase using a interferometric double focus arrangement. One focus is used as a reference and directly interferes with emission from the other focus.

4.7 Using Gas Mixtures to Measure the Phase of Molecular HHG

To measure the phase we use a mixture of an atomic and a molecular gas. The pump pulse will only rotationally excite the molecular gas. As the emission from the molecular gas evolves with the rotational wave packet, the emission from the atomic gas remains constant and can be used a reference to determine the relative phase of the emission from the molecular gas.

Consider a mixture of an atomic (Kr) and a molecular (CO_2) gas. The emission intensity of a single harmonic order (n) resulting from the mixture is then the coherent sum of the emission from both species.

$$I_q(a) = |aD_{CO_2}\exp(i\phi_{CO_2}) + (1-a)D_{Kr}|^2 \tag{4.2}$$

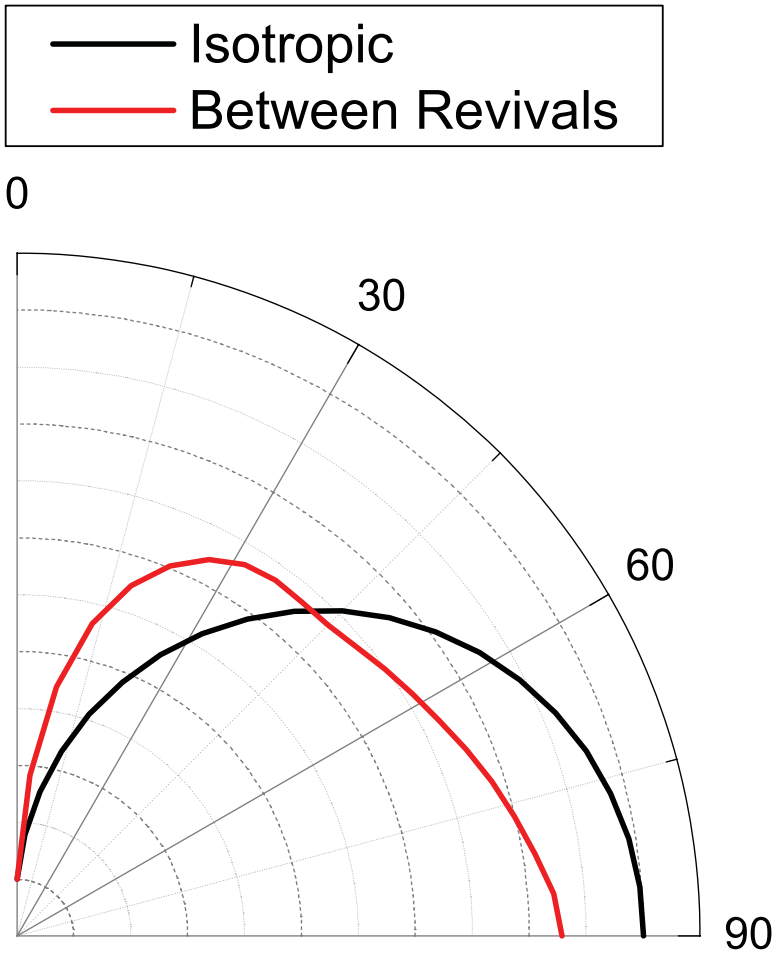

Figure 4.4: The angular density for the isotropic case (no excitation) (Black) and for time-delays between revivals (Red). The distribution is shifted to smaller angles between revivals.

$$I_q(a) = a^2 D_{CO_2}^2 + (1-a)^2 D_{Kr}^2 + 2 D_{CO_2} D_{Kr} a(1-a)\cos\phi_{CO_2} \tag{4.3}$$

Here D_{CO_2} and D_{Kr} are the magnitudes of the electric field emitted from CO_2 and krypton respectively, while ϕ_{CO_2} is the phase of the emission from CO_2 relative to krypton. The experimentally controllable parameter is the molar fraction of CO_2, a. After exciting the rotational wave packet in CO_2, the magnitude (D_{CO_2}) and phase (ϕ_{CO_2}) of the harmonic emission depends on the wave packet evolution and will vary with the time delay between the pump alignment pulse and probe harmonic-generation pulse.

The total emission from CO_2 is a coherent sum of dipole responses from molecules distributed over many angular orientations. The orientational dipole response must therefore be weighted by the rotational wave packet probability density to determine the molecular contribution to the harmonic emission.

$$D_{CO_2}(t)\exp(i\phi_{CO_2}(t)) = \int_0^\pi B(\theta)P(\theta,t)\sin\theta d\theta \tag{4.4}$$

The rotational wave packet angular probability density is well understood and can be calculated[45]. It is therefore possible to retrieve the orientational dipole from the measured time-dependent harmonic emission from rotationally excited molecules and atomic gas mixtures. The orientational dipole $B(\theta)$ can be thought of as the complex harmonic dipole from perfectly aligned CO_2. Harmonic generation from a rotationally excited wave packet combines emission from many orientations of the molecule. Therefore, measuring only the intensity of the harmonic signal is insufficient to retrieve the orientational dipole $B(\theta)$.

Figure 4.5a shows the intensity of the 31^{st} harmonic as a function of time delay between the alignment and harmonic generating beams, for mixture ratios of 0%, 19.1%, 41.0%, 78.7% and 100% of CO_2 with Kr. (We have switched to the 31^{st} harmonic

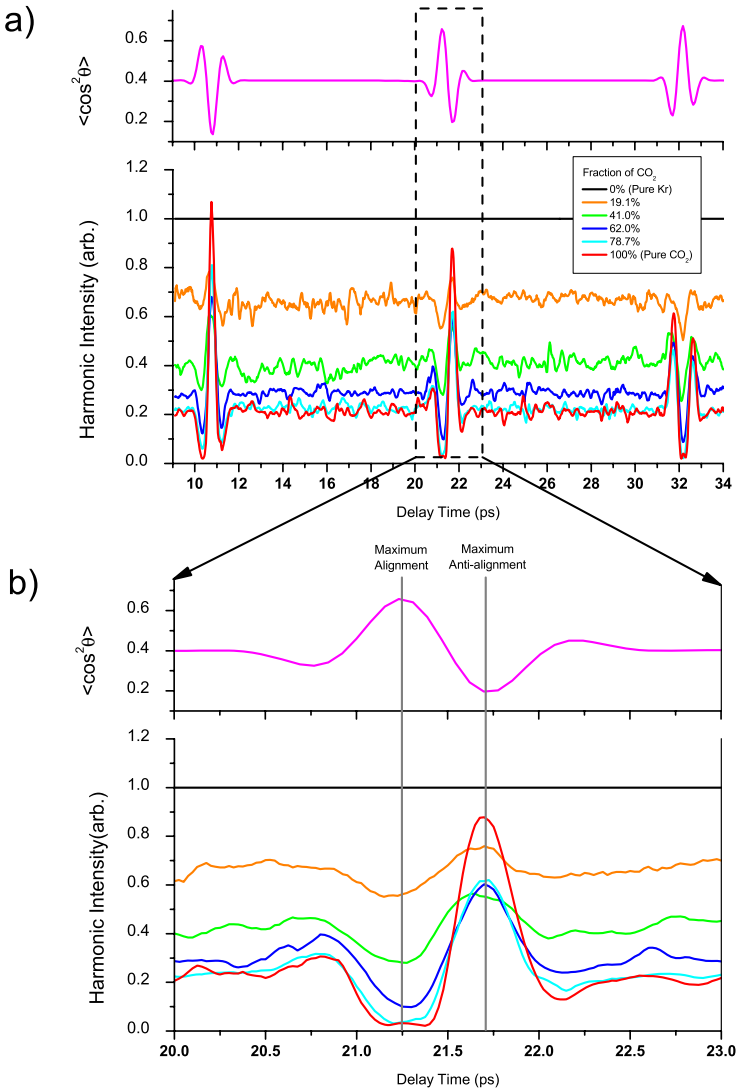

Figure 4.5: a) The upper plot shows the calculated alignment parameter for the rotational wave packet. The lower plot shows the HHG intensity for the 31^{st} harmonic from Kr:CO_2 mixtures plotted against the time delay of the pump and probe pulses for several mixture ratios as stated in the legend. b) Same as above, however, expanded near the half revival.

because for this dataset the 31^{st} harmonic is less noisy than the 39^{th} harmonic.) The range of time delays in Fig. 4.5a corresponds to the first three revivals of the rotational wave packet in CO_2. The pure Kr curve (black) shows no noise because it was measured from a single spectrum and does not vary with delay time. In the case of pure CO_2 (red curve), several additional features not seen in other experiments with CO_2 are apparent, particularly at the peak of the alignment (time delays where $< \cos^2\theta >$ is maximized; i.e. 21.25 ps delay) where the harmonic intensity increases slightly from the minima on each side. This is due to the higher degree of alignment in this experiment ($< \cos^2\theta > = 0.67$) compared with previous experiments ($< \cos^2\theta > = 0.6$)[32][64] as explained in section 4.3. As the fraction of CO_2 is decreased, the amplitude of the modulation decreases as expected; however, the shape of the modulation changes significantly as well. In pure CO_2 (red curve) at the revival, the enhancement (with respect to the signal between revivals) is three times as strong as the suppression. When the CO_2 fraction is reduced to 19.1% (orange curve), both the enhancement and suppression are of the same magnitude. This suggests that the EUV emission from CO_2 changes phase during the revival. This can be seen more clearly in Fig. 4.6a, which shows the harmonic intensity as a function of CO_2 fraction at two time-delays - corresponding to best alignment (harmonic suppression, red curve) and best anti-alignment (harmonic enhancement, blue curve) near the half revival.

The data shown in Fig. 4.6 was fit to Eqn. 4.3 using a least squares procedure. The magnitude and the phase of the CO_2 dipole were used as fit parameters. Figure 4.6a shows the experimental data as squares, while the fit to the data is shown as solid lines. Because the magnitude of the dipoles of Kr and CO_2 can be measured directly in a pure gas, it is possible to subtract the first and second terms in Eqn. 4.3 from the data, and investigate only the 3^{rd} term that is responsible for interference. Figure 4.6b plots the same data as in Fig. 4.6a with the first and second terms subtracted and then normalized with respect to the magnitude of emission from each species. In this graph, constructive

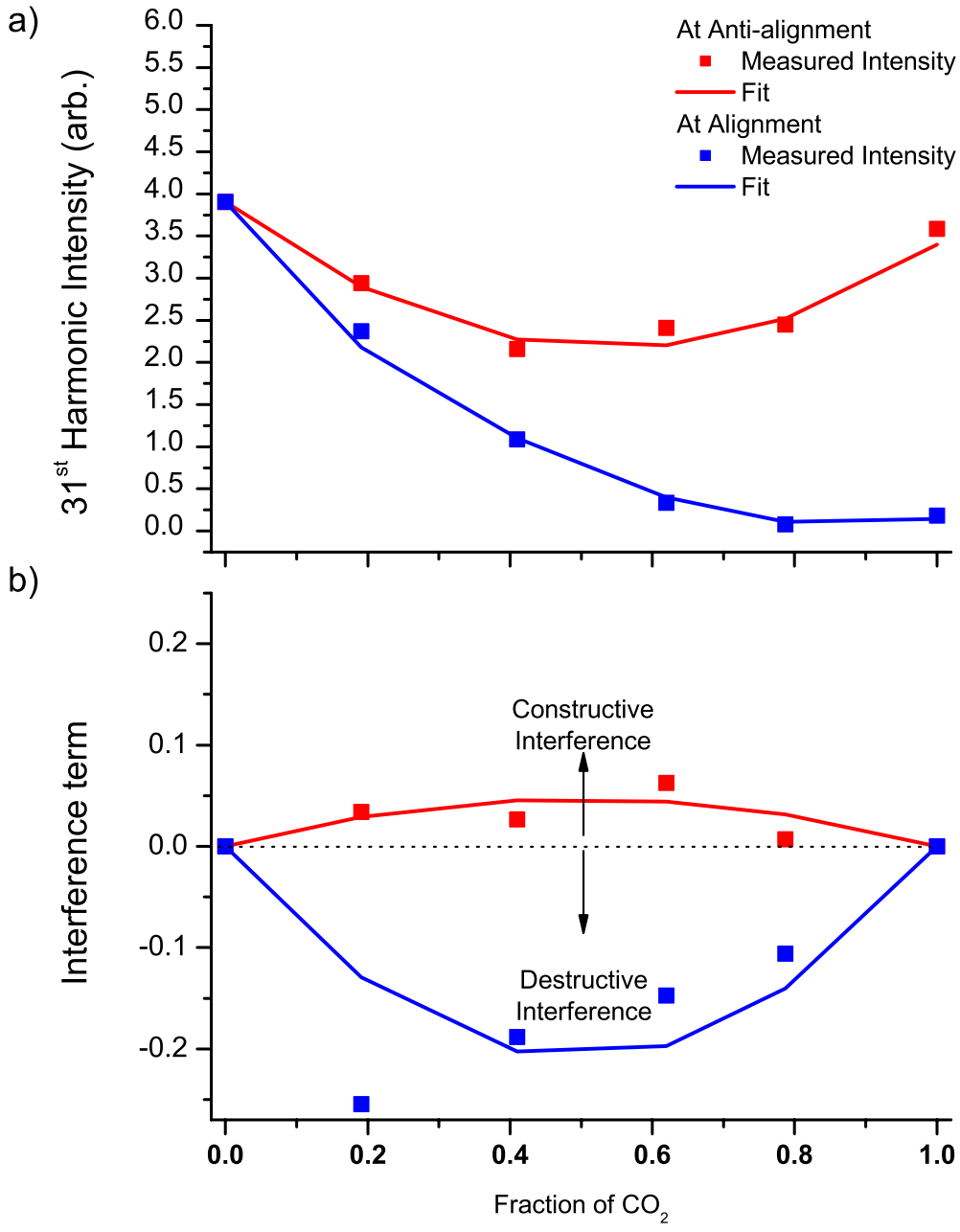

Figure 4.6: a) The intensity of the 31^{st} harmonic plotted against the fraction of CO_2 in the mixture at two time delays: 21.75 ps and 21.25 ps corresponding to the maximum anti-alignment and alignment during the revival. b) The 3^{rd} term of eqn. 4.3 plotted against the fraction of CO_2 for the same two time delays.

interference between the Kr and CO_2 harmonic emissions corresponds to positive values, while destructive interferences correspond to negative values. The data clearly show that when CO_2 is aligned, the harmonic emission interferes destructively with that from krypton, while when anti-aligned, the interference is constructive. This least-squares fitting procedure was applied to all measured time-delays, and the magnitude and phase of the harmonic emission is displayed in Fig. 4.7. We can see that when the CO_2 is approximately isotropically distributed (at time delays between revivals), the emission from CO_2 is 90° out of phase from that of Kr. However, when the CO_2 is aligned, the total harmonic emission is suppressed, and the phase difference between the emissions from the two species approaches 180° .

At any time delay, the harmonic emission from CO_2 results from a superposition of emissions from different molecular orientations that are distributed in a rotational wave packet. The total (rotationally averaged) emission can be calculated from Eqn. 4.4. We can apply a least squares fitting procedure a second time to determine the magnitude and phase of the orientational dipole $B(\theta)$, which is the nonlinear harmonic response from a perfectly-aligned molecule. To accomplish this, we expand $B(\theta)$ as a series of Legendre polynomials -

$$B(\theta) = c_0 + c_1 \cos^2\theta + c_2 sin^2 2\theta \tag{4.5}$$

where c_0 , c_1 , and c_2 are the fit parameters. Such an expansion has been used previously in other experimental and theoretical work[21][31]. The angular distribution is never particularly sharp in impulsively excited rotational wave packets (the FWHM of the CO_2 distribution is 15° at the maximum alignment and 60° at the maximum anti-alignment under our experimental conditions of a rotational temperature of 70 K, and a pump pulse peak intensity of 3.8×10^{13} W/cm^2 with a duration of 140 fs FWHM.) Therefore, we limited our expansion to three terms. The fit parameters c_0 , c_1 , and

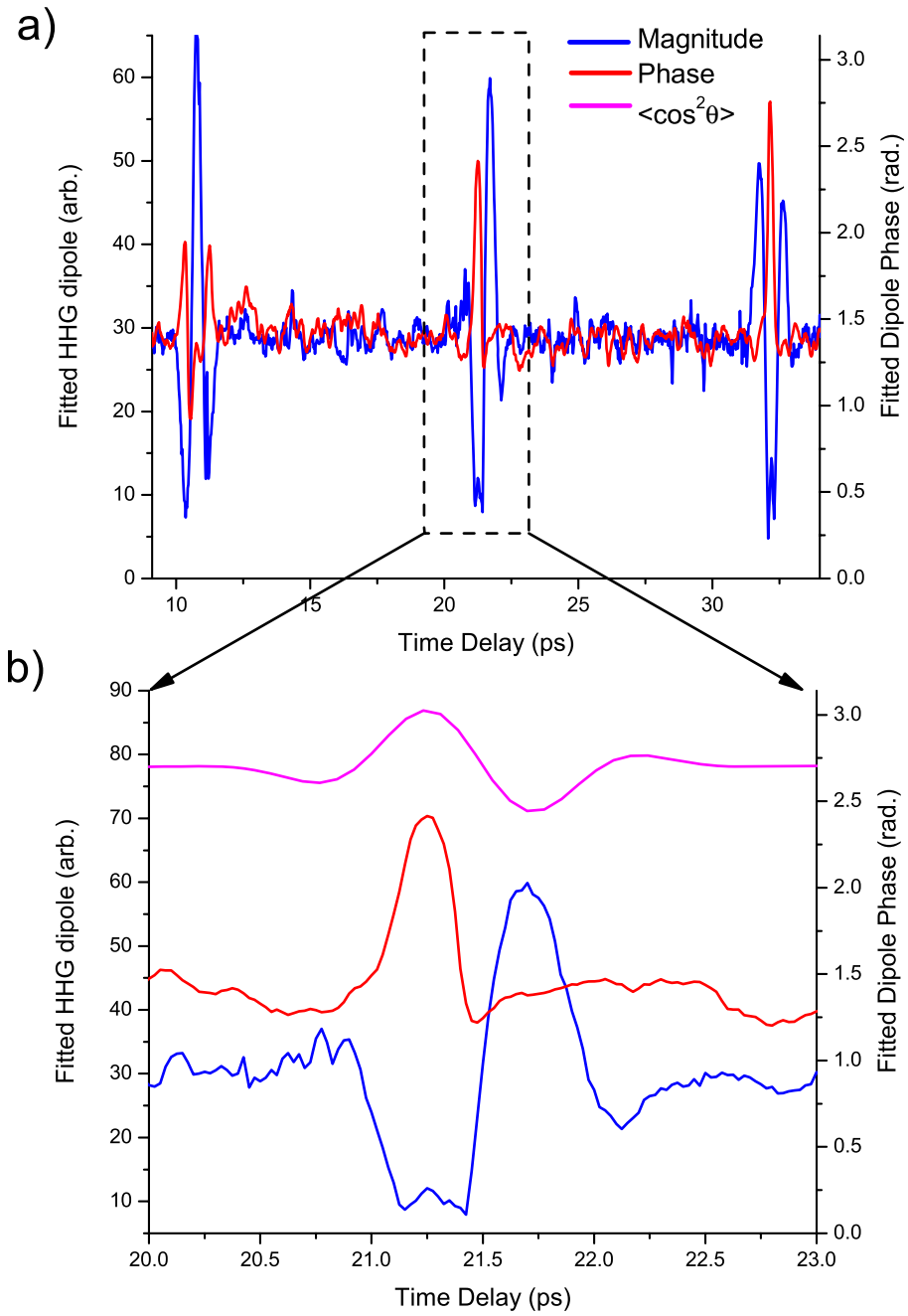

Figure 4.7: a) The magnitude (blue) and phase (red) of the dipole of CO_2 retrieved by fitting the intensity from several mixtures to Eqn. 4.3. b) Same as above, however, magnified near the half revival. The alignment parameter is also plotted for reference.

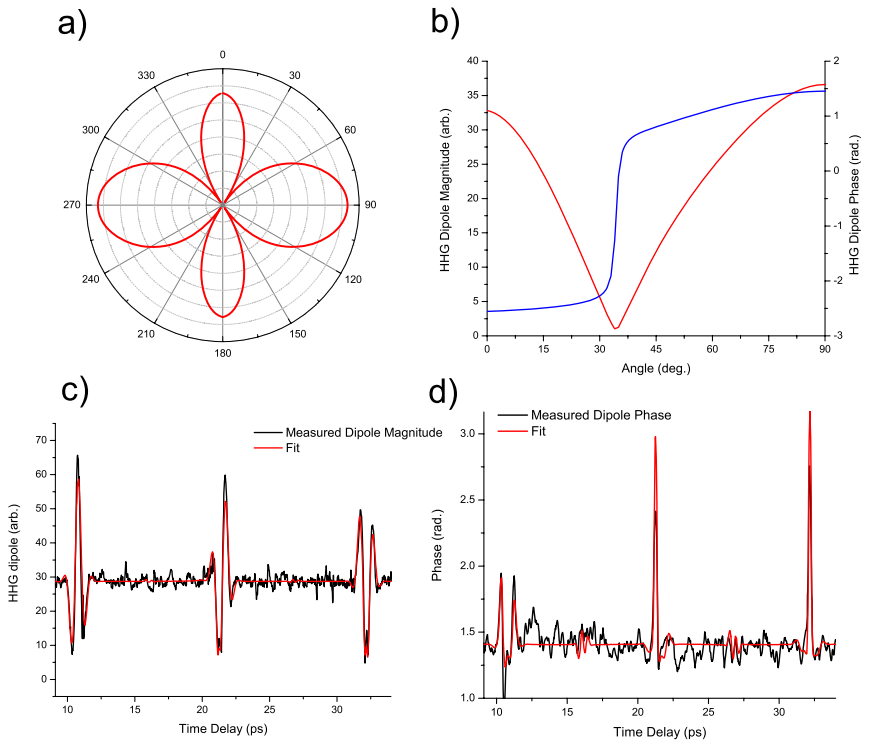

Figure 4.8: a) The magnitude of the orientational dipole retrieved by fitting to Eqn. 4.4 plotted against the molecular orientation. b) The magnitude and phase of the orientational dipole retrieved from the 2^{nd} fitting procedure c) The magnitude of the time dependent dipole and the fit. d) The phase of the time-dependent dipole and the subsequent fit.

c_2 are allowed to take on complex values because the orientational dipole $B(\theta)$ and the total time-dependent dipole from the first fit are complex, whereas the rotational angular density $P(\theta, t)$ is real and positive. This effectively gives 6 real-valued fit parameters. The expansion in terms of Legendre polynomials requires that the orientational dipole have mirror symmetry about the 0° and 90° axes - the same as the molecular structure. Figure 4.9 shows the Legendre polynomial fit to the data for the 31^{st} harmonic order. The retrieved orientational dipole $B(\theta)$ magnitude and phase are shown in Fig. 4.9 (a) and (b). The retrieved orientational dipole shows a π phase shift at 30° , corresponding to a minimum in the magnitude of $B(\theta)$. The fit to the magnitude and phase of the rotationally averaged emission from the first fitting step is also shown in Fig. 4.8.

Our analysis up to this point has concentrated on the emission from the 31^{st} harmonic order. Ideally we would perform the same analysis for all observed harmonic orders. In practice, however, we are limited to harmonic orders that have sufficient intensity to achieve a good signal-to-noise ratio. Figures 4.9 (a) and (b) show the results of a fit to the orientational dipole magnitude and phase for harmonic orders 21-35. In each harmonic order, the data show a minimum in the magnitude of $B(\theta)$, and a corresponding phase shift at the position of the minimum. As the harmonic order increases, the angular position of the minimum in the orientational dipole $B(\theta)$ moves from smaller angles to larger angles, while the depth of the minimum increases. The size and sharpness of the phase shift also increase with harmonic order. The two highest observed harmonic orders, 33 and 35, do not follow this trend as closely. The minima seen in our data are in agreement with the results of Vozzi[64], who also observed a minimum around 30° in the 31^{st} harmonic order intensity (the harmonic phase was not measured in that experiment).

The trends in the magnitude and phase of the CO_2 orientational dipole $B(\theta)$ that we extract from our data are similar to those predicted by the very simple and approximate two-center interference mode. This model assumes that the angular variation of

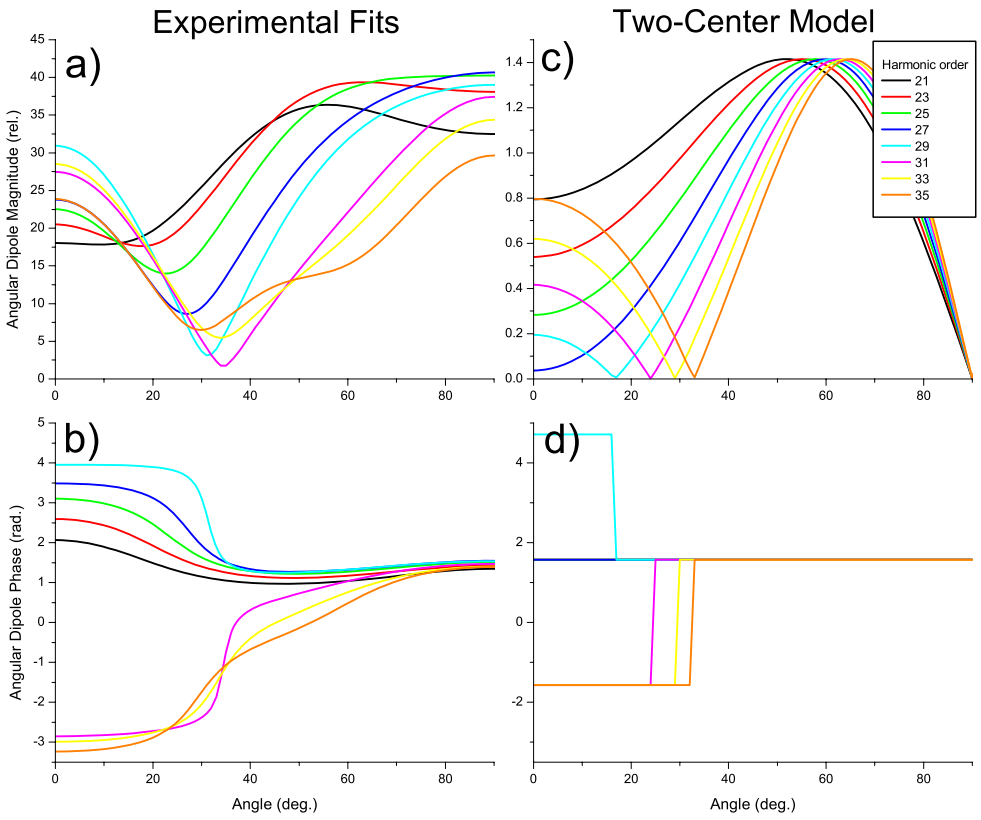

Figure 4.9: a) and b) The magnitude and phase of the orientational dipole retrieved from the 2^{nd} fitting procedure for harmonic orders 21-35. c) and d) the orientational dipole magnitude and phase predicted by the two-center emission model.

high harmonic emission for small molecules is dominated by the recombination of the electron with the molecule. This model was developed theoretically by Lein, et al[37] and explored experimentally by Kanai[32] and Vozzi[63]. In this model, the recombination step is modeled by approximating the returning electron as a plane wave. The orbital into which it recombines is modeled as two centers that are symmetric or anti-symmetric, depending on the symmetry of the molecule. If we assume the two centers are Dirac delta functions, the angular variation of the orientational dipole magnitude and phase can be calculated from Eqn. 4.6 and 4.7 (for the anti-symmetric case).

$$|B(\theta)| \propto \sqrt{1 - \cos\left(\frac{2\pi R}{\lambda_q}\cos\theta\right)} \tag{4.6}$$

$$\phi(\theta) = \frac{\pi}{2} \times \mathrm{sgn}\left(\sin\frac{2\pi R}{\lambda_q}\cos\theta\right) \tag{4.7}$$

The distance between the two centers is R. In CO_2 this corresponds to the distance between the two oxygen atoms, 0.232 nm. The electron wavelength is directly related to the harmonic order q by: $\lambda_q = 2\pi\hbar/\sqrt{2m(q\hbar\omega - I_p)}$ where m is the mass of an electron, ω is the frequency of the fundamental, and I_p is the ionization potential of the molecule. We have calculated the electron wavelength as described by Vozzi[64], and the results are shown in Figs. 4.9 (c) and (d), respectively. An angular minimum and phase shift first appear for the 27^{th} harmonic order, and increase in angle with harmonic order.

We note that in this analysis, we consider only the microscopic dipole, while neglecting the propagation phase of the harmonic light (e.g. phasematching effects) and any harmonic emission from molecules that is polarized perpendicular to the fundamental driving laser. These are reasonable assumptions for short interaction lengths $\sim$0.4 mm and low densities of $\sim 7 \times 10^{17}$ molecules/cm^3. Moreover, we observe strong destructive interferences in our data indicating that the harmonic emission from the Kr and CO_2 are polarized parallel to one another.

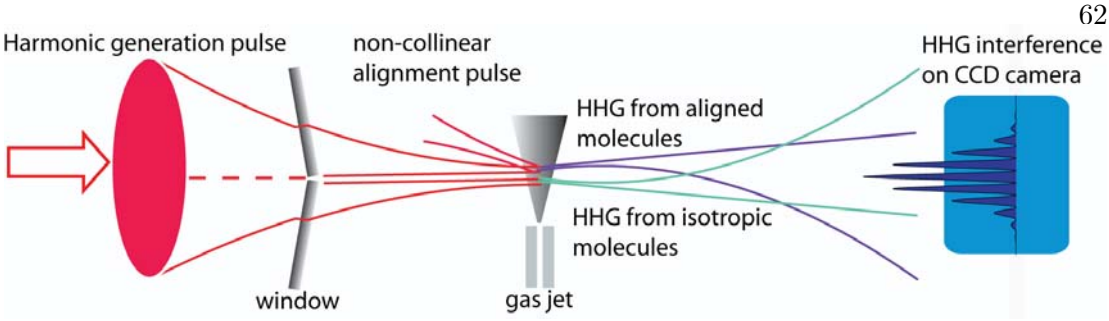

Figure 4.10: Setup for directly measuring the intensity and phase of high harmonic emission from molecules. The two foci are 240 μm and 110 μm away from the gas jet orifice respectively. The diameter of the gas jet is 150 μm and the backing pressure is 700 torr. HHG from aligned and randomly oriented molecules from two different regions of a gas jet interfere in the far field.

4.8 Direct Phase Measurement

We have also measured the phase of the EUV emission from CO_2. This was done using a double focus geometry as shown in figure 4.10. The high harmonic probe beam is split into two using two glass plates. The glass plates spatially separate the halves of the beam and each beam focuses to a separate spot on the gas jet. The high harmonic emission from each spot then overlaps and interferes on the camera. The interference pattern is along the non-spectral dimension of the spectrometer. A non-collinear pump is used to pump only one of the high harmonic generation spots. Any phase difference between the high harmonic emission from each spot is seen as a shift in the interference pattern on the camera.

The interference patterns for the 27^{th} and the 33^{rd} harmonics are shown in figure 4.11. The pump-probe time delay corresponds to the 3/4 revival in CO_2. Figures 4.11 a and c show the interference pattern along the vertical axis and time delay along the horizontal axis. A shift of the interference pattern is clearly seen for the 33^{rd} harmonic for time delays corresponding to maximal alignment. This phase shift is also exactly π. No phase shift is seen in the 27^{th} harmonic. Figures 4.11 b and d show lines of the interference pattern for time delays corresponding to the phase shift, and show the

phase shift more clearly. No phase shift is seen in harmonic orders below the 29^{th} while those above the 29^{th} exhibit a π phase shift.

Using this method the phase is measured relative to phase of the emission from isotropic CO_2. In contrast using the gas mixtures, the phase was measured relative to emission from krypton. This point is relevant only when looking at the phase as a function of harmonic order. When we look at the phase as a function of time-delay in the rotational wave packet or the phase of the orientational dipole for a specific harmonic order, relative measurement will only add a constant term to the phase.

This π phase shift suggests that the emission from CO_2 can be described as a real number instead of a complex number. A π phase shift is simply a change from a positive number to a negative number. Because the angular density is also a real positive number, Eqn. 4.4 restricts the orientational dipole to real number as well. The phase shift also occurs at the same time delays as the bump described in section 4.3, which agrees with the explanation of the bump being due to a phase shift.

Additionally, if the orientational dipole is a real number and a π phase shift is observed in the time-delayed signal, then the intensity must go to zero when the phase jumps. This is because a real number must pass through zero to change sign. (A complex number can go around zero in the complex plane.) This is roughly in agreement with the experimental results shown in figure 4.2. There are minima at the places where the phase jump occurs and the minima are close to zero intensity. However there is a measurable high harmonic intensity at these minima. This problem with the measured intensity modulation interferes with the fitting procedure used to extract the orientational dipole. We have tried these fits and they don't produce convincing results. It seems the next step is to improve the measurement of the intensity modulations which will lead to better fit results.

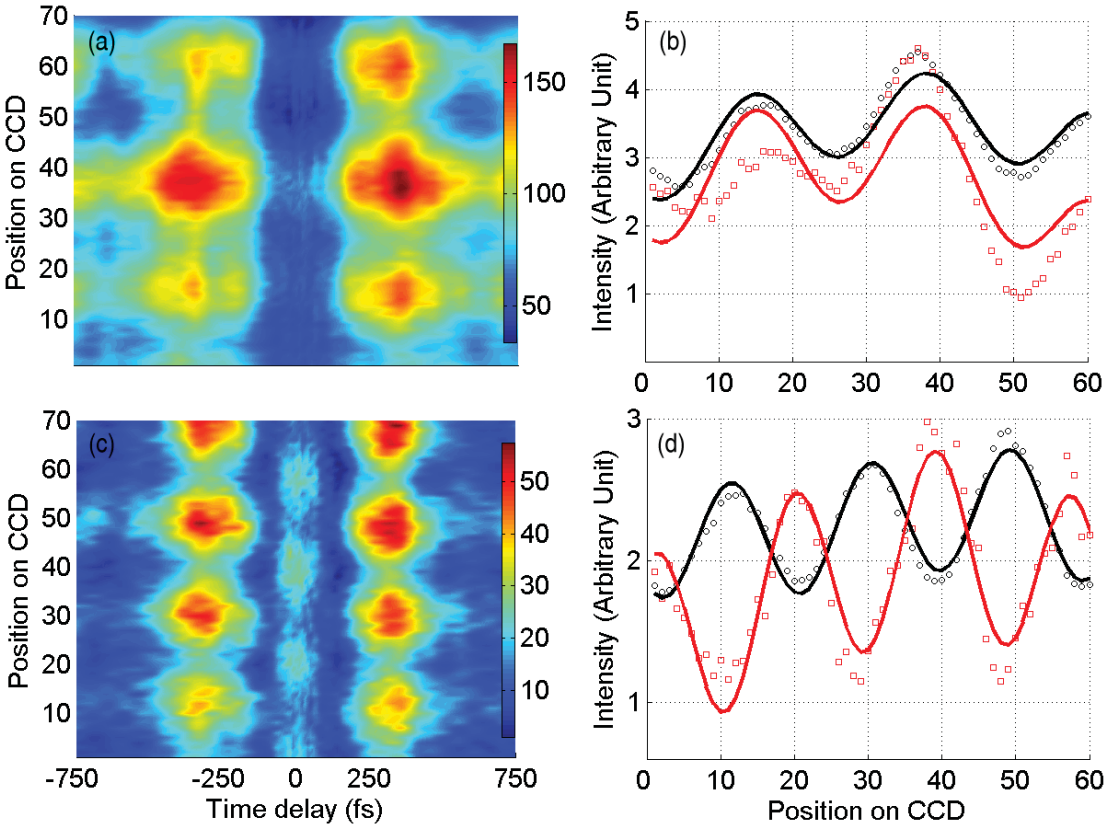

Figure 4.11: (a), (c) Interference pattern as a function of time within the 3/4 revival for harmonic orders 27 (a) and 33 (c). (b) Intensity-scaled integrated fringes for the 27^{th} harmonic in the -100 fs to 100 fs interval (red squares), along with least square fit (red solid line). Integrated fringes outside this temporal window are also shown (black circles) as well as a least square fit (black solid line). (d) Same as (b), but for the 33^{rd} harmonic. The time delay in (a) and (b) is relative to the center of the 3/4 revival.

4.9 Reconciling the Differences in Phase Measurements

The phase measured using the gas mixtures and the direct methods disagree significantly. Using the gas mixtures we saw a phase shift for every harmonic order and the magnitude of the phase shift varied greatly where the direct method gave a π phase shift for orders greater than 29. The phase shifts do occur at the same time-delays, namely when the molecules are maximally aligned; however, the mixtures method also sees some phase variation at the 1/4 revival during anti-alignment.

The direct measurement is more solid because it does not rely on intensity varying quadratically with mixture ratio and the direct method gives the unique result of an exact π phase shift. The phase shift would likely not be exactly π is there was a systematic error.

The variation of the intensity with mixture ratio is likely not completely described by Eqn. 4.3. This can be be seen in the phase variation around the 1/4 revival in fig. 4.5 where the fitted phase variation has a similar shape to the intensity modulation. It is possible the fitted phase variation has been contaminated with the intensity modulation.

There are several possible sources of error in Eqn. 4.3. First, the supersonic expansion of the gas jet changes significantly as the mixture ratio is adjusted: mainly the density and the rotational temperature. Second, the probe spot size may not be small enough to sample a uniform pump intensity. Then the high harmonic emission would be averaged over a distribution of rotational wave packets. Third, the high harmonic emission from a gas jet may not be completely coherent spatially. This incoherent part would not participate in the interference. Fourth, the observed discrepancy could be due to neglecting propagation and phase matching.

4.10 A Two Center Model of HHG from CO_2

Lein numerically investigated HHG in H_2 using an *ab-initio* calculation[37]. He observed minima and phase shift in the high harmonic spectrum, and explained these features in terms of a two center emission model. First, it is assumed that the recombination process dominates the orientational dependence of HHG while the ionization rate does not change significantly with polar angle. The two center model then tells us how the recombination amplitude varies with orientation of the molecule. The ground state wave function is approximated as two delta functions separated by the internuclear distance. These delta functions are either symmetric or antisymmetric depending on the symmetry of the molecular HOMO. The incoming electron is modeled as a plane wave.

$$a_r = \int \left(\delta(\mathbf{x} - R/2) \pm \delta(\mathbf{x} + R/2)\right) \mathbf{x} \exp\left(i\mathbf{k} \cdot \mathbf{x}\right) d\mathbf{x} \tag{4.8}$$

Here R is the internuclear distance and $\mathbf{k}$ is the propagation constant of the incoming electron plane wave. The dipole and the intensity for both the symmetric and antisymmetric cases are shown below.

$$d_{ant}(\mathbf{k}) = i \sin(0.5kR\cos(\theta)) \tag{4.9}$$

$$d_{sym}(\mathbf{k}) = \cos(0.5kR\cos(\theta)) \tag{4.10}$$

$$I_{ant} \propto \frac{1 - \cos(kR\cos(\theta))}{2} \tag{4.11}$$

$$I_{sym} \propto \frac{1 + \cos(kR\cos(\theta))}{2} \tag{4.12}$$

This model shows intensity extrema at angles such that the internuclear axis is equal to the electron wavelength projected onto the internuclear axis. These extrema are due the interference of the high harmonic emission from each center. The conditions for maxima and minima are shown below:(for an antisymmetric orbital the conditions are switched.) After passing through each minima there is an accompanying π phase shift.

$$R\cos\theta = (2m+1)\lambda/2 \tag{4.13}$$

$$R\cos\theta = m\lambda/2 \tag{4.14}$$

Determining the electron wavelength from the harmonic order is somewhat uncertain. Lein's calculations show that the effective wavelength of the electron is its wavelength at the bottom of the molecular potential, $\lambda_q = 2\pi\hbar/\sqrt{2m(q\hbar\omega)}$. However, experiments by Vozzi, et al. [64] showed better agreement with the wavelength of the electron in the continuum: $\lambda_q = 2\pi\hbar/\sqrt{2m(q\hbar\omega - I_p)}$.

This agreement was determined by looking at the high harmonic spectrum of aligned CO_2. The CO_2 aligns in the butterfly distribution and is mostly aligned at 30°. The minimum in the spectrum corresponds to the first destructive interference minimum. Figure 4.12 shows such data from our experiment. There is a clear minimum in the aligned spectrum at 31^{st} harmonic which agrees with the experiment by Vozzi[64] using the electron wavelength in the continuum. Additionally we have measured the high harmonic phase and we see no phase shifts for the 29^{th} harmonic and lower; however, we see π phase shifts for the 31^{st} harmonic and above.

An additional prediction of the two center model is that we will see the intensity modulation flip as we look at the emssion from higher harmonic orders. At an interference maximum the high harmonic intensity will be correlated with alignment instead

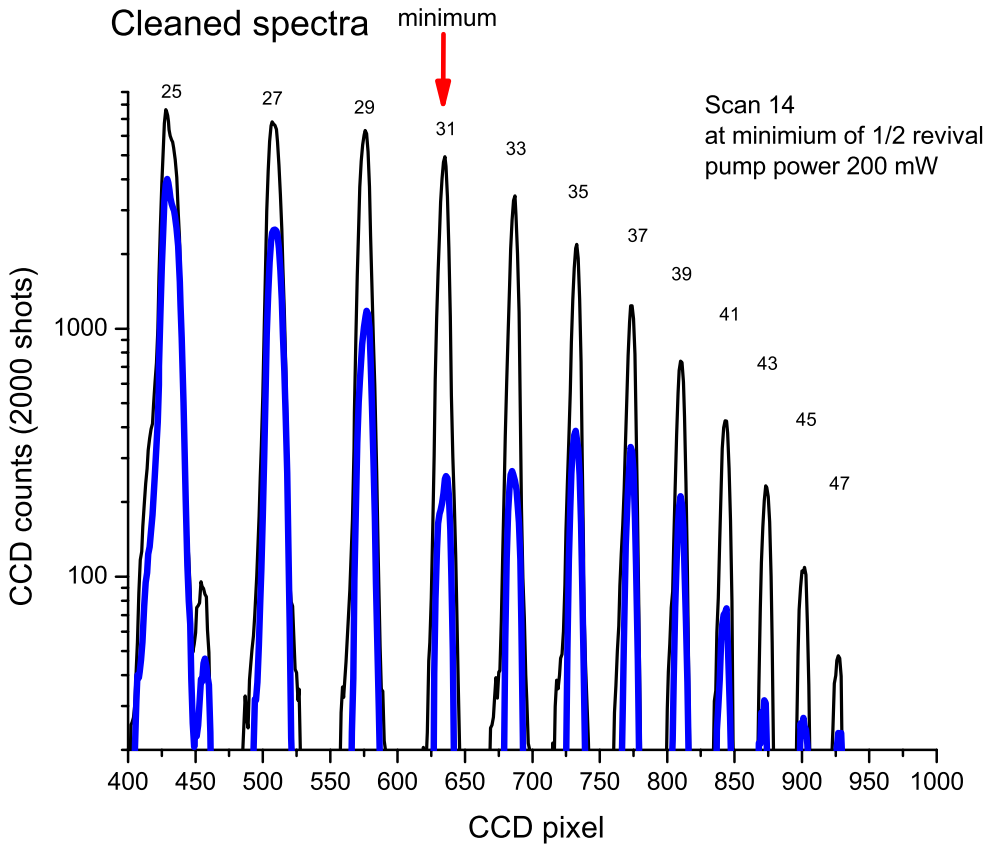

Figure 4.12: High harmonic spectra from aligned CO_2 compared with HHG from an isotropic distribution. The black is the isotropic spectrum and the blue is the aligned spectrum. Due to the butterfly shape of the angular distribution, the angular distribution can be approximated as a classical molecule aligned at 30°.

of anti-correlated. For CO_2 aligned at 30°, the interference maximum is at the 79^{th} harmonic. We would expect the modulation to flip somewhere between the minimum at the 31^{st} harmonic and the maximum at the 79^{th} harmonic. Vozzi[64] claimed to have seen this flip at the 49^{th} harmonic; however, the experimental noise makes the data less than convincing. We have measured the intensity modulations in CO_2 for harmonic orders 13-55 and the modulation is always anti-correlated with the alignment parameter as shown in fig. 4.13. The intensities at an anti-aligned time-delay in this figure are relative to the isotropic intensity, so intensities greater than 1 indicate an anti-correlation with the alignment parameter. It is possible that a flip in the modulation will appear in harmonic orders closer to the 79^{th}.

4.11 Outlook

Using HHG in combination with rotational alignment has been suggested as a method of ultrafast molecular imaging. The first goal would be to extract the a static structure as has been done with N_2[30]. Second, this imaging could then be extended to transient molecular structures such as a dissociating molecule[26]. It is currently not clear how the complexities in the molecular potential, ionization, and multi-electron effects can be overcome to achieve this goal. However, we have demonstrated the importance of first obtaining an accurate measurement of the orientational dipole.

One avenue of further work in this area would be improving the measurement of the orientational dipole. Creating a wave packet with a sharper alignment would allow us to see more features in the intensity modulation and hence extract a more detailed orientational dipole. Excluding propagation effects would make the fitting method better and allow for more trust in the retrieved orientational dipole. This could be done by using a counter propagating blue pulse to create even harmonics and limiting the interaction length. Decreasing the interaction length will minimize phasematching and propagation effects. Additionally, a more powerful laser system would allow the

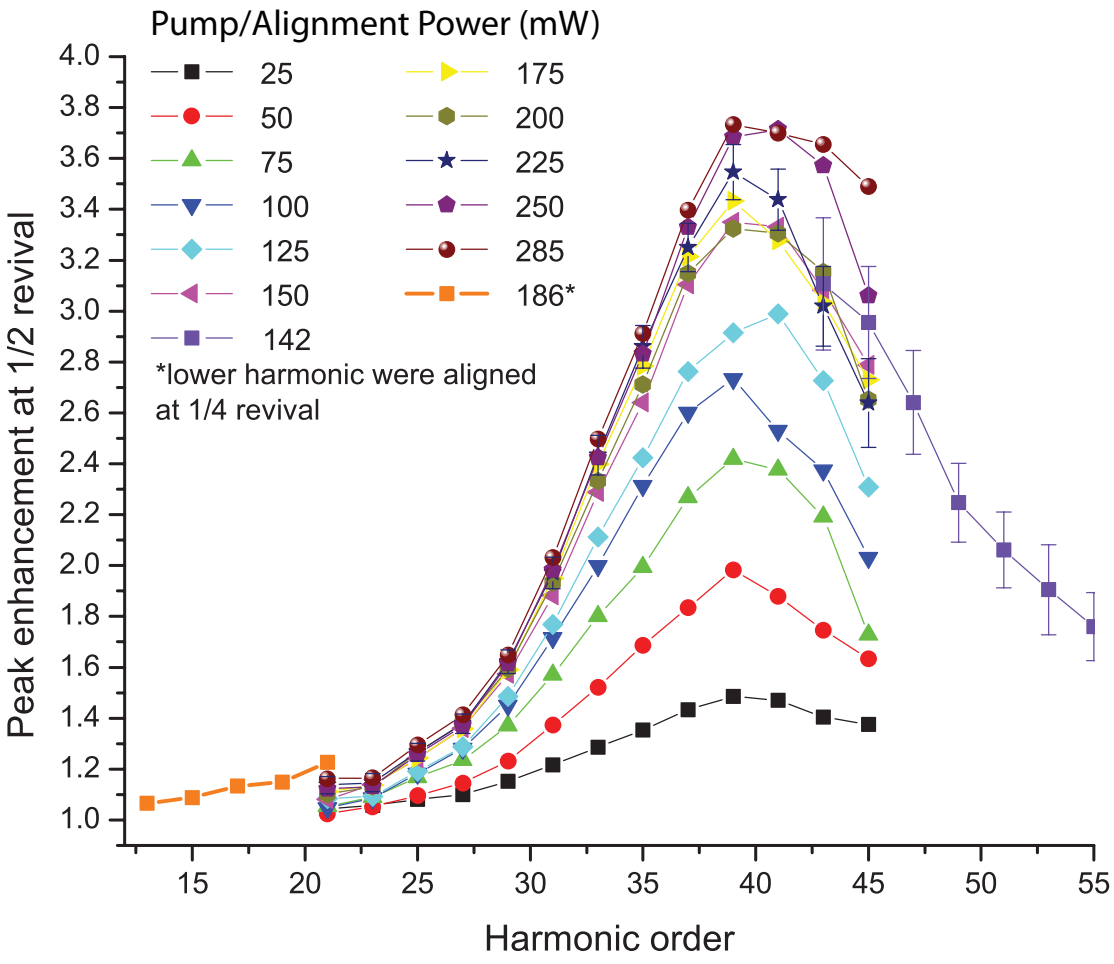

Figure 4.13: Anti-aligned harmonic intensity relative to the isotropic intensity for several pump powers stated in the legend. The graph shows harmonic orders higher and lower than usual range of 19-47. The lower orders were measured using a diffraction grate with lower groove density. The high orders were measured using a zirconium filter instead of aluminum. Peak enhancement > 1 indicates the modulation is anti-correlated with the alignment parameter.

pump pulse to have a larger spot size which would lead to more uniform wave packet over the region which is being probed.

Chapter 5

High Harmonic Generation from Vibrationally Excited Molecules

In this experiment, we demonstrate that it is possible to use high harmonic generation as a probe of internal dynamics in molecules. We impulsively excite[69][71][11] a vibrational wave packet in SF_6 using a short laser pulse, and observe oscillations in the extreme-ultraviolet high-order harmonic emission generated from these molecules using an intense probe pulse. SF_6 was chosen for being a spherically symmetric molecule that can be excited using the impulsive Raman interaction[68] while not being rotationally excited.

The impulsive excitation populates the first vibrational level of each of the 3 Raman active vibrational modes of SF_6. All three modes are observed in the intensity modulation of the high harmonic probe, in contrast to an optical probe where only the strong symmetric stretch is observed. Furthermore, we observe rotational dephasing of the vibrational modulations. First, we will discuss exciting vibrational wave packets, and the vibrational modes of SF_6. Then, we present the intensity modulation observed in excited SF_6, and a Fourier analysis of the modulation. This analysis is then compared with a similar optical experiment. Finally, we will discuss vibrational wave packets observed in other molecules using HHG.

5.1 Exciting Vibrational Wave Packets

Vibrational modes can be excited using methods that we already employed for rotational excitation: both are excited through a two photon Raman processes. The main difference is the spacing of the energy levels. Rotational levels are typically separated by ~ 1 cm^{-1} whereas vibrational levels are separated by 100-1000 cm^{-1}. Additionally, there are a limited number of bound-state vibrational levels before reaching the dissociation limit, whereas rotational states as high as $J \approx 500$[62] can be excited before the centrifugal force pulls the molecule apart.

Because the vibrational energy levels are widely spaced, usually only the first vibrational state is significantly populated in our experiments. This leads to a wave packet whose evolution is much simpler than is the case for the rotational wave packet. The vibrational wave packet consists of the first excited state beating against the ground state, leading to sinusoidal modulation of the mean vibrational coordinate.

Each vibrational mode has a Raman (two-photon accessible) and an infrared character (one-photon accessible). The Raman character is due to the polarizability changing with the vibrational coordinate, and the infrared character comes from the permanent dipole changing with the vibrational coordinate. In molecules that are centrosymmetric (such as diatomics, CO_2 or SF_6), each vibrational mode is exclusively Raman or infrared in nature. Infrared modes are excited resonantly with an infrared electromagnetic field, and Raman modes are excited non-resonantly by a two color Raman process. In the experiments discussed here, we are limited to exciting Raman modes due to the non-resonant nature of our pump. The vibrational modes of SF_6 are shown in figure 5.1. There are 3 Raman active modes, 2 infrared modes and one mode which is forbidden. The forbidden mode changes neither the dipole nor the polarizability significantly.

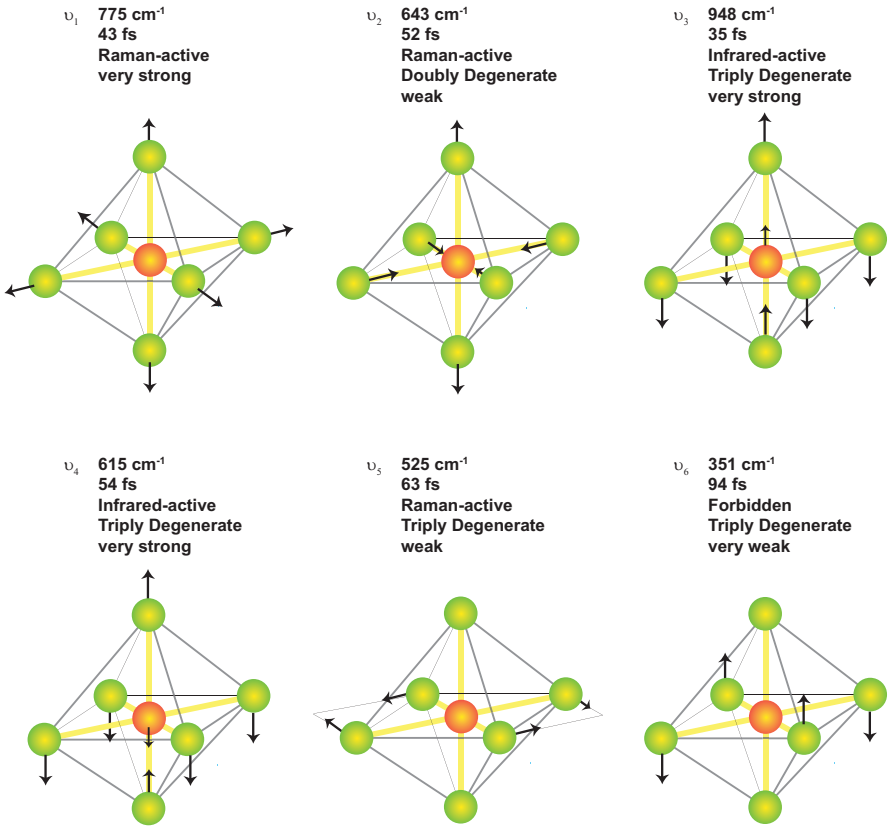

Figure 5.1: Normal modes of vibrations for SF_6. The wavenumber, period, degeneracy and activity of each mode is stated[28]. SF_6 has three Raman-active modes, two infrared active modes and one forbidden mode (which are not excited in our experiment).

5.2 Classical Model

Molecular vibrational modes can be modeled as simple harmonic oscillators with a fundamental frequency equal to the vibrational frequency[9]. The optical field drives the vibration through an induced dipole. We start with Newton's 2nd Law.

$$m\ddot{q} = -kq + F_{drive} \tag{5.1}$$

Here the fundamental frequency of the vibrational mode is $\omega_0 = \sqrt{k/m}$ and q is the vibrational coordinate. The driving force can be found using the potential of an electric field acting on a dipole.

$$\begin{aligned} V &= \frac{1}{2}\mu \cdot \mathbf{E} = \frac{1}{2}\bar{\alpha}(q) \cdot \mathbf{E} \cdot \mathbf{E} \\ F_{drive} &= -\frac{\partial V}{\partial q} = -\frac{1}{2}\frac{\partial \bar{\alpha}(q)}{\partial q} \cdot \mathbf{E} \cdot \mathbf{E} \end{aligned} \tag{5.2}$$

Here $\bar{\alpha}(q)$ is the polarizability tensor expressed as a function of the vibrational coordinate. We have ignored the permanent dipole because this term will average to zero when the electric field oscillates at optical frequencies: $\omega_{optical} >> \omega_0$. This condition is satisfied with a near IR driving field frequency of $13,000 cm^{-1}$ and the fastest molecular vibrations $< 5000 cm^{-1}$. Next, we set the electric field to be linearly polarized, and set an interaction parameter $B = \frac{1}{mc\epsilon_0}\frac{\partial \bar{\alpha}(q)}{\partial q}$. Now, the equation of motion becomes

$$\ddot{q} + \omega_0^2 q = -BI(t) \tag{5.3}$$

where $I(t)$ is the intensity envelope of the optical field. This differential equation can be solved in terms of sinusoids, with the boundary condition $q(t = -\infty) = 0$.

$$q(t) = \frac{i}{\omega_0}\exp(i\omega_0 t)\int_{-\infty}^{t} dt' I(t')\exp(i\omega_0 t') + c.c. \tag{5.4}$$

If we consider times after the driving field has turned off, the integral becomes a Fourier transform. From this it is evident that the efficiency of excitation is proportional to the Fourier component of the driving envelope at the vibrational frequency. For example, we can consider a Gaussian driving pulse $I(t) = I_0 \frac{T}{\tau_{FWHM}} \exp(-4 \log 2 \frac{t^2}{\tau_{FWHM}})$. This will allow me to investigate the excitation of the vibration with respect to the driving pulse duration τ_{FWHM}. We have defined the amplitude of the driving pulse such that the energy in the pulse is constant as the duration is varied.

$$q(t) = -\frac{BI_0T}{2\omega_0}\sqrt{\frac{\pi}{\log 2}} \exp\left(-\frac{\tau_{FWHM}^2 \omega_0^2}{16 \log 2}\right) \tag{5.5}$$

All of the dependence on pulse length is in the exponential and this is plotted in figure 5.2. A driving pulse duration less than half of the vibrational period is needed to excite the mode efficiently.

The vibrational excitation can be modeled quantum mechanically similarly to the quantum mechanical model for the rotational excitation. This quantum mechanical vibrational model is mainly useful for predicting the population in the first excited state.

5.3 Observation of Vibrational Motion in SF_6 using HHG

Figure 5.3 shows the intensity of the 39^{th} harmonic generated in SF_6 as a function of pump-probe time delay. The red(black) curve shows the signal of the 39th harmonic generated with(without) the presence of the pump pulse. When the pump and probe pulses are overlapped, a coherent artifact appears due to the superposition of the two pulses. At positive delay times, the harmonic intensity is periodically modulated with 17 oscillation periods recorded. The amplitude of the oscillations decays as the delay time is increased. At very small delay times, the baseline is lowered and then recovers within 300fs.

Figure 5.4a shows a discrete Fourier transform (DFT) for the time interval from

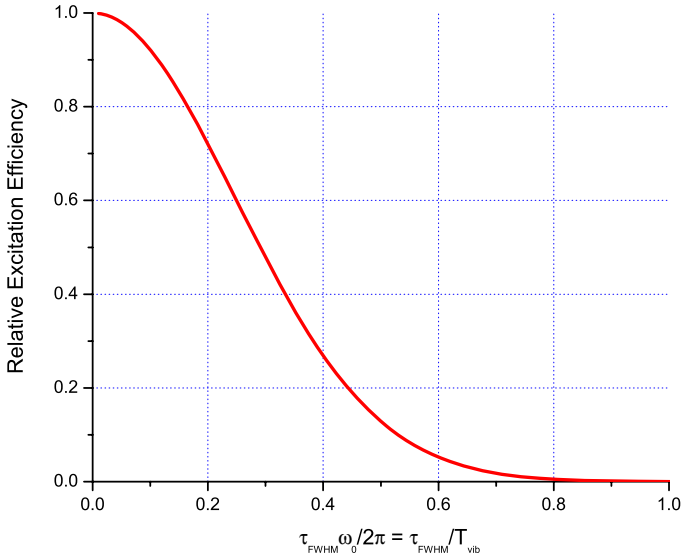

Figure 5.2: Relative excitation efficiency as a function of driving pulse duration relative to vibrational period. A duration less than half the vibrational period is needed for efficient excitation.

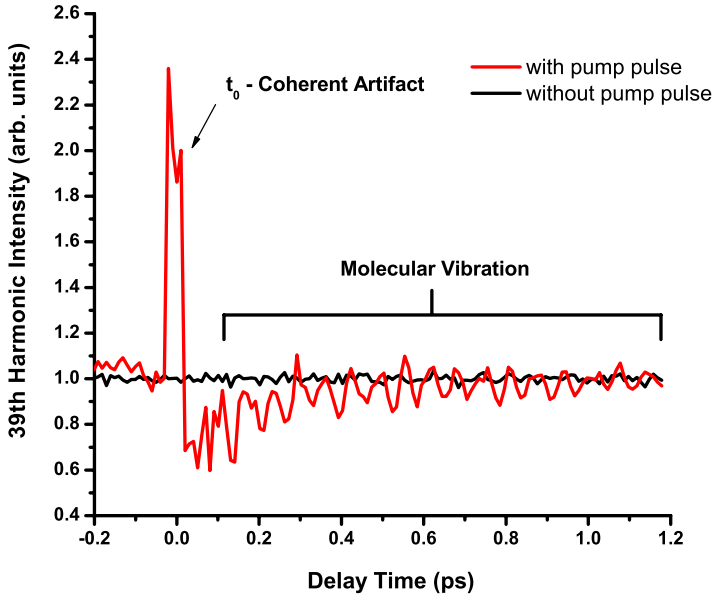

Figure 5.3: Red curve: Intensity of 39^{th} harmonic generated from vibrationally excited SF_6 as a function of time delay between the pump pulse and the EUV generating probe pulse. Black curve: high harmonic emission without the pump pulse present.

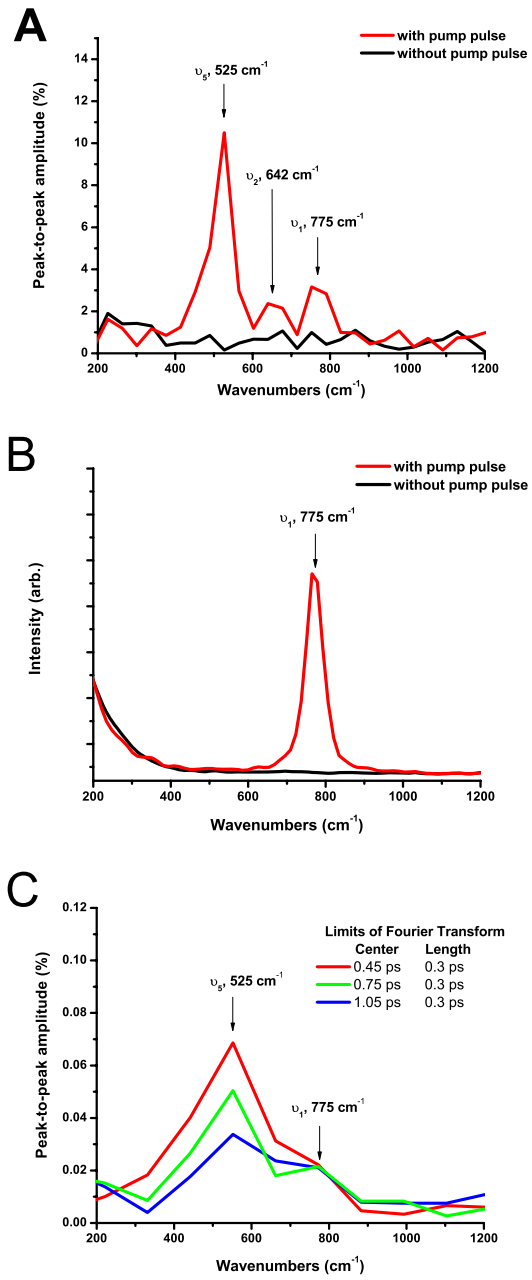

Figure 5.4: a) Discrete Fourier Transform of the 39^{th} harmonic emission from Figure 5.3, showing the three Raman-active modes of SF_6 that are excited by our impulsive stimulated Raman scattering (ISRS) pump pulse. b) Stimulated anti-Stokes Raman scattering of a 400 fs probe pulse centered at 400nm from SF_6, after excitation by the same ISRS pump pulse used to excite vibrations in Fig. 5.3. c) Discrete Fourier Transform of the harmonic emission data from Figure 5.3, for 0.3 ps time intervals centered at different times after the pump pulse (0.45 ps, 0.75 ps and 1.05 ps).

0.3 ps to 1.2 ps in the data in figure 5.3. The red curve shows the spectrum of the modulated high-harmonic signal, while the black curve corresponds to the DFT of the noise background. The vertical axis corresponds to the peak-to-peak percent amplitude modulation of the signal. Three peaks are visible at 525 cm^{-1}, 643 cm^{-1}, and 775 cm^{-1}, corresponding to oscillation periods of 43 fs, 52 fs, and 63 fs, respectively. The Fourier spectrum was normalized such that the spectral amplitude is the percentage modulation of the high harmonic signal in the time domain. These peaks can be assigned to the three Raman-active vibrational modes of SF_6[28] ν_5, ν_2, and ν_1, respectively. The mode ν_1 is totally symmetric, whereas ν_2 and ν_5 are asymmetric and doubly and triply degenerate, respectively.

The vibrational spectrum in figure 5.4a demonstrates that the HHG probe is sensitive to all three Raman-active vibrational modes in SF_6, regardless of their symmetry or degeneracy. In contrast, when the effect of the vibrational motion on the index of refraction of SF_6 is studied, we could only observe the symmetric breathing mode, ν_1. The vibrational wave packet is created by the same pump pulse as in the HHG experiment; however, it is probed with a longer pulse of 400 fs duration and where the central wavelength is 400 nm. The oscillations produce sidebands in the detected spectrum of the probe pulse, as depicted in figure 5.4b. This result is consistent with earlier measurements by Bartels and Weinacht[11] as well as Korn[71] , where the latter used a 10 fs probe pulse.

The amplitude of the modulation in figure 5.3 is not constant in time. We studied the time dependence of the amplitude by taking the DFT of the 39^{th} harmonic at three time intervals: 0.3 ps to 0.6 ps, 0.6ps to 0.9 ps, and 0.9 ps to 1.2 ps. The results are shown in figure 5.4c. Because of the shorter time interval, the resolution of the DFT is coarse and only the modes ν_1 and ν_5 are visible. The amplitude of the symmetric mode ν_1 is constant for all three time intervals; however, the amplitude of the asymmetric mode ν_5 decreases by half as the delay time is increased.

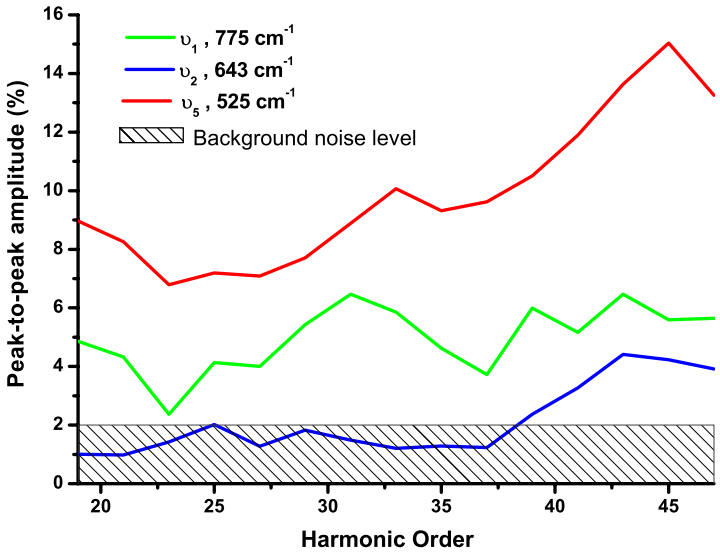

Figure 5.5: Peak to peak amplitude of the observed modulation for the three vibrational peaks shown in Figure 5.4a, as a function of harmonic order; ν_5 (red) , ν_2 (green) , and ν_1 (blue).

For each of the three observed vibrational modes, figure 5.5 shows the modulation of the high harmonic signal as a function of harmonic order for orders 19 to 47, which corresponds to photon energies 30 eV to 75 eV. The amplitude of both asymmetric modes (ν_5 and ν_2) increases with harmonic order, with the signal of the mode ν_2 being above the noise level only for harmonic orders greater than 37. However, the signal of symmetric vibration ν_1 shows no such trend.

5.4 Sensitivity to Vibrational Motion

There are three interesting and new aspects to the data presented in figures 5.3 - 5.5. First, high harmonic generation as a probe of vibrational dynamics is sensitive to small-amplitude oscillations of all the Raman-active vibrational modes of the molecule. (The other IR-active modes are not excited in this experiment.) Because the time scale of the vibrations, at tens of femtoseconds period, is much longer than the sub-optical-cycle time scale of HHG, the nuclear motion is frozen during the HHG probing process. Furthermore, the HHG process is sensitive to small changes in shape of the molecule, we estimate that the S-F coherent bond length change is approximately 5% based on a 10% population in the first excited vibrational state of the symmetric mode, ν_1. This 5% change in bond length increases the intensity of the HHG by 5%.

5.5 Comparison with Other Experiments

A second interesting aspect of this work is that the observed intensities of the vibrational modes using high harmonic emission as a probe differ from the spectra obtained using either traditional Raman spectroscopy or stimulated Raman scattering as a probe. In traditional Raman spectroscopy, the same three modes are observed and the symmetric vibration, ν_1, is most intense[17]. Using high harmonic emission as a probe, all three modes have comparable amplitude; however, the asymmetric vibration, ν_5, is the most intense. Additionally, as we have shown in fig. 5.4b, ISRS experiments

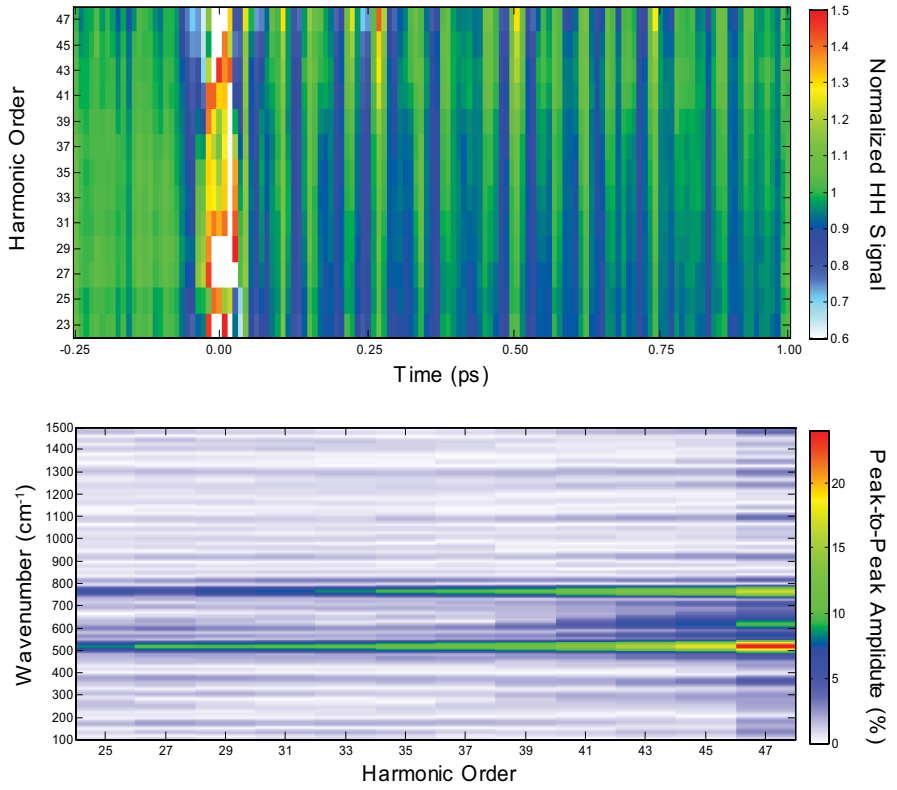

Figure 5.6: (Upper) High harmonic signal for harmonic orders 23 - 47 as a function of time delay. The high harmonic signal without the pump pulse present has been subtracted in order to show the modulations in the high harmonic signal for all harmonic orders. (Lower) Amplitude of the high harmonic modulation by the excited Raman-active modes as a function of harmonic order. The amplitude of all modes significantly increases with harmonic order. The modulation of the high harmonic signal due to the ν_2 mode is above the noise level only for harmonic orders greater than 37.

have only observed the symmetric mode, ν_1. This suggests that using high harmonic emission as a probe is more sensitive to asymmetric modes than is spontaneous Raman spectroscopy or ISRS.

There are several factors which influence the observed vibrational intensities. In the impulsive excitation, the pulse length relative to the vibrational period as well as the differential polarizability determines the population of the vibrational excited states. The vibrational wave packet can modulate the harmonic intensity either through the ionization rate[59] or the recombination integral[36]. The vibrational intensity varies significantly with harmonic order as can be seen in fig. 5.5 . This is evidence that the recombination integral is important in determining the vibrational intensity, because a change in ionization rate would have the same effect on all harmonic orders.

Using HHG as a probe of vibrational wave packets is quite sensitive in terms of the number of molecules needed to observe the vibrational spectrum. The column number density is the number density of molecules multiplied by the interaction length. For the HHG experiment it is greater than 10^{17} molecules/cm^2 and for the spontaneous and ISRS experiments the column density is a factor of 1000 larger.

5.6 Decay of Oscillations

The third interesting aspect of the data is that the amplitude of the modulations in the data of Figure 5.4 decay over the picosecond time window shown. To analyze this decay, we applied a Fourier transform to the data at early times (0.3 ps to 0.6 ps), middle times (0.6 ps to 0.9 ps), and at late times (0.9 ps to 1.2 ps) shown of figure 5.4c. We then compared the magnitude of the symmetric and asymmetric vibrational modes ν_1 and ν_5 in the three time windows. We found that the asymmetric mode was significantly stronger (x2) than the symmetric mode initially, but then decayed to a comparable intensity by the late time interval. In contrast, the amplitude of the symmetric mode was relatively unchanged. We speculate that rotational dephasing may

explain the rapid decay of the asymmetric mode. The excitation of the Raman modes is done using linear polarized light. The polarized light excites a subset of the degenerate set of modes corresponding to the orientation stretched in the direction of the laser polarization. Subsequent random rotational motion of the molecules redistributes the orientation of this excitation, but only for asymmetric modes.

5.7 Calculation of Modulation Amplitudes

Zach Walters has worked to model the high harmonic generation process in molecules, and has modeled the high harmonic intensity from SF_6[67]. The calculation involves expanding each step in high harmonic generation to the first order in the vibrational coordinate. The product of the modulation amplitude for each step predicts the total intensity modulation of the high harmonic intensity. The calculation also includes the effect of the potential on the recombination amplitude. One aspect of the calculation is the connection between high harmonic intensity modulation and the shifting of population between the ground and excited states. The same matrix coefficient in the high harmonic Hamiltonian causes both the intensity modulation and the transfer of population between the vibrational states. This is illustrated in fig. 5.7.

A comparison between the calculated modulation amplitudes and experimental results is shown in fig. 5.8. The modulation amplitudes agree to within an order of magnitude which is an encouraging result considering that the this theory does not take into account macroscopic effects, such as phasematching, absorption, etc.

5.8 Vibrations from Other Molecules

We have observed vibrational wave packets using HHG in two other molecules, $CClF_3$ and N_2O_4. In $CClF_3$ all of the modes are Raman active due to the lack of centrosymmetric symmetry; however, we have observed only two of the Raman active modes. The other modes are not visible most likely due to the noise being too large

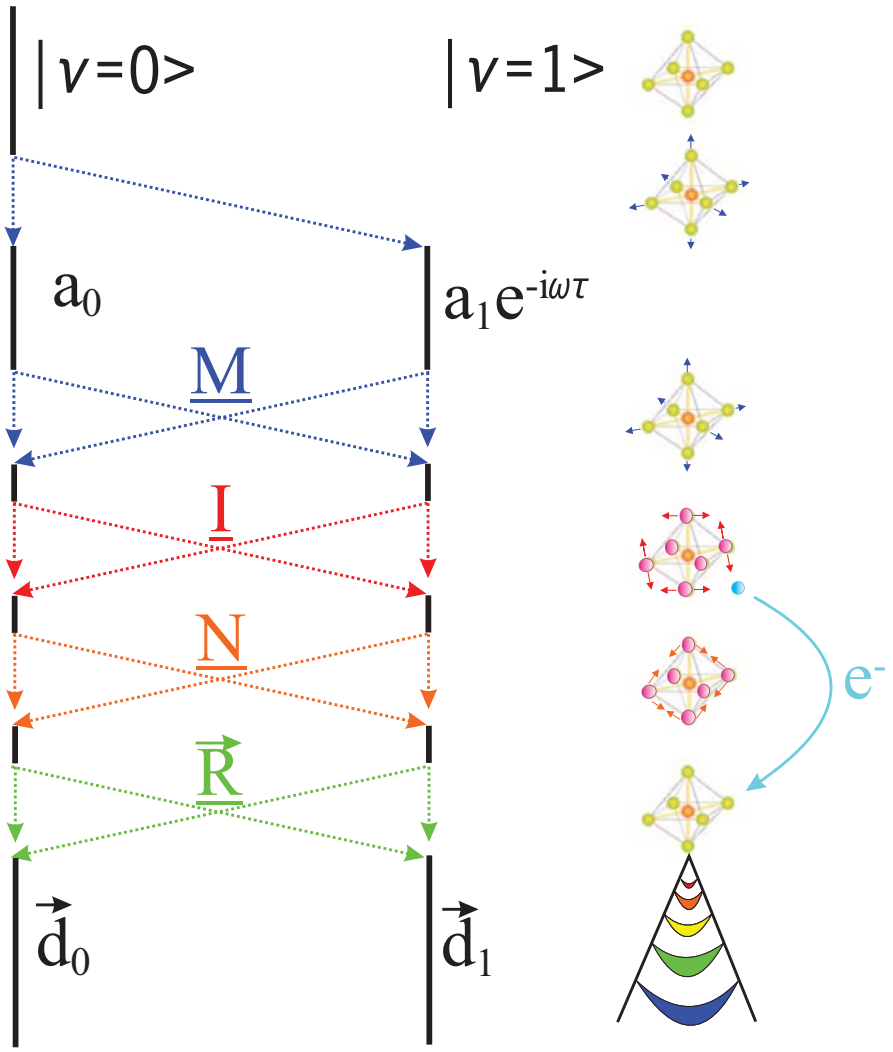

Figure 5.7: A cartoon illustrating the steps involved in generating high harmonics from a system with two vibrational states. Every step can step can shift population between the vibrational states.

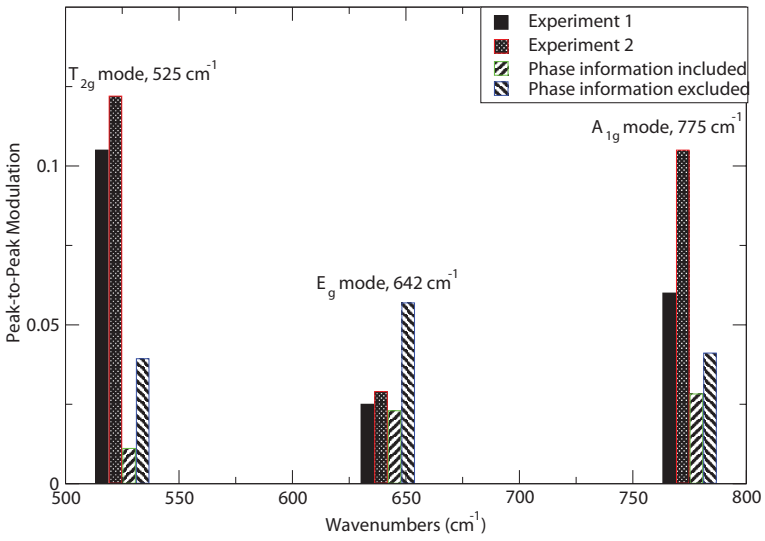

Figure 5.8: A comparison of calculated vibrational amplitudes with experimentally measured amplitudes.

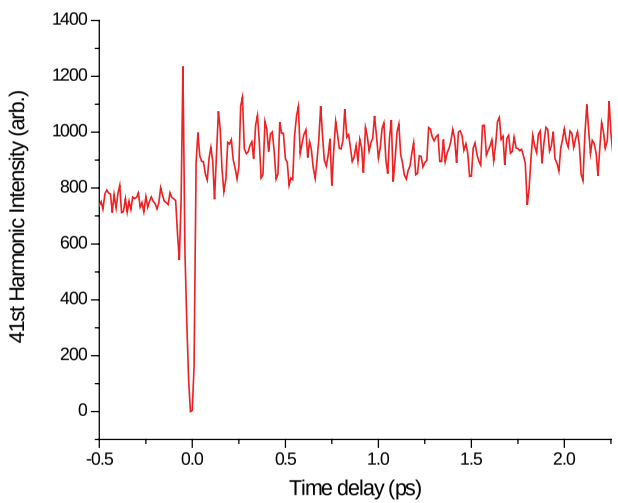

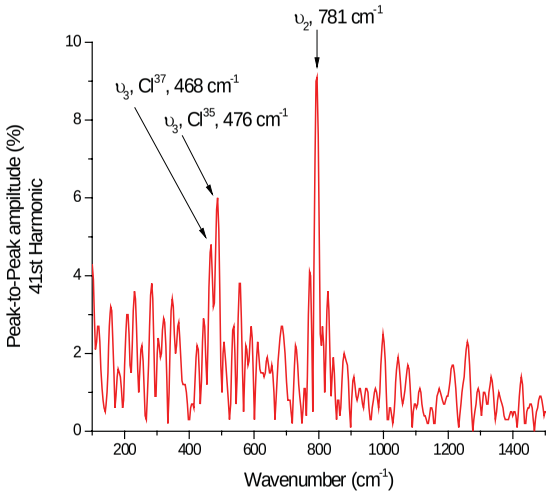

Vibrational modes of $CClF_3$

Wavenumber (cm^{-1})			Period (fs)
350	υ_6	e fundamental	95
468	υ_3	a_1 fundamental Cl^{37}	71
476	υ_3	a_1 fundamental Cl^{35}	70
560	υ_5	e fundamental	60
781	υ_2	a_1 fundamental	43
1106	υ_1	a_1 fundamental	30
1217	υ_4	e fundamental	27

Spontaneous Raman spectrum of $CClF_3$ Claassen, J. Chem. Phys. 22, 50

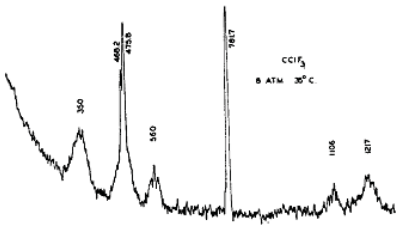

υ_2
782 cm^{-1}
42.6 fs
non-degenerate

υ_3
475 cm^{-1}
70.2 fs
non-degenerate

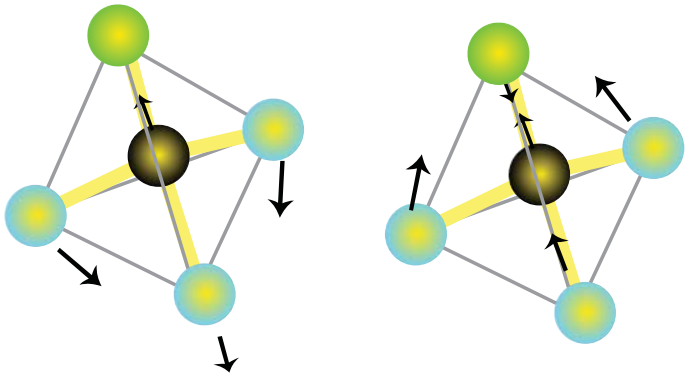

Figure 5.9: The intensity modulation and DFT of the 41^{st} harmonic from vibrationally excited $CClF_3$. Two vibrational modes are visible as well as the isotopic splitting of the ν_3 mode.

and also because for some modes the pulse length is not sufficiently short for a strong excitation. We also have enough resolution to distinguish the isotopic variation in frequency of ν_3. This is shown in fig. 5.9. This mode is dominated by movement of the chlorine atom which is naturally abundant in two common isotopes, ^{35}Cl - 75.8% and ^{37}Cl - 24.2%.

N_2O_4 is dimer of two NO_2 molecules which forms at a temperature slightly below room temperature. A bond between the two nitrogen atoms forms the dimer and is Raman active. The intensity modulation and frequency spectrum of the modulation are shown in figure 5.10. The amplitude of the modulation is quite large when compared with the modulation observed in SF_6. This large modulation is due to two causes. First, the excitation pulse is much shorter than the vibrational period of 128 fs, leading to much more efficient excitation compared with the SF_6 case. Second, there is evidence that the vibration greatly increases the Franck-Condon overlap between the ground state and the cation. This causes the vibration to modulate the ionization rate strongly and consequently the high harmonic intensity.

5.9 Outlook

This work demonstrates the potential for a new kind of vibrational spectroscopy with unique advantages. First, the high harmonic emission as a probe of internal dynamics in a molecule is sensitive to all Raman-active vibrational modes in a molecule, and it is possible that the infrared-active and Raman-active modes could be observed simultaneously. This technique should thus be generally useful for observing dynamics in polyatomic molecules, and could be used to investigate energy redistribution among vibrational modes in molecules, or coherences between vibrational modes. Second, this technique is useful for observing chemically important ground state dynamics in molecules, and since the vibrations observed herein are small-amplitude motion, the utility of this technique to monitor (generally much larger) conformational changes in

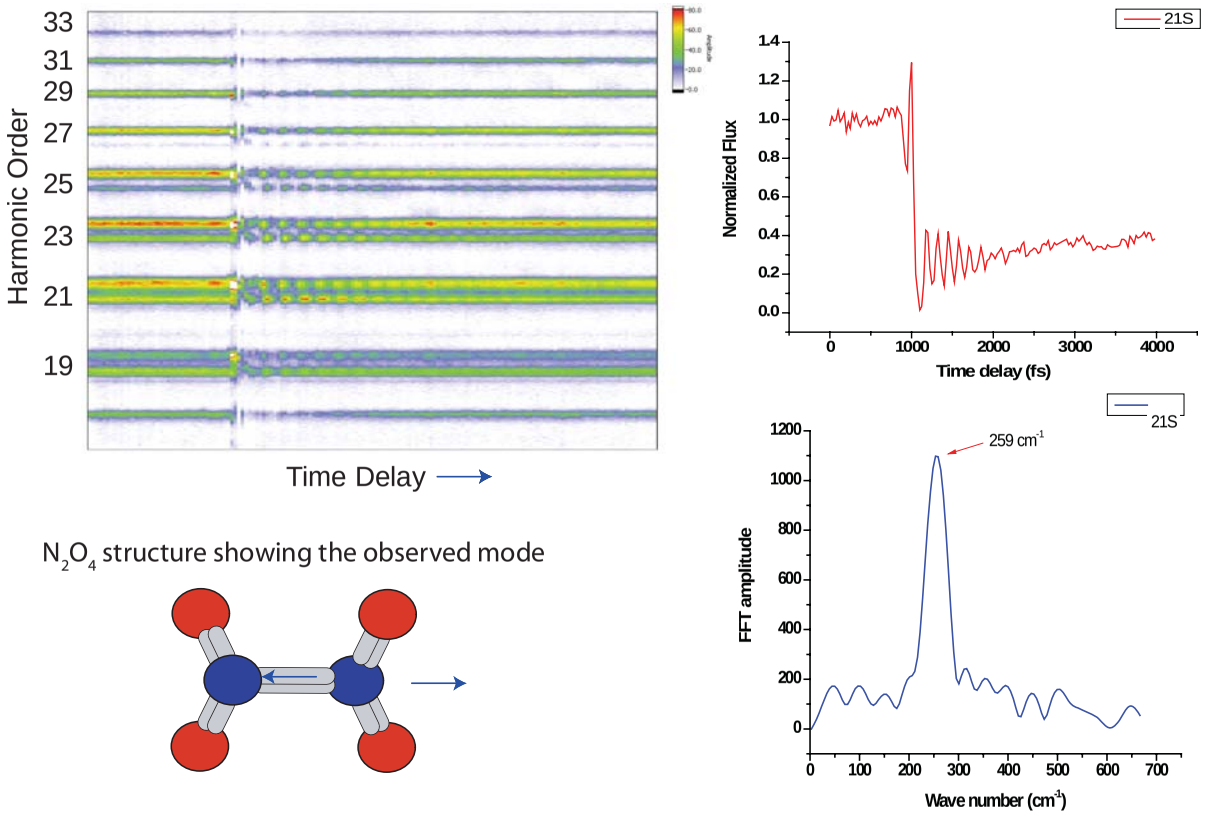

Figure 5.10: The intensity modulation of the high harmonic signal in vibrationally excited N_2O_4.

molecules is very likely. Third, HHG is a coherent ultrafast process that occurs on a sub-cycle timescale. Thus, it should be possible to monitor ultrafast electronic redistribution within the molecule. And finally, by combining this technique with molecular alignment techniques, structural information about the molecule can be retrieved as a function of time as both vibrational and rotational wave packets evolve, or as molecules are highly excited and dissociate.

Chapter 6

Summary

In this work we have used HHG as a probe of molecular wave packets. We have observed rotational wave packets in molecules. Because CO_2 can easily be aligned, rotational wave packets in CO_2 exhibit several unique features such as the bump at maximum alignment. These features can be explained as a π phase shift in the HHG emission, which was also measured experimentally. Furthermore, a fitting method was presented which extracts the complete orientational dipole from the modulated intensity and phase. The general features of the experimental orientational dipole are found to be in agreement with the two center emission model. Future experiments could extract a more detailed orientational dipole and show where the two-center emission model breaks down.

Additionally, we have excited vibrational wave packets in SF_6. All of the Raman-active modes of SF_6 were observed, in contrast to a comparable experiment using an optical probe. We also observed the rotational dephasing of non-spherically symmetric vibration modes in SF_6. The probing of vibrational wave packets using HHG has been extended to additional molecules: $CClF_3$ and N_2O_4 where a very large modulation has been observed.

Bibliography

[1] M. V. Ammosov, N. B. Delone, and V. P. Krainov. Tunnel ionization of complex atoms and atomic ions in a varying electromagnetic-field. Sov. Phys. JETP, 64:1191, 1986.

[2] M. T. Asaki, C. P. Huang, D. Garvey, J. P. Zhou, H. C. Kapteyn, and M. M. Murnane. Generation of 11 fs pulses from a self-mode-locked ti-sapphire laser. Optics Letters, 18(12):977–979, 1993.

[3] D. Attwood. Soft X-Rays and Extreme Ultraviolet Radiaion: Principles and Applications. Cambridge University Press, New York, 1999.

[4] A. A. Babin, D. V. Kartashov, A. M. Kiselev, V. V. Lozhkarev, A. M. Sergeev, A. A. Solodov, and A. N. Stepanov. Ionization spectrum transformation and compression of powerful femtosecond laser pulses in experiments on the propagation in gas-filled dielectric capillaries. JETP Letters, 76(9):548–552, 2002.

[5] A. A. Babin, D. V. Kartashov, A. M. Kiselev, A. N. Stepanov, and A. M. Sergeev. Compression of high-intensity femtosecond laser pulses due to ionization self-phase modulation in gas-filled capillary tubes. Laser Physics, 13(8):1050–1053, 2003.

[6] S. Backus, R. Bartels, S. Thompson, R. Dollinger, H. C. Kapteyn, and M. M. Murnane. Sigh-efficiency, single-stage 7-khz high-average-power ultrafast laser system. Optics Letters, 26(7):465–467, 2001.

[7] S. Backus, C. G. Durfee, M. M. Murnane, and H. C. Kapteyn. High power ultrafast lasers. Review of Scientific Instruments, 69(3):1207–1223, 1998.

[8] R. Bartels, S. Backus, E. Zeek, L. Misoguti, G. Vdovin, I. P. Christov, M. M. Murnane, and H. C. Kapteyn. Shaped-pulse optimization of coherent emission of high-harmonic soft x-rays. Nature, 406:164–166, 2000.

[9] R. A. Bartels, S. Backus, M. M. Murnane, and H. C. .Kapteyn. Impulsive stimulated raman scattering of molecular vibrations using nonlinear pulse shaping. Chemical Physics Letters, 374(3):326, 2003.

[10] R. A. Bartels, A. Paul, H. Green, H. C. Kapteyn, M. M. Murnane, S. Backus, I. P. Christov, Y. W. Liu, D. Attwood, and C. Jacobsen. Generation of spatially coherent light at extreme ultraviolet wavelengths. Science, 297(5580):376–378, 2002.

[11] R. A. Bartels, T. C. Weinacht, S. R. Leone, H. C. Kapteyn, and M. M. Murnane. Nonresonant control of multimode molecular wave packets at room temperature. Physical Review Letters, 88(3):033001, 2002.

[12] R. A. Bartels, T. C. Weinacht, N. Wagner, M. Baertschy, C. H. Greene, M. M. Murnane, and H. C. Kapteyn. Phase modulation of ultrashort light pulses using molecular rotational wave packets. Physical Review Letters, 88(1):013903, 2002.

[13] M. Bellini, C. Lynga, A. Tozzi, M. B. Gaarde, T. W. Hansch, A. L'Huillier, and C. G. Wahlstrom. Temporal coherence of ultrashort high-order harmonic pulses. Physical Review Letters, 81(2):297–300, 1998.

[14] R. Boyd. Nonlinear Optics. Academic Press, San Diego, 1992.

[15] I. P. Christov. Control of high harmonic and attosecond pulse generation in aperiodic modulated waveguides. Journal of the Optical Society of America B, 18:1877, 2001.

[16] M. F. Ciappina, C. C. Chirila, and M. Lein. Influence of coulomb continuum wave functions in the description of high-order harmonic generation with h2+. Physical Review A, 75:043405, 2007.

[17] H. H. Claassen, G. L. Goodman, J. H. Holloway, and H. Selig. Raman specta of mof6, tcf6, ref6, uf6, sf6, sef6, and tef6 in vapor state. Journal of Chemical Physics, 53:341–348, 1970.

[18] P. B. Corkum. Plasma perspective on strong-field multiphoton ionization. Physical Review Letters, 71(13):1994–1997, 1993.

[19] K. W. Delong, R. Trebino, J. Hunter, and W. E. White. Frequency-resolved ooptical gating with the use of 2nd-harmonic generation. Journal of the Optical Society of America B, 11(11):2206–2215, 1994.

[20] C. G. Durfee, A. R. Rundquist, S. Backus, C. Herne, M. M. Murnane, and H. C. Kapteyn. Phase matching of high-order harmonics in hollow waveguides. Physical Review letters, 83(11):2187–2190, 1999.

[21] F. H. M. Faisal, A. Abdurrouf, K. Miyazaki, and G. Miyaji. Origin of anomalous spectra of dynamic alignments observed in n-2 and o-2. Physical Review Letters, 98(14):143001, 2007.

[22] B. Friedrich and D. Herschbach. Polarization of moleules induced by intense nonresonant laser fields. Journal of Physical Chemistry, 99(42):15686–15693, 1995.

[23] M. Ghr, B. K. McFarland, J. P. Farrell, and P. H. Bucksbaum. High harmonic generation for n_2 and co_2 beyond the two-point model. Journal of Physics B: Atomic, Molecluar and Optical Physics, 40:3745–3755, 2007.

[24] E. A. Gibson, A. Paul, N. Wagner, R. Tobey, S. Backus, I. P. Christov, M. M. Murnane, and H. C. Kapteyn. High-order harmonic generation up to 250 ev from highly ionized argon. Physical Review Letters, 92(3):033001, 2004.

[25] A. Gordon, F. X. Kartner, N. Rohringer, and R. Santra. Role of many-electron dynamics in high harmonic generation. Physical Review Letters, 96(22):223902, 2006.

[26] N. Hay, R. Velotta, M. B. Mason, M. Castillejo, and J. P. Marangos. High-order harmonic generation efficiency increased by controlled dissociation of molecular iodine. Journal of Physics B: Atomic, Molecular and Optical Physics, 35:1051–1060, 2002.

[27] M. Hentschel, R. Kienberger, C. Spielmann, G. A. Reider, N. Milosevic, T. Brabec, P. B. Corkum, U. Heinzmann, M. Drescher, and F. Krausz. Attosecond metrology. Nature, 414:509–513, 2001.

[28] G. Herzberg. Molecular Spectra and Molecular Structure. Krieger Publishing, Malabar, 1950.

[29] J. M. Hollas. Modern Spectroscopy. Wiley, 4th edition, 2004.

[30] J. Itatani, J. Levesque, D. Zeidler, H. Niikura, H. Pepin, J. C. Kieffer, P. B. Corkum, and D. M. Villeneuve. Tomographic imaging of molecular orbitals. Nature, 432(7019):867–871, 2004.

[31] J. Itatani, D. Zeidler, J. Levesque, M. Spanner, D. M. Villeneuve, and P. B. Corkum. Controlling high harmonic generation with molecular wave packets. Physcial Review Letters, 94(12):123902, 2005.

[32] T. Kanai, S. Minemoto, and H. Sakai. Quantum interference during high-order harmonic generation from aligned molecules. Nature, 435(7041):470–474, 2005.

[33] T. Kanai, E. J. Takahashi, Y. Nabekawa, and K. Midorikawa. Destructive interference during high harmonic generation in mixed gases. Physical Review Letters, 98(15):153904, 2007.

[34] T. K. Kjeldsen and L. B. Madsen. Strong-field ionization of diatomic molecules and companion atoms: Strong-field approximation and tunneling theory including nuclear motion. Physical Review A, 71:023411, 2005.

[35] K. C. Kulander, K. J. Schafer, and J. L. Krause. Dynamics of short-pulse excitation, ionization and harmonic conversion. Super-Intense Laser-Atom Physics, 316:10, 1993.

[36] M. Lein, N. Hay, R. Velotta, J. P. Marangos, and P. L. Knight. Interference effects in high-order harmonic generation with molecules. Physical Review A, 66(2):023805, 2002.

[37] M. Lein, N. Hay, R. Velotta, J. P. Marangos, and P. L. Knight. Role of the intramolecular phase in high-harmonic generation. Physical Review Letters, 88(18):18903, 2002.

[38] M. Lewenstein, Ph. Balcou, M. Yu. Ivanov, Anne LHuillier, and P. B. Corkum. Theory of high-harmonic generation by low-frequency laser fields. Physical Review A, 49(3):2117 – 2132, 1994.

[39] A. L'Huillier and P. Balcou. High-order harmonic-generation in rare-gases with a 1-ps 1053-nm laser. physical Review Letters, 70(6):774–777, 1993.

[40] A. McPherson, G. Gibson, U. Jara, H.Johann, T. S. Luk, I. A. McIntyre, K. Boyer, and C. K. Rhodes. Studies of multiphoton production of vacuum-ultraviolet radiation in the rare gase. Journal of the Optical Society of America B, 4(4):595, 1987.

[41] K. Miyazaki, M. Kaku, G. Miyaji, A. Abdurrouf, and F. H. M. Faisal. Field-free alignment of molecules observed with high-order harmonic generation. Physical Review Letters, 95(24):243903, 2005.

[42] D. Muller, S. Backus, K. Read, M. Murnane, and H. C. Kapteyn. Cryogenic cooling multiplies output of ti : sapphire output. Laser Focus World, 41(10):65–68, 2005.

[43] B. Nikolaus and D. Grischkowsky. 12x pulse-compression using optical fibers. Applied Physics Letters, 42(1):1–2, 1983.

[44] M. Nisoli, S. De Silvestri, and O. Svelto. Generation of high energy 10 fs pulses by a new pulse compression technique. Applied Physics Letters, 68(20):2793–2795, 1996.

[45] J. Ortigoso, M. Rodriguez, M. Gupta, and B. Friedrich. Time evolution of pendular states created by the interaction of molecular polarizability with a pulsed nonresonant laser field. Journal of Chemical Physics, 110(8):3870–3875, 1999.

[46] S. Patchkocskii, Z. Zhao, T. Brabec, and D. M. Villeneuve. High harmonic generation and molecular orbital tomography in multielectron systems: Beyond the single active electron approximation. Physical Review Letters, 97:123003, 2006.

[47] A. Paul. Coherent EUV Light from High-Order Harmonic Generation: Enhancement and Applications to Lensless Diffractive Imaging. PhD thesis, University of Colorado, 2007.

[48] S. C. Rae. Spectral blueshifting and spatial defocusing of intense laser-pulses in dense gases. Optics Communications, 104(4-6):330–335, 1994.

[49] A. R. Rundquist, C. G. Durfee, Z. H. Chang, C. Herne, S. Backus, M. M. Murnane, and H. C. Kapteyn. Phase-matched generation of coherent soft x-rays. Science, 280(5368):1412–1415, 1998.

[50] P. Salieres, B. Carre, L. Le Deroff, F. Grasbon, G. G. Paulus, H. Walther, R. Kopold, W. Becker, D. B. Milosevic, A. Sanpera, and M. Lewenstein. Feynman's path-integral approach for intense-laser-atom interactions. Science, 292(5518):902–905, 2001.

[51] P. Salieres, Anne LHuillier, and M. Lewenstein. Coherence control of high-order harmonics. Physical Review Letters, 74(19):3776–3779, 1995.

[52] G. Scoles. Atomic and Molecular Beam Methods. Oxford University Press, New York, 1988.

[53] O. Shorokhov, A. Pukhov, and I. Kostyukov. Self-compression of laser pulses in plasma. Physical Review Letters, 91(26):265002, 2003.

[54] A. V. Sokolov, D. D. Yavuz, D. R. Walker, G. Y. Yin, and S. E. Harris. Light modulation at molecular frequencies. Physical Review A, 63(5):051801, 2001.

[55] H. Stapelfeldt and T. Seideman. Colloquium: Aligning molecules with strong laser pulses. Reviews of Modern Physics, 75(2):543–557, 2003.

[56] D. Strickland and G. Mourou. Compression of amplified chirped optical pulses. Optics Communications, 56(3):219–221, 1985.

[57] G. Tempea and T. Brabec. Nonlinear source for the generation of high-energy few-cycle optical pulses. Optics Letters, 23(16):1286–1288, 1998.

[58] W. J. Tomlinson, R. H. Stolen, and C. V. Shank. Compression of optical pulses chirped by self-phase modulation. Journal of the Optical Society of America B, 1(2):139–149, 1984.

[59] X. M. Tong, Z. X. Zhao, and C. D. Lin. Theory of molecular tunneling ionization. Physical Review A, 66(3):033402, 2002.

[60] S. Tonzani and C. H. Greene. Electron-molecule scattering calculations in a 3d finite element r-matrix approach. Journal of Chemical Physics, 122(1):014111, 2005.

[61] D. Umstadter, S. Y. Chen, A. Maksimchuk, G. Mourou, and R. Wagner. Nonlinear optics in relativistic plasmas and laser wake field acceleration of electrons. Science, 273(5274):472–475, 1996.

[62] D. M. Villeneuve, S. A. Aseyev, P. Dietrich, M. Spanner, M. Yu. Ivanov, and P. B. Corkum. Forced molecular rotation in an optical centrifuge. Physical Review Letters, 85(542-545), 2000.

[63] C. Vozzi, F. Calegari, E. Benedetti, R. Berlasso, G. Sansone, S. Stagira, M. Nisoli, C. Altucci, R. Velotta, R. Torres, E. Heesel, N. Kajumba, and J. P. Marangos. Probing two-center interference in molecular high harmonic generation. Journal of Physics B-Atomic Molecular and Optical Physics, 39(13):S457–S466, 2006.

[64] C. Vozzi, F. Calegari, E. Benedetti, J. P. Caumes, G. Sansone, S. Stagira, M. Nisoli, R. Torres, E. Heesel, N. Kajumba, J. P. Marangos, C. Altucci, and R. Velotta. Controlling two-center interference in molecular high harmonic generation. Physical Review Letters, 95(15):153902, 2005.

[65] N. Wagner, E. A. Gibson, T. Popmintchev, I. P. Christov, M. Murnane, and H. C. Kapteyn. Self-compression of ultrashort pulses through ionization-induced spatiotemporal reshaping. Physical Review Letters, 93(17):173902, 2004.

[66] N. L. Wagner, A. Wuest, I. P. Christov, T. Popmintchev, X. B. Zhou, M. M. Murnane, and H. C. Kapteyn. Monitoring molecular dynamics using coherent electrons from high harmonic generation. Proceedings of the National Academy of Sciences of the United States of America, 103(36):13279–13285, 2006.

[67] Z. B. Walters, S. Tonzani, and C. H. Greene. High harmonic generation in sf_6: Raman-excited vibrational quantum beats. Journal of Physics B: Atomic, Molecular and Optical Physics, 40:F277–F283, 2007.

[68] T. C. Weinacht, R. Bartels, S. Backus, P. H. Bucksbaum, B. Pearson, J. M. Geremia, H. Rabitz, H. C. Kapteyn, and M. M. Murnane. Coherent learning control of vibrational motion in room temperature molecular gases. Chemical Physics Letters, 344:333–338, 2001.

[69] A. M. Weiner, D. E. Leaird, G. P. Wiederrecht, and K. A. Nelson. Femtosecond pulse sequences used for optical manipulation of molecular motion. Science, 247(4948):1317–1319, 1990.

[70] H. Wille, M. Rodriguez, J. Kasparian, D. Mondelain, J. Yu, A. Mysyrowicz, R. Sauerbrey, J. P. Wolf, and L. Woste. Teramobile: A mobile femtosecond-terawatt laser and detection system. European Physcial Journal-Applied Physics, 20(3):183–190, 2002.

[71] M. Wittmann, A. Nazarkin, and G. Korn. Femtosecond-pulse synthesis using phase modulation by impulsively excited molecular vibrations. Physical Review Letters, 84(24):5508–5511, 2000.

[72] W. M. Wood, G. Focht, and M. C. Downer. Tight focusing and blue shifting of millijoule femtosecond pulses from a concial axicon ampilifer. Optics Letters, 13(11):984–986, 1988.

[73] K. Yamane, Z. G. Zhang, K. Oka, R. Morita, M. Yamashita, and A. Suguro. Optical pulse compression to 3.4 fs in the monocycle region by feedback phase compensation. Optics Letters, 28(22):2258–2260, 2003.

[74] X. H. Zhang, A. L. Lytle, T. Popmintchev, X. B. Zhou, H. C. Kapteyn, M. M. Murnane, and O. Cohen. Quasi-phase-matching and quantum-path control of high-harmonic generation using counterpropagating light. Nature Physics, 3(4):270–275, 2007.

Appendix A

Lewenstein Model of High Harmonic Generation

The Lewenstein model is a semi-classical model of high harmonic generation that captures the important details of the process in atoms, and is a good place to start a discussion of high harmonic generation in molecules.

Let us start with the time-dependent Schrödinger equation. This formalism is developed in the single active electron approximation and the interaction with the electromagnetic field is limited to the dipole approximation.

$$i\frac{\partial}{\partial t}\left|\Psi(\mathbf{r},t)\right\rangle = \left[-\frac{1}{2}\nabla^2 + V(\mathbf{r}) - \mathbf{E}(t)\cdot\mathbf{r}\right]\left|\Psi(\mathbf{r},t)\right\rangle \tag{A.1}$$

This analysis ignores any bound states above the ground state and ignores depletion of the ground state. Furthermore we will be making the strong-field approximation(SFA) which assumes that when the electron is in the continuum it is not affected by the potential of the atom $V(\mathbf{r})$. Another way of stating the SFA is $2U_p > I_p$.

Now, we divide the wavefunction into a part which stays in the ground state and a part that ionizes into the continuum. The part in the continuum is expressed in terms of momentum eigenstates.

$$\left|\Psi(\mathbf{r},t)\right\rangle = e^{iI_p t}\left(a(t)\left|0\right\rangle + \int d^3\mathbf{v}\, b(\mathbf{v},t)\left|\mathbf{v}\right\rangle\right) \tag{A.2}$$

Here $|0\rangle$ is the ground state of the atom and $|\mathbf{v}\rangle$ is a continuum state with momentum $\mathbf{v}$. We have also factored out the free oscillations of the ground state, $e^{iI_p t}$. Factoring

out this oscillation can be thought of as setting the zero-energy to be the energy of the ground state.

Now, we insert the wavefunction into the the Schrödinger equation. First, we work with the time derivative on the left hand side of the equation. Here, we ignore the ground state depletion by $a(t) \cong 1$.

$$i\frac{\partial}{\partial t}\left|\Psi(\mathbf{r},t)\right\rangle = -I_p\left|\Psi(\mathbf{r},t)\right\rangle + ie^{iI_pt}\int d^3\mathbf{v}\dot{b}(\mathbf{v},t)\left|\mathbf{v}\right\rangle \tag{A.3}$$

Now, we insert the wave function into the right side of the Schrödinger equation, remembering that $e^{iI_pt}\left|0\right\rangle$ is an eigenstate of the Hamiltonian (without the electric field), with energy $-I_p$. Similarly, $\left|\mathbf{v}\right\rangle$ is an eigenstate with energy $\mathbf{v}^2/2 + I_p$. The addition of I_p comes from the phase we have factored out of $\left|\mathbf{v}\right\rangle$.

$$\begin{aligned} H\left|\Psi(\mathbf{r},t)\right\rangle &= -I_pe^{iI_pt}a(t)\left|0\right\rangle \\ &\quad + \mathbf{E}(t)\cdot\mathbf{r}e^{iI_pt}a(t)\left|0\right\rangle \\ &\quad + e^{iI_pt}\int d^3\mathbf{v}\left(\frac{\mathbf{v}^2}{2}+I_p\right)b(\mathbf{v},t)\left|\mathbf{v}\right\rangle \\ &\quad + e^{iI_pt}V(\mathbf{r})\int d^3\mathbf{v}b(\mathbf{v},t)\left|\mathbf{v}\right\rangle \\ &\quad + e^{iI_pt}\mathbf{E}(t)\cdot\mathbf{r}\int d^3\mathbf{v}b(\mathbf{v},t)\left|\mathbf{v}\right\rangle \end{aligned} \tag{A.4}$$

Next, we simplify the 3^{rd} term using the SFA. Basically, the potential only has a zero-order effect on the continuum state, $V(\mathbf{r})\left|\mathbf{v}\right\rangle = -I_p\left|\mathbf{v}\right\rangle$. Now the 1^{st} and 4^{th} terms can be combined.

$$\begin{aligned} H\left|\Psi(\mathbf{r},t)\right\rangle &= -I_p\left|\Psi(\mathbf{r},t)\right\rangle + e^{iI_pt}\mathbf{E}(t)\cdot\mathbf{r}a(t)\left|0\right\rangle \\ &\quad + e^{iI_pt}\int d^3\mathbf{v}\left(\frac{\mathbf{v}^2}{2}+I_p\right)b(\mathbf{v},t)\left|\mathbf{v}\right\rangle \\ &\quad + e^{iI_pt}\mathbf{E}(t)\cdot\mathbf{r}\int d^3\mathbf{v}b(\mathbf{v},t)\left|\mathbf{v}\right\rangle \end{aligned} \tag{A.5}$$

Now put the left and right sides of the equation together and cancel terms.

$$\begin{aligned} i\int d^3\mathbf{v}\dot{b}(\mathbf{v},t)\left|\mathbf{v}\right\rangle &= \mathbf{E}(t)\cdot\mathbf{r}a(t)\left|0\right\rangle \\ &\quad+\int d^3\mathbf{v}\left(\frac{\mathbf{v}^2}{2}+I_p\right)b(\mathbf{v},t)\left|\mathbf{v}\right\rangle \\ &\quad+\mathbf{E}(t)\cdot\mathbf{r}\int d^3\mathbf{v}b(\mathbf{v},t)\left|\mathbf{v}\right\rangle \end{aligned} \tag{A.6}$$

Now multiply both sides of the equation by $\int d^3\mathbf{v}'\left\langle\mathbf{v}'\right|$ and express the position operator $\mathbf{r}$ in momentum space, $i\nabla_v$. And then, drop the integral with respect to $\mathbf{v}$ from every term.

$$\begin{aligned} i\dot{b}(\mathbf{v},t) &= -\left\langle\mathbf{v}\left|\mathbf{E}(t)\cdot\mathbf{r}\right|0\right\rangle+\left(\frac{\mathbf{v}^2}{2}+I_p\right)b(\mathbf{v},t) \\ &\quad+i\mathbf{E}(t)\cdot\int d^3\mathbf{v}'\left\langle\mathbf{v}'\left|\nabla_v b(\mathbf{v},t)\right|\mathbf{v}\right\rangle \end{aligned} \tag{A.7}$$

Looking at the fourth term,

$$\begin{aligned} \int d^3\mathbf{v}'\left\langle\mathbf{v}'\left|\nabla_v b(\mathbf{v},t)\right|\mathbf{v}\right\rangle &= (\nabla_v b(\mathbf{v},t))\int d^3\mathbf{v}'\left\langle\mathbf{v}'\mid\mathbf{v}\right\rangle \\ &\quad+b(\mathbf{v},t)\int d^3\mathbf{v}'\left\langle\mathbf{v}'\left|\nabla_v\right|\mathbf{v}\right\rangle \end{aligned} \tag{A.8}$$

According to Sakurai pg. 54, eqn. 1.7.18, $\int d^3\mathbf{v}'\left\langle\mathbf{v}'\left|\nabla_v\right|\mathbf{v}\right\rangle=0$. So, the differential equation for $b(\mathbf{v},t)$ is

$$\dot{b}(\mathbf{v},t)=-i\left(\frac{\mathbf{v}^2}{2}+I_p\right)b(\mathbf{v},t)-\mathbf{E}(t)\cdot\nabla_v b(\mathbf{v},t)+i\left\langle\mathbf{v}\left|\mathbf{E}(t)\cdot\mathbf{r}\right|0\right\rangle \tag{A.9}$$

This differential equation is the Volkov equation. It can be solved exactly and the solution is stated in the Lewenstein paper.

$$\begin{aligned} b(\mathbf{v},t) &= i\int_0^t dt'\mathbf{E}(t')\cdot\mathbf{d}\left(\mathbf{v}+\mathbf{A}(t)-\mathbf{A}(t')\right) \\ &\times\exp\left(-i\int_{t'}^t\left[(\mathbf{v}+\mathbf{A}(t)-\mathbf{A}(t''))^2/2+I_p\right]\right) \end{aligned} \tag{A.10}$$

where $\mathbf{d}(\mathbf{v}) = \langle \mathbf{v} | \mathbf{r} | 0 \rangle$ and $\mathbf{A}(t)$ is the vector potential in the radiation gauge, $\mathbf{E} = -d\mathbf{A}/dt$.

The argument of the exponential is the semi-classical action,

$$S = \int_{t'}^{t} dt'' \left[(\mathbf{v} + \mathbf{A}(t) - \mathbf{A}(t''))^2/2 + I_p \right] \tag{A.11}$$

The integral is a Feynman path integral, where S is the classical Lagrangian for a free particle in an electric field. Note that the potential of the atom is approximated as I_p. The classical electron trajectories associated with this Lagrangian are $\nabla_v S = 0$.

Now that we know the wave function for the ionized electron, we can calculate the time-dependent dipole. The high harmonic emission's electric field will be proportional to the second time-derivative of the dipole.

$$\begin{aligned} \langle \Psi(\mathbf{r},t) | \mathbf{r} | \Psi(\mathbf{r},t) \rangle &= \langle 0 | \mathbf{r} | 0 \rangle + \int d^3\mathbf{v} d^3\mathbf{v}' b^*(\mathbf{v}',t) \langle \mathbf{v}' | \mathbf{r} b(\mathbf{v},t) | \mathbf{v} \rangle \\ &\quad + \int d^3\mathbf{v} \langle 0 | \mathbf{r} b(\mathbf{v},t) | \mathbf{v} \rangle \\ &\quad + \int d^3\mathbf{v} b^*(\mathbf{v},t) \langle \mathbf{v} | \mathbf{r} | 0 \rangle \end{aligned} \tag{A.12}$$

The first term is zero. The second term will be neglected because it represents continuum-continuum transitions not transitions back to the ground state. The third and fourth terms are complex conjugates.

$$\xi(t) = \langle \Psi(\mathbf{r},t) | \mathbf{r} | \Psi(\mathbf{r},t) \rangle \cong \int d^3\mathbf{v} b^*(\mathbf{v},t) \langle \mathbf{v} | \mathbf{r} | 0 \rangle + c.c. \tag{A.13}$$

Or,

$$\xi(t) \cong \int d^3\mathbf{v} b(\mathbf{v},t) \mathbf{d}(\mathbf{v}) + c.c. \tag{A.14}$$

Now, we insert the solution for $b(\mathbf{v},t)$.

$$\xi(t) = i \int d^3\mathbf{v} \int_0^t dt' \mathbf{E}(t') \cdot \mathbf{d}(\mathbf{v} + \mathbf{A}(t) + \mathbf{A}(t')) \exp(-iS(\mathbf{v}, t, t')) \mathbf{d}^*(\mathbf{v}) \tag{A.15}$$

Next, we introduce a change of variables, $\mathbf{p} = \mathbf{v} + \mathbf{A}(t)$. $\mathbf{p}$ is the canonical momentum and is a constant of the motion. However, it is not the physical momentum of the electron.

$$\xi(t) = i \int_0^t dt' \mathbf{E}(t') \cdot \int d^3\mathbf{p} \mathbf{d}(\mathbf{p} + \mathbf{A}(t')) \exp(-iS(\mathbf{p}, t, t')) \mathbf{d}^*(\mathbf{p} - \mathbf{A}(t)) \tag{A.16}$$

$$S = \int_{t'}^t dt'' \left[(\mathbf{p} - \mathbf{A}(t''))^2/2 + I_p \right] \tag{A.17}$$

Next, we use the stationary-phase approximation to do the integral over $\mathbf{p}$. The integral over $\mathbf{p}$ has the following form

$$\int d^3\mathbf{p} f(\mathbf{p}) \exp(-iS(\mathbf{p})) \tag{A.18}$$

Because $\exp(iS(\mathbf{p}))$ oscillates rapidly, it averages to zero except near the extreme or when $\nabla_p S(\mathbf{p}) = 0$. So, the contributions to the integral are dominated by areas around the roots of $\nabla_p S(\mathbf{p}) = 0$. These roots define the classical electron trajectories. The function $S(\mathbf{p})$ can be expanded in a Taylor series around the roots $\mathbf{p}_s$.

$$S(\mathbf{p}) \cong S(\mathbf{p}_s) + \frac{1}{2} \nabla_p^2 S|_{p_s} (\mathbf{p} - \mathbf{p}_s)^2 \tag{A.19}$$

Now, we also assume that $f(\mathbf{p})$ varies slowly compared to the phase of the exponential. This allows us to pull $f(\mathbf{p}_s)$ out of the integral and the integral becomes

$$f(\mathbf{p}_s) \exp(-iS(\mathbf{p}_s)) \int d^3\mathbf{p} \exp(-i\frac{1}{2} \nabla_p^2 S|_{p_s} (\mathbf{p} - \mathbf{p}_s)^2) \tag{A.20}$$

This integral in 3 dimensions can be converted to the product of 3 one dimensional integrals.

$$f(\mathbf{p}_s)\exp(-iS(\mathbf{p}_s))\int d^3p_x \exp(-i\frac{1}{2}\nabla_p^2 S|_{p_s}(p_x-p_{sx})^2) \int d^3p_y \exp(-i\frac{1}{2}\nabla_p^2 S|_{p_s}(p_y-p_{sy})^2) \int d^3p_z \exp(-i\frac{1}{2}\nabla_p^2 S|_{p_s}(p_z-p_{sz})^2) \tag{A.21}$$

Now we can perform a change of variables $\pi\zeta^2/2 = a(p_x - p_{sx})^2$ for the integral.

$$f(\mathbf{p}_s)\exp(iS(\mathbf{p}_s))\left(\frac{\pi}{\nabla_p^2 S|_{p_s}}\right)^{3/2}\left(\int_{-\infty}^{\infty} d\zeta \exp(-i\pi\zeta^2/2)\right)^3 \tag{A.22}$$

This is now a Fresnel integral, $\int_{-\infty}^{\infty}(\cos(\pi x^2/2) - i\sin(\pi x^2/2))dx = 1 - i = i\sqrt{i}$. Additionally, $\nabla_p^2 S|_{p_s} = t - t'$. Inserting this, we get

$$-if(\mathbf{p}_s)\exp(iS(\mathbf{p}_s))\left(\frac{\pi i}{t-t'}\right)^{3/2} \tag{A.23}$$

Now we can put the result of the integral into the equation for the dipole, $\xi(t)$.

$$\xi(t) = \int_0^t dt' \left(\frac{\pi i}{t-t'}\right)^{3/2} \mathbf{E}(t')\cdot\mathbf{d}(\mathbf{p}_s + \mathbf{A}(t')) \times \exp(-iS(\mathbf{p}_s, t, t'))\mathbf{d}^*(\mathbf{p}_s - \mathbf{A}(t)) \tag{A.24}$$

where $\mathbf{p}_s$ is defined by

$$\nabla_p S(\mathbf{p}_s, t, t') = \int_{t'}^{t} dt''(\mathbf{p}_s - \mathbf{A}(t'')) = 0 \tag{A.25}$$

This is the main result: the dipole as a function of time in the generating pulse. Taking the 2^{nd} time derivative and Fourier transforming will give the high harmonic spectrum for a particular pulse shape.

Usually the optical field is sinusoidal in which case the integration over the ionization time can be carried out. This integral is simplified using the stationary phase approximation. For a sinusoidal field there are two stationary phase points for every

cycle of the pulse. These two solutions are the long and short trajectories. Furthermore due to the spatial spread of the continuum electron wave packet, only ionizion times from the immediate cycle need to be considered. Using the stationary phase approximation reduces the integral to a sum with two terms: one for the long trajectory and one for the short trajectory.

Each term is made up of three complex amplitudes. First, the ionization rate, where the ADK ionization rate is usually employed. Second is the propagation, which determines the energy of the harmonic because the phase accumulation of the returning electron determines how fast the dipole oscillates. Third is the recombination amplitude, which in the plane wave approximation is a Fourier transform of the highest orbital and the the dipole operator.

Appendix B

Self-compression of Ultrashort Pulses in an ionizing medium

The propagation of intense femtosecond duration light pulses in materials, gases and plasmas is important for many areas of high field science, such as high-harmonic generation[40][39], laser-particle acceleration[61], and LIDAR based on atmospheric propagation of laser beams[70]. Nonlinear propagation has also been employed extensively in ultrafast technology for temporal compression of pulses to even shorter duration. Nonlinear self-phase modulation (SPM) experienced by a pulse as it travels through a medium will spectrally broaden it. This broadened pulse bandwidth can then be compressed by applying appropriate dispersion to the pulse subsequent to the spectral broadening. Typically, a pulse is self-phase modulated by propagation through an optical fiber[58][43] or a gas-filled hollow optical waveguide[44], and dispersion compensation is provided by pairs of prisms or gratings, or using chirped mirrors to induce a negative chirp. These schemes have been employed to compress pulses to < 4 fs pulse duration[73]; however, they are also relatively complex and lossy. Furthermore, all previously demonstrated schemes are limited to compression of pulses at nanojoule to sub-millijoule energy, limited by the characteristics of the fiber or waveguide propagation, and by the damage threshold of the nonlinear material. SPM-based techniques also tend to generate pulses with large spectral modulations and complex nonlinear chirps that are difficult to compensate for, resulting in large temporal pedestals on the pulse. A variety of other schemes for pulse compression have been demonstrated or

proposed; for example, phase modulation of a light pulse induced by molecular phase modulation[71] [12] [54] using vibrational or rotational motion. However, these schemes are also limited to laser intensities below the dissociation threshold of the molecule. The use of ionization to blue-shift and phase modulate a pulse for compression has been previously considered [57] [4] [5]; however, this scheme also depended on the use of external dispersion compensation, and is distinct from the mechanism seen in this work.

In this work, we discovered a new and unanticipated regime of ultrashort pulse compression that operates at high laser intensities, where the pulse is ionizing the medium[65]. We show that an intense 800 nm wavelength pulse propagating through a short gas-filled hollow waveguide, can reshape and self-compress in time without the need for subsequent dispersion compensation. Theoretical models show a new mechanism for pulse compression where spatio-temporal reshaping of the pulse occurs by ionization-induced spectral broadening, plasma-induced refraction, and guiding in the hollow waveguide. Therefore, this new technique is fundamentally different from previous mechanisms that broaden the spectrum of a short pulse in a waveguide, and then subsequently compress it using dispersion. This high field pulse compression is unique in its ability to shorten the duration of intense light pulses with high efficiency and with excellent pulse fidelity. Because this new mechanism can operate at intensities that are significantly higher than in other schemes, it may be scalable to much higher pulse energies, with implications for the design of many high field science experiments.

In our experiment, pulses from a Ti:sapphire amplifier with ~ 30 fs near transform-limited pulse duration and with energy of 2.2 mJ, at repetition rate of 1 kHz[6] were focused into a 2.5 cm long, 150 μm inner-diameter, hollow waveguide filled with low pressure argon. The spot diameter of the laser at the entrance to the waveguide was 50 μm FWHM. The energy throughput of the waveguide is $\sim 60\%$ with no gas present, adjusted for other losses. The focusing region before and after the waveguide was held under vacuum to limit the interaction region and to maintain a constant pressure[49].

The pulse was characterized before and after the waveguide using second-harmonic Frequency Resolved Optical Gating (SHG-FROG)[19]. All FROG measurements were deconvolved using commercial software from Femtosoft Technologies (Version 3.03) to an error of $< 1\%$ at for a 256×256 grid. After exiting the waveguide, the pulse passes through a 250 μm sapphire window and a 1 mm thick fused silica beamsplitter in the FROG apparatus; the dispersion of these elements corresponds to an additional pulse chirp that stretches the measured pulse duration of at-most 1-3 fs, and therefore does not affect our findings. Therefore, our pulsewidth measurements accurately determine the pulse duration at the exit of the waveguide. No effort was made to further optimize the measured pulsewidths. If there is no gas in the waveguide, the duration of the pulse going into the waveguide is equal to that after the waveguide to within our measurement resolution.

The intensity in the waveguide, at approximately 10^{15} W cm^{-2}, is high enough that the argon gas is fully ionized on the leading edge of the pulse. This rapidly-changing ionization during the leading edge of the pulse results in an index of refraction that decreases rapidly with time, causing an overall blue shift in the laser spectrum of tens of nanometers, which has been observed previously[72]. Figure B.1 shows the pulse spectra at the exit of the waveguide with and without gas in the guide. Pressures as low as 1 torr result in a significant blue shift and broadening. As the pressure is increased, the pulse width also decreases to a minimum value of 13.3 fs at pressures around 4 torr. The compressed pulse width then remains relatively constant for increased pressures up to 9 torr, at which point the laser mode begins to break up. Both the input pulse and the compressed final pulse have pulse width within 20% of the time-bandwidth product, as shown in Fig. B.2. Figure B.2(a) shows the temporal envelope of the pulse with and without gas in the waveguide. The initial pulse width of 28.9 fs has been dramatically reduced in duration to 13.3 fs at a pressure of 4 torr. The measured pulse spectra and the deconvolved spectra from the FROG are shown in Fig. B.2(b), and correspond to a

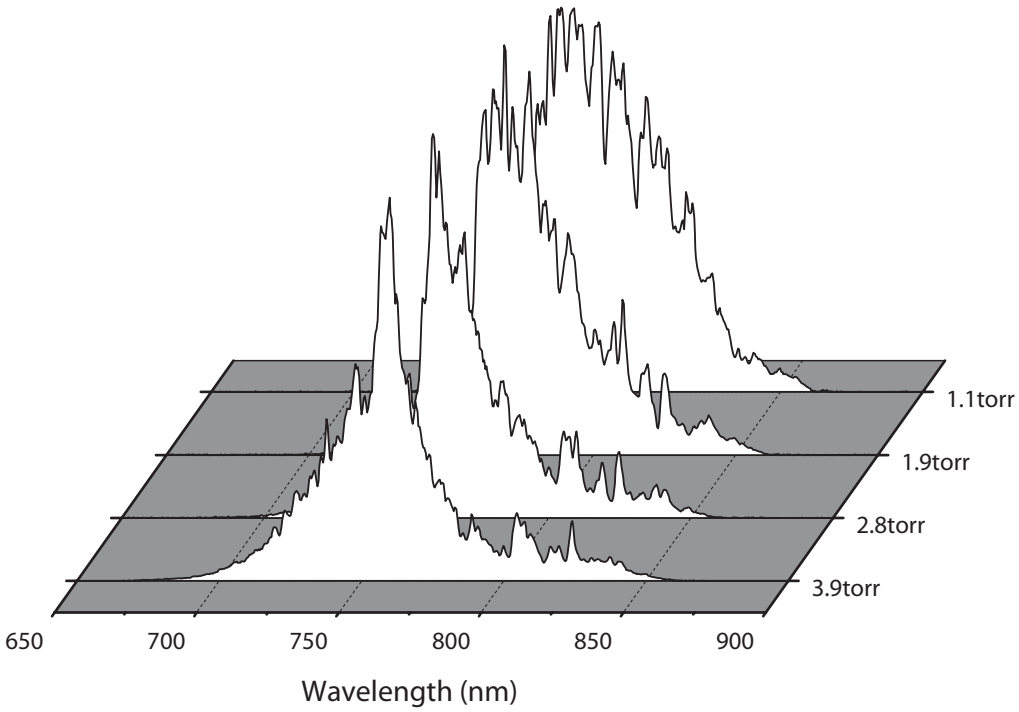

Figure B.1: Spectra of pulses emerging from a waveguide filled with argon at pressures starting at 4 torr decreasing to 0 torr, front to back. Ionization induces a spectral blueshift and broadening of the pulse.

transform limit of 11 fs. The excellent agreement between the measured and retrieved spectra indicates that the measurement has high accuracy and that it is self-consistent. At a pressure of 4 torr, the energy loss from the compression process is only 5% of the total pulse energy i.e. the output energy drops by 5% at 4 torr, while at 8 torr the loss is 10%. We observe lower levels of compression (from 30 fs to 24 fs) using a larger diameter, 230 μm, waveguide, and minimal amounts of compression by < 1 fs when the waveguide is replaced by a large-diameter cell.

Conventional 1-D pulse propagation models, such as those used to explain self-phase modulation in optical fibers, microstructured fibers, or hollow waveguides, fail to explain the observed compression phenomenon. In conventional pulse compression techniques, spectral broadening is accomplished through self-phase modulation (SPM). However, SPM alone broadens the pulse spectrum, but does not alter the temporal envelope. Higher-order corrections due to self-steepening and other effects can reshape the trailing edge of the pulse, but will not shorten the pulse in time without subsequent pulse compression. At high intensities however, significant spectral and temporal effects are expected due to the rapid ionization on the leading edge of the pulse that leads to a rapidly decreasing plasma index $n_p = \sqrt{1 - (\omega_p^2/\omega^2)}$ where ω_p is the plasma frequency given by $\omega_p^2 = n_e e^2/m\epsilon_o$, e and m are the charge and mass of the electron, and n_e is the electron density. The rapidly-decreasing index due to the creation of a plasma leads to a blue-shifting and broadening of the spectrum, that can then support a shorter pulse[14]. However, this effect alone cannot change the temporal envelope of the pulse. Self-steepening will also occur due to the rapidly changing plasma index of refraction. The sign of this self-steepening term is same as self-steepening in a normal material, and therefore it also leads to a steep trailing edge on the pulse, but should not decrease pulse duration. Table B.1 summarizes the potential 1-D pulse-shaping mechanisms and the characteristic propagation length over which these effects becomes significant. From Table B.1, it is clear that the plasma-induced phase modulation and self-steepening

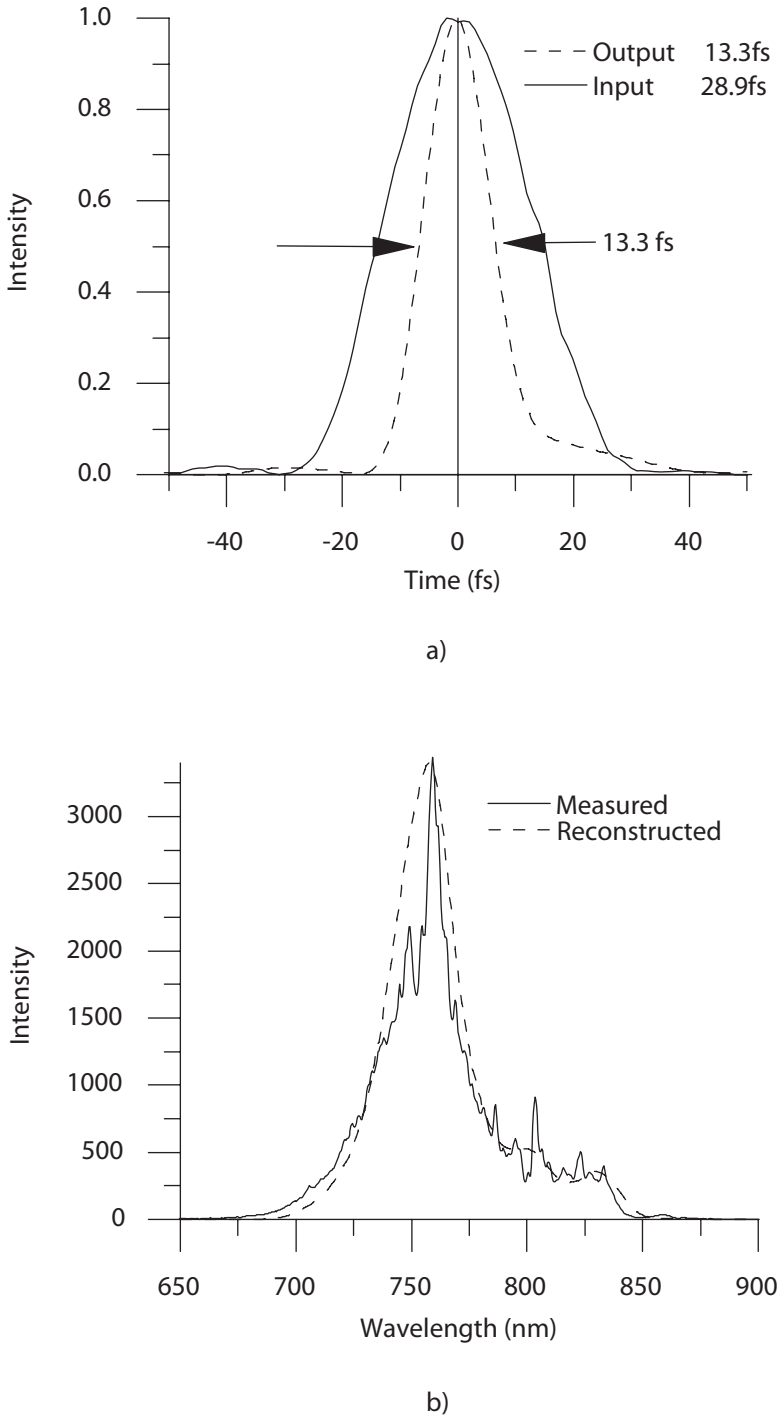

Figure B.2: Input and output pulse characteristics at the 4 torr optimum pressure for compression of pulse with an input laser intensity of 10^{15} Wcm^{-2}. (a) Temporal profile and phase of the input pulse (29 fs) and the final compressed pulse (13.3 fs), (b) Measured spectrum of the compressed pulse, compared with the spectrum of the pulse reconstructed from the time-domain second-harmonic FROG data. These data demonstrate the fidelity of the compressed pulse measurement.

will be dominant, with some contribution due to conventional SPM. However, no self-compression is possible due to any of the effects listed in Table B.1.

Mechanism	Length Scale	Distance
Waveguide GVD	$\frac{T^2 a^2 \omega^3}{8\log(2)\mu_{nm}^2 c}$	1 m
Gas GVD	$\frac{T^2}{4}\frac{2\pi c^2}{\log(2)\lambda^3 d^2 n/d\lambda^2}$	1.5 km
Plasma GVD	$\frac{T^2 c\omega}{4\log(2)}\frac{\omega^2}{\omega_p^2}$	60 cm
Gas SPM	$\frac{c}{\omega n_2 I}$	10 cm
Gas self-steepening	$\frac{cT}{n_2^{(g)} I}$	3 m
Plasma blue-shift	$\frac{2\omega c}{\omega_p^2}$	2.3 mm
Plasma self-steepening	$2Tc\frac{\omega^2}{\omega_p^2}$	6.5 cm

Table B.1: Table of possible pulse shaping mechanisms that involve only 1-D propagation effects in Ar at a pressure of 4 torr (i.e. not spatio-temporal pulse evolution effects) and the length of propagation over which they become significant[14]. T = pulse duration; GVD = group velocity dispersion; n_2 = nonlinear index of Ar; n = linear index of Ar; I = laser intensity; ω = laser frequency; c = speed of light; u_{nm} = waveguide mode index; a = waveguide radius. The calculated gas terms are lower limits calculated for neutral Ar.

Since 1-D nonlinear wave propagation cannot explain this phenomenon, and since experimentally we found the waveguide to be essential, we turned to a 3-D model to explain the results. Propagation of the laser in the waveguide was modeled by a numerical solution of a 3-D scalar wave equation for the laser field, as reported previously[14]. The model takes into account dispersion due to the transient plasma, power dissipation due to ionization, and dispersion due to the neutral gas, at each radial position in the guide as a function of time. Also, the 3-D diffraction experienced by the beam in the waveguide automatically includes the correct value of negative dispersion due to the waveguide. Finally, waveguide loss was measured experimentally and incorporated into the model.

The theoretically predicted pulse durations as a function of pressure are shown in Fig. B.3(a), together with the experimentally measured values for comparison (Fig. B.3(b)). The model is in excellent agreement with experimental data, predicting that

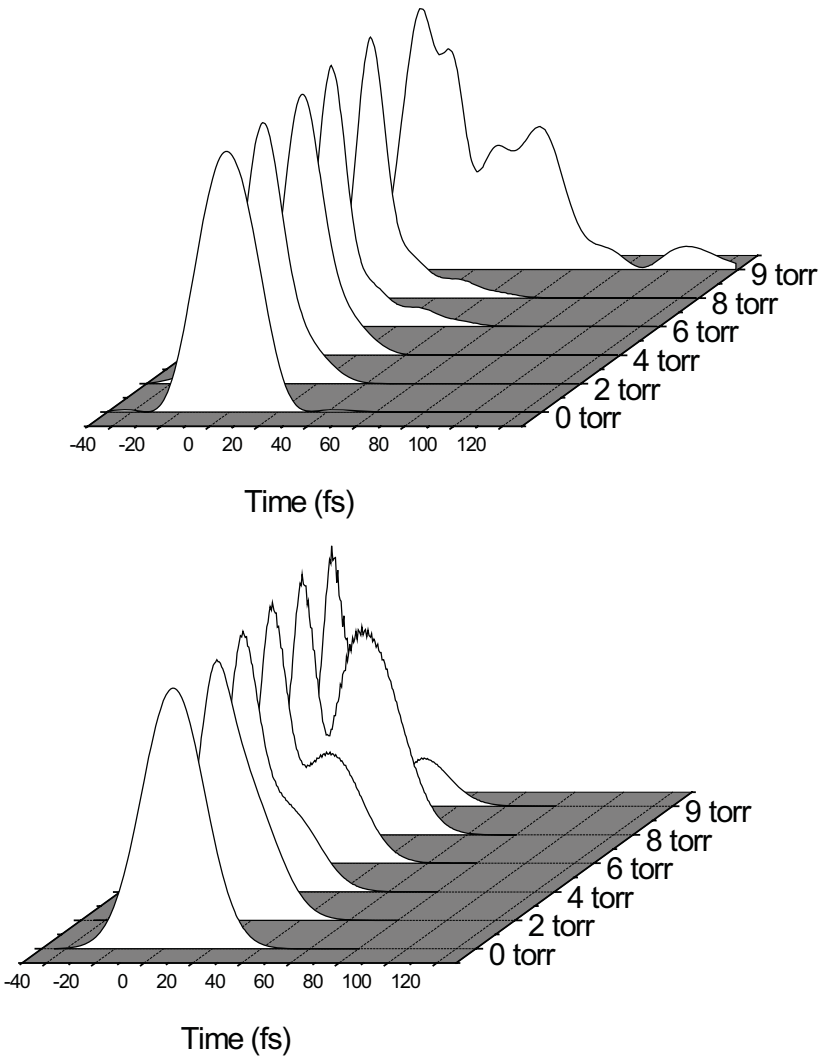

Figure B.3: Comparison between the experimentally observed (reconstructed FROG) and theoretically predicted pulse envelopes as a function of pressure for 0, 2, 4, 6, 8 and 9 torr. (a) Experimentally measured pulse shapes (b) Theoretically predicted pulse shapes. The pulse compression and pulse splitting behavior are seen both experimentally and theoretically, with excellent qualitative and good quantitative agreement between experiment and model.

the pulse undergoes temporal reshaping that reduces the pulse width from 30 fs to approximately 13 fs with increasing pressure, and that the minimum pulse duration is obtained around 4 torr. The leading edge of the pulse also steepens in time, accompanied by a longer trailing edge that develops a shoulder as the pressure is increased- again in very good agreement with experiment. The model also predicts less compression for larger diameter waveguides and little or none for the case of no waveguide, as is the case experimentally. Finally, the corresponding pulse spectral blue shift and increase in bandwidth is due to the combined effects of rapidly changing plasma index and self-phase modulation, also in good agreement with experiment. At high pressures above $\sim$ 8 torr, the pulse splits and the spectrum develops a large long-wavelength wing, leading to the breakup also observed in experiment. The only parameter in our calculations that was adjusted to obtain agreement is the input diameter of the focused laser mode into the waveguide.

From our models, we can identify the mechanism behind the self-compression as a spatio-temporal interplay of plasma-induced refraction and blue shifting, diffraction of the laser beam, phase modulation due to the rapidly-changing plasma index, and finally guiding by the hollow waveguide. The role of plasma defocusing[48] is very important in the compression process because it is responsible for the spatio-temporal coupling at high, ionizing, laser intensities. The presence of the waveguide is also crucial, both experimentally and theoretically. Our models show that as the pulse begins to ionize the gas, the trailing edge of the pulse refracts from the center of the waveguide due to plasma-induced defocusing. However, this portion of the beam is then reflected back into the guide by reflection from the waveguide walls. This leads to a temporally compressed pulse with a sharp leading edge and flat temporal phase, in dramatic contrast to other pulse compression schemes. The reshaping also leads to a small periodic oscillation in the beam diameter and pulsewidth as the pulse propagates down the waveguide. This high-field pulse reshaping process has similarities with passive mode locking of lasers

using saturable absorbers - the trailing edge of the pulse is slowly depleted periodically along the waveguide due to ionization-induced defocusing, where the role of a laser resonator is replaced by the waveguide. Both experimentally and theoretically, the pulse compression process is sensitive to the initial mode launched into the waveguide. The laser beam must be focused to a tighter focal spot (50 μm FWHM) than ideal ($\sim$ 100 μm FWHM) for coupling into the lowest-order mode of 150 μm waveguide, in order to launch a mode that gives rise to large ionization levels and a high degree of plasma-induced refraction.

In conclusion, we demonstrate a new and unanticipated mechanism for pulse compression that operates at laser intensities above the ionization threshold for the first time. By propagating intense, femtosecond, pulses inside a hollow-core waveguide filled with low-pressure argon gas, we demonstrate an increased bandwidth as well as temporal self-compression of a pulse without the need for dispersion compensation. Theoretical models show a new mechanism for pulse compression where spatio-temporal reshaping of the pulse occurs by ionization-induced spectral broadening, plasma-induced refraction, and guiding in the hollow waveguide. This result represents a significant simplification over other pulse compression techniques at laser intensities above the ionization thresholds of atoms and molecules, and will be useful in many applications in high field science. This mechanism is likely to scale to higher intensities and pulse energies, and likely also to the use of plasma-based waveguides.